同期電動機のためのON/OFF法をもとにした位相最適化

博士学位論文

Topology Optimization Based on ON/OFF Method for Synchronous Motors

室蘭工業大学大学院 工学研究科 博士後期課程
工学専攻 先端情報電子工学コース

SUN ZHEN

指導教員
渡辺　浩太 教授

Declaration

I hereby declare that this thesis is my own work and effort and that it has not been submitted anywhere for any award. Wherever contributions of others are involved, every effort is made to indicate this clearly, with due reference to the literature, and acknowledgment of collaborative research and discussions.

SUN ZHEN
June 2023

Acknowledgements

Firstly, I would like to express my sincere gratitude to my doctoral supervisor Prof. Kota Watanabe for giving me the opportunity the Ph.D. study and the continuous support for the related research. I would like to also thank my master's supervisors Prof. Xudong Wang and Prof. Xiaozhuo Xu at Henan Polytechnic University, especially for their support for my short-term overseas exchange during my master's period.

Besides my supervisors, I would like to thank the rest of my thesis committee: Prof. Yasuhide Tsuji, and Prof. Hideki Kawaguchi, for their insightful comments and encouragement from various perspectives. I want to thank Prof. Takahiro Sato. His advice helped me write the technical papers.

Thanks to my senior fellow apprentice, Shiyang Fang, Hiroto Otsuki, Ren Ishisone, etc. I got to know them during a short-term exchange when I first came to Muroran Institute of Technology in 2019, and became friends since then, and got along with them for a longer time when I came to Muroran Institute of Technology again for a Ph.D. They are the few Japanese friends I have, and I thank them for their warm help and for bringing happiness to my life in Japan. Although I will no longer have the opportunity to meet them after graduation, they are all lifelong friends of mine.

I would like to acknowledge the financial, academic, and technical support of the Muroran Institute of Technology and the financial support from the Japan Science and Technology Agency, which has brought me many opportunities to attend academic conferences and to publish our works in journals.

Finally, I would like to thank my parents and my family. One's parents are destined to be the most important people in one's life, both in terms of animal and social attributes, and this is especially true for the Chinese civilization, which is centered on family culture. It seems that just a second ago, my parents in my mind were still teaching me to tie my shoes and ride a bicycle. When I opened my eyes, my parents were both over half a century old, with gray temples. Because I was born into a not-so-rich, senior intellectual family, my parents always supported my studies as much as they could. Ph.D. is the highest degree in this society. The steady and unfailing support of my parents during my 22 years of student life, from choosing schools in elementary, middle, and high school, to applying for university and providing living expenses, is the prerequisite for me to be able to bring this doctoral thesis into the world. I believe they were pleased and proud to see me attending the graduation ceremony. The world is unpredictable, and when I enter society soon after, I will definitely encounter more complicated situations than my student career. I am already prepared and have the courage to deal with them. I hope to have the opportunity to continue making progress in the future, to view the world, society, and myself from a higher dimension, and not to waste the difficulty I have endured along the way. If I can bring some interesting things to the world to bring something good to others while progressing myself, it will be the best.

謝辞

まず、博士課程の指導教員である渡邊浩太教授に、博士課程に進学機会を与えてくださったこと、そして研究を継続的に支援してくださったことに、心から感謝申し上げます。 また、修士課程の指導教員である河南理工大学の汪旭東教授と许孝卓教授のご指導、特に修士課程中に協定校の交換留学生プログラムへの参加を支援していただいたことに感謝いたします。

指導教官のほか、論文指導委員の辻寧英教授、川口秀樹教授には、さまざまな観点から洞察力に富んだコメントと激励をいただきましたことに感謝いたします。また、佐藤孝洋准教授には、より分かりやすい学術論文を書くためのアドバイスをいただき、感謝申し上げます。

先輩である房世阳さん、大槻寛人さん、石曽根蓮さんに感謝します。2019 年に交換留学生として初めて室工大に来た時に出会い、それ以来友人となり、博士課程の進学で再び室工大に来た時により良い友達にりました。彼らは私にとって数少ない日本の友人であり、私の日本での生活を楽しくしてくれることに感謝しています。

室工大の経費的、学習的、個人生活的のサポートと日本科学技術振興機構の奨学金により、学会への参加や雑誌への成果発表の機会を与えていただいたことに感謝いたします。

最後に、私の両親と家族に感謝したい。人の両親は、動物的にも社会的属性的にも、その人の人生において最も重要な人物となる運命にあり、家族文化を中心とする中華文明では特にそうである。前の瞬間のように、私の頭の中では両親がまだ靴ひもを結び、自転車に乗りなさいと教えていたようですが、目を開けると、両親はすでに 50 歳を過ぎて、両鬢はシルバーになってる。私は高級知識分子でも裕福ではない家庭に生まれたため、幼い頃から両親は私の学習を最大限にサポートしてくれました。博士はすでに最高の学位であり、小学校、中学校、高校の学校選択から、大学の受験や生活費の提供まで、22 年間の学生生活の中で両親の安定的ない支持は私が安心してこの博士論文を世界に持っていくことができる前提です。彼らは卒業式に参加した私を見て、喜んで、誇りにに思っていると思う。世の中は予測不可能で、将来のことは学生時代のキャリアよりも複雑になっていくが、自分には勇気がある。私はこれからも進歩し続け、より高い次元から世界を見て、社会を見て、自分を見て、これまで経験した困難を無駄にしないことを望んでいます。自分が進歩しながら、世の中に面白いもの、他人の生活にも良いものをもたらすことができれば最高です。

致谢

首先，我想对我的博士生导师渡边浩太教授表示衷心的感谢，感谢他接纳我来日本交流，提供了继续攻读博士学位的机会，以及对相关研究的持续支持。我还要感谢我的硕士生导师河南理工大学的汪旭东教授和许孝卓教授对我的指导，特别是感谢他们对我硕士期间参加合作院校交换生项目的支持。

除了我的导师，我还要感谢我的论文指导委员会的辻寧英教授和川口秀樹教授，感谢他们从不同角度提出的有见地的意见和鼓励。感谢佐藤孝洋副教授，在他的建议下我写出了更加易读的学术论文。

感谢日本研究室的前辈，房世阳、大槻寛人、石曾根蓮等人。在 2019 年第一次来室兰工业大学做交换生时中认识了他们，从此成为朋友，再次来室兰工业大学读博士时有了更久的相处，他们是我为数不多的日本朋友，感谢他们的热情和帮助，为我在日本的生活带来快乐。虽然毕业后不再有机会见到他们，但他们都是我一生的朋友。

我要感谢室兰工业大学对经费、学习和个人生活上的支持，以及来自日本科学技术振兴机构的全额奖学金的支持，这不但使我可以安心研究，还给了我们更多参加学术会议和在科技期刊上发表成果的机会。

最后，我想感谢我的父母和家族。一个人，无论从动物属性还是社会属性来说，父母都注定是生命中最重要的人，对于以家庭文化为中心的中华文明更是如此。仿佛上一秒，脑海里的父母还在教我自己系鞋带，骑单车，睁开眼，父母均已年过半百，两鬓斑白。出生于一个并不富裕高知家族，从小父母就对我的学习给予了很大的期待，并提供了能力范围内的最大支持。博士已经是最高学位了，从小学，初中，高中的择校，到大学的报考和生活费的提供，22 年求学生涯中来自父母的稳定且不遗余力的支持是我能安心把这篇博士论文带到世界上的前提。相信他们看到参加毕业典礼的我时是欣慰且自豪的。世事难料，未来进入社会后一定会遇到比学生生涯更加复杂的局面。“仰天大笑出门去，我辈岂是蓬蒿人”，日子总会越过越好，一个人在他乡求学和生活经历已使我有勇气来独当一面。希望以后能有机会继续进步，能从更高的维度来看待世界，看待社会，看待自己，也不枉一路以来吃过的苦，如果能在自己进步的同时能为世间带来一些有趣的东西，为别人的生活也带来一些美好，那就赚了。

ABSTRACT

With the electrification trend of electric vehicles and industrial machines, more and more attention has been paid to electric motors. As a conversion device of electrical energy and mechanical energy, the performance of the motor will directly determine the competitiveness of the product. The performance of a motor is basically determined by the motor structure, which can be optimized by many different methods according to the way of shape expression. The topology optimization method is a kind of state-of-art method for structural optimization, in this method, the material can be freely distributed in the design domain. Compared with other geometry design methods such as the size design and shape design, topology optimization has the highest freedom to express the shape. Topology optimization was first used in the design of mechanical structures, and so far it has been extended to more fields, such as the design of electromagnetic devices and electric motors.

The purpose of this study is to broaden the application boundaries of topology optimization techniques in the design of electric motors. The author believes that there may be unexpected discoveries using topology optimization techniques to design iron cores in electric motors by topology optimization method as the optimized core can modulate the flux distribution. To this end, a typical topology optimization method - the ON/OFF method, is introduced for four interesting research topics, and the research findings are elaborated.

In the first research topic, the ON/OFF method is introduced into the design of the consequent-pole permanent magnet motor. The consequent-pole permanent magnet motor is a kind of special motor, it has attracted much attention in recent years due to its advantages of saving the amount of permanent magnets. As the design findings, it has been confirmed that the cogging torque and torque ripple of the motor can be suppressed to a rather low level if the iron poles are carefully designed.

In the second research topic, the ON/OFF method is introduced into the design of permanent magnet synchronous linear motors, and it is found that the end effect, which was considered an inherent defect of permanent magnet synchronous linear motors, can be almost eliminated.

In the third research topic, the ON/OFF method co-works with the electromagnetic-structural Multiphysics simulation to reduce the stator vibration of a switched reluctance motor. It is found that opening a inner window on the rotor poles and adopting anchor-shaped rotor pole are two design techniques for reducing radial electromagnetic force and stator vibration.

In the last research topic, aiming at the problem that both topology optimization and parameter optimization are simultaneously needed in the design of permanent magnet synchronous motor, a technique of coupling topology optimization and parameter optimization is proposed. A multi-objective optimization design of a permanent magnet synchronous motor

is carried out using the proposed technique, and the numerical results show that the proposed method can be used in the early conceptual design of a permanent magnet synchronous motor.

Overall, the author has conducted a series of studies on the design of some special motors and topology optimization - a state of art structural design method, out of author's interests and research bases, in the hope that this paper can provide a reference for researchers in academia and engineers in industry.

論文内容の要旨

電気自動車や産業機械の電動化に伴い、電気モーターへの注目度が高まっている。電気エネルギーと機械エネルギーの変換装置である電気モーターの性能は、生産品の競争力を直接左右することになる。電気モーターの性能は基本的にモーターの形状で決まる。構造最適化(structural optimization)手法は、形状表現手法によるサイズ最適化(size optimization)、形状最適化(shape optimization)、トポロジー最適化(topology optimization)の3種類に分類できる。トポロジー最適化法は、構造最適化の最先端手法であり、この手法では、設計領域で材料を自由に分布させることができる。サイズ設計や形状設計といった他の形状設計手法と比較して、トポロジー最適化は形状表現の自由度が最も高い手法である。トポロジー最適化は、機械構造物の設計で初めて用いられ、現在では、電磁デバイスや電気モーターの設計など、より多くの分野へ拡大されている。

本研究の目的は、電気モーターの設計におけるトポロジー最適化手法のプロモーションである。最適化された回転子は磁束分布を適切に分布させることができるため、トポロジー最適化手法を用いて電気モーターの鉄心を設計することで、思わぬ発見があるか期待できる。本研究では、4つの興味深い研究課題について、トポロジー最適化手法であるON/OFF法を導入した。

一つ目の研究課題では、consequent-pole型永久磁石モータの設計にON/OFF方式を導入した。consequent-pole型永久磁石モータは特殊なモータの一種であり、永久磁石の使用量を節約できる利点から近年注目されている。トポロジー最適化により，ローター鉄心の最適化を行ったところ、モータのコギングトルクやトルクリップルをかなり低く抑えられることが確認できた。

二つ目の研究課題では，永久磁石同期リニアモータの設計にON/OFF法を導入し，永久磁石同期リニアモータの固有の欠陥とされていたend-effectをほぼ解消できることを明らかにした。

三つ目の研究課題では、スイッチドリラクタンスモータのステータ振動を低減するために、ON/OFF法と電磁-構造マルチフィジックスシミュレーションを結合した。その結果、ローターポールに内窓を設けることと、アンカー型ローターポールを採用することが、半径方向の電磁力とステーター振動を低減する2つの設計手法であることがわかった。

四つ目の研究課題では、永久磁石同期モータの設計において、トポロジー最適化とパラメータ最適化の両方が同時に必要であるという問題に着目し、トポロジー最適化とパラメータ最適化を連動させるハイブリッド最適化手法を提案するものである。提案手法を用いて永久磁石同期モータの多目的最適化設計を行い、数値解析の結果、提案手法が永久磁石同期モータの初期概念設計に利用可能であることを示し

た。

本論文で示したた特殊モーターの設計事例と最先端の構造設計手法であるトポロジー最適化の適用研究が研究者やエンジニアの参考になることが期待できる。

INDEX

1 Introduction

1.1 Research background

With the electrification of electric vehicles and industrial machines, more and more attention has been paid to electric motors. As a conversion device of electrical energy and mechanical energy, the performance of the motor will directly determine the competitiveness of the product.

Because the shape of the motor determines the performance of the motor, the design of the motor shape is an important topic. In order to develop high-performance motors, the process of shape optimization is indispensable. Typically, the finite element method (FEM) is used to evaluate the performance of a motor, which is a numerical method that numerically approximates an unsolvable analytical solution [1][2]. However, the shape design of the motor is ever-changing, even for a skilled engineer, it will be a rather time-consuming task to use finite element evaluation for many motor designs.

In the above context, it is essential to develop an automated process of shape generation, finite element analysis, and performance evaluation for the shape design of electric motors, so that automatic design can be accomplished by computer, thus freeing designers from the tedious and boring motor design work.

The shape optimization of motors can be divided into two types [3][4], one is parameter optimization (PO) and the other is topology optimization (TO). In parameter optimization, the designer first describes the shape with some parameters, and then optimizes these parameters to optimize the shape. Because of limited parameter changes, parameter optimization can be completed in a short time, but the results of parameter optimization are often affected by the engineer's experience, because each engineer's method of shape parameterization is often different. Meanwhile, in parameter optimization, the change of shape is not free but limited by parameters. On the other hand, in topology optimization, the shape is not limited by parameters and the material can be freely distributed in space. In other words, in topology optimization,

shapes can be freely deformed, and holes can be freely created or annihilated. Thus, topology optimization has the potential to find innovative shapes beyond the imagination of designers.

The concept of topology optimization originated in the field of mechanics [3]-[5]. At present, topology optimization has been widely used in the field of mechanical design. As shown in Figure 1-1, the design of bicycle body through topology optimization technology achieves the effect of high strength and light weight. Topology optimization technology is being actively extended to various design areas, such as optoelectronic equipment [6], heat transfer devices [7], motors and so on.

Fig. 1-1 The optimal design of bicycle body through topology optimization method (source: https://nlab.itmedia.co.jp/nl/articles/1605/22/news015.html)

1.2 Research purposes

The purpose of this study is to broaden the application boundaries of topology optimization techniques in motor design. The author believe that there may be unexpected discoveries using topology optimization techniques to design iron cores to modulate the magnetic field in electric motors.

For this reason, in the chapter 3, the topology optimization technique is introduced into the

design of the consequent-pole permanent magnet motor, and it is found that the cogging torque and torque ripple of the motor can be suppressed to a rather low level.

In the chapter 4, the topology optimization technology is introduced into the design of linear motors, and it is found that the edge effect, which was considered as an inherent defect of linear motors, can be almost eliminated.

Chapter 5 studies the design of low-vibration switched reluctance motors by combining topology optimization technology and Multiphysics analysis technology. opening a inner window on the rotor poles and adopting anchor-shaped rotor pole are two design techniques to reduce radial electromagnetic force and stator vibration. After these two techniques, the vibration amplitude of the motor stator can be reduced by more than 30%.

In the chapter 6, aiming at the problem that both topology optimization and parameter optimization are simultaneously needed in the design of permanent magnet synchronous motor, a technique of coupling topology optimization and parameter optimization is proposed. A multi-objective optimization design of a permanent magnet synchronous motor is carried out using the proposed technique, and the numerical results show that the proposed method can be used in the early conceptual design of a permanent magnet synchronous motor.

Figure 1-2 expresses the context of this paper. In short, based on topology optimization technology, this paper conducts a series of exploratory research on some motor design issues. Figure 1-3 classify the research content from the perspective of theory and application. The third, fourth and fifth chapters are biased towards the application research of topology optimization technology, while the sixth chapter is biased towards the theoretical research of topology optimization technology.

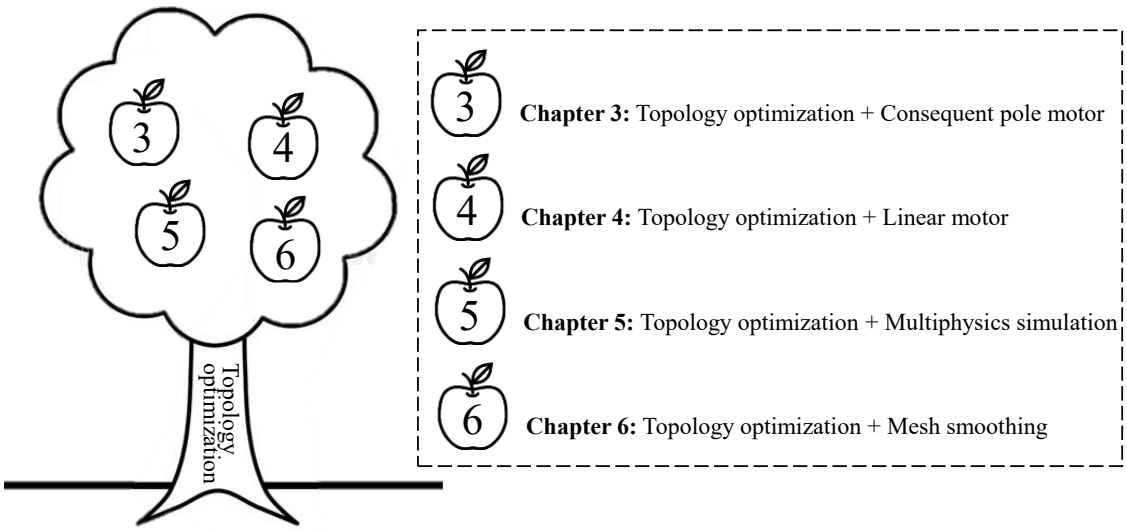

Fig. 1-2 Contents of the studies

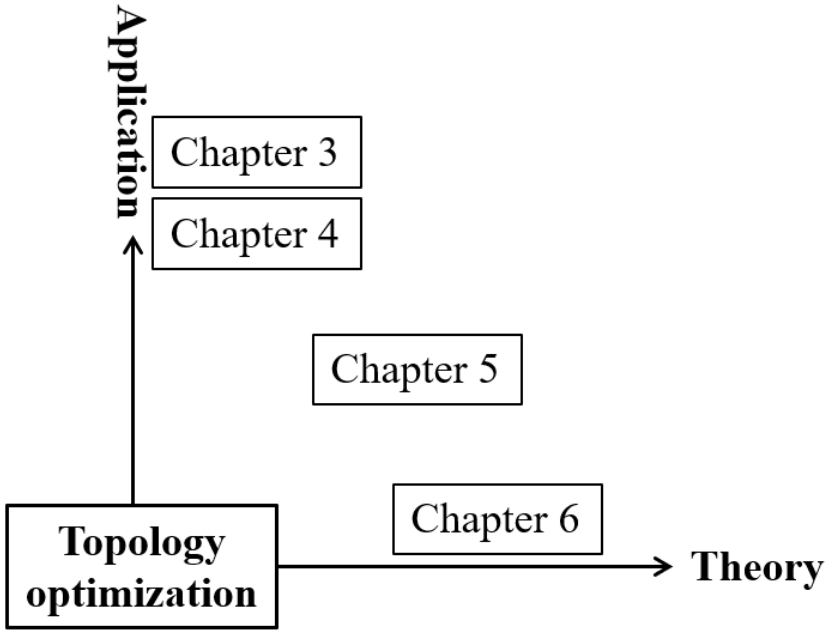

Fig. 1-3 classifications of the studies

2 Numerical calculation method

2.1 Finite element method

Exact solutions to boundary value problems for elliptic partial differential equations can be found analytically when the shape of the region is geometrically simple, such as a rectangle or an ellipse. It is not easy to analytically obtain the exact solution of the complex shape seen. For such problems, the finite element method is widely known as one of the numerical solution methods that can always obtain an approximate solution even if an exact solution is impossible. Error analysis is possible for approximate solutions by the finite element method, and it is reliable that convergence to exact solutions is guaranteed by increasing the number of element divisions. The formulation of the finite element method is roughly divided into the following three components.

(1). Strong form consisting of governing equations and boundary conditions for the model;

(2). Weak form;

(3). Approximate function (discretization).

2.2 Formulation in two-dimensional static magnetic field analysis

2.2.1 Strong form

A strong form consists of the governing equations and boundary conditions. To derive the governing equations, we present Maxwell's equations. When considering a two-dimensional static magnetic field, the displacement current term in Ampere's law and the time derivative term on the right side of Faraday's law are set to 0.

$$\nabla \times H = J \tag{2-1}$$

$$\nabla \times E = 0 \tag{2-2}$$

$$\nabla \cdot B = 0 \tag{2-3}$$

$$\nabla \cdot D = \rho \tag{2-4}$$

where $\boldsymbol{H}$ is the magnetic field strength, $\boldsymbol{B}$ is the magnetic flux density, $\boldsymbol{E}$ is the electric field

strength, $\boldsymbol{D}$ is the electric flux density, ρ is the charge density, and $\boldsymbol{J}$ is the current density.

$$B = \mu H \tag{2-5}$$

$$D = \varepsilon E \tag{2-6}$$

$$J = \sigma E \tag{2-7}$$

where μ, ε, σ are permeability, permittivity, and conductivity, respectively. Although these are tensor quantities, we assume an isotropic material in this study.

Let $\boldsymbol{A}$ be any vector that satisfies the vector formula shown in equation (2-8)

$$\nabla \cdot \nabla \times A = 0, \forall A \tag{2-8}$$

From Equation (2-3), $\boldsymbol{B}$ can be expressed as in equation (2-9), where $\boldsymbol{A}$ is called the magnetic vector potential.

$$B = \nabla \times A \tag{2-9}$$

Since the magnetic vector potential has only the z component in the two-dimensional static magnetic field, we transform Equation (2-9) for the z component as

$$B = \nabla \times A = \left(\frac{\partial A_z}{\partial y}, -\frac{\partial A_z}{\partial x}\right) = \nabla A_z \times e_z \tag{2-10}$$

Substitute Equation (2-5) and (2-10) into Equation (2-1). At this time, since the current density has only the z component in the two-dimensional static magnetic field

$$\nabla \times \left(\frac{1}{\mu}\nabla A_z \times e_z\right) = J e_Z \tag{2-11}$$

Applying Equation (2-12) to the left side of Equation (2-11)

$$\nabla \times (a \times b) = (b \cdot \nabla)a - (a \cdot \nabla)b + a\nabla \cdot b - b\nabla \cdot a \tag{2-12}$$

we get

$$\nabla \times \left(\frac{1}{\mu}\nabla A_z \times e_z\right) = (e_z \cdot \nabla)\frac{1}{\mu}\nabla A_z - \left(\frac{1}{\mu}\nabla A_z \cdot \nabla\right)e_z + \frac{1}{\mu}\nabla A_z(\nabla \cdot e_z) - e_z\left(\nabla \cdot \frac{1}{\mu}\nabla A_z\right)$$

$$= -e_z\left(\nabla \cdot \frac{1}{\mu}\nabla A_z\right) \tag{2-13}$$

Substituting Equation (2-13) into Equation (2-11), we obtain the governing equation of the

two-dimensional static magnetic field

$$\nabla \cdot \frac{1}{\mu} \nabla A_z + J = 0 \tag{2-14}$$

About Strong Form Boundary Conditions. In the following, let the analysis region be Ω and the analysis boundary be Γ.

There are two types of boundary conditions, and at any point on the boundary, either the magnetic vector potential $\boldsymbol{A}$ or the magnetic field strength $\boldsymbol{H}$ in the normal direction must be defined, and both cannot be defined at the same time. Let Γ_A be the default boundary of magnetic vector potential $\boldsymbol{A}$ and Γ_H be the default boundary of magnetic field strength $\boldsymbol{A}$.

$$\Gamma_A \cup \Gamma_H = \Gamma, \ \Gamma_A \cap \Gamma_H = \emptyset \tag{2-15}$$

The default boundary conditions for the magnetic vector potential $\boldsymbol{A}$ is defined as follows.

$$A(x, y) = \bar{A}(x, y) \quad (on\ \Gamma_A) \tag{2-16}$$

where $\bar{A}$ is the default magnetic vector potential. This is called the basic boundary condition. Since the magnetic field strength $\boldsymbol{H}$-default boundary defines the strength of the magnetic field in the normal direction, the boundary condition is

$$H(x, y) \times n = 0 \quad (on\ \Gamma_H) \tag{2-17}$$

This is called the natural boundary condition.

2.2.2 Weak form

In order to derive the finite element equations, the partial differential equation must be transformed into what is called a weak integral form. The weak and strong forms are equivalent.

Multiply the strong forms Equations (2-14) and (2-17) by an arbitrary differentiable function $w(x, y)$ and integrate over the region Ω and boundary Γ_H, respectively.

$$\iint_{\Omega_l} w(\nabla \cdot \frac{1}{\mu} \nabla A_z + J)\, d\Omega \tag{2-18}$$

$$\oint_{\Gamma_H} w(H \times n)\Gamma = 0 \tag{2-19}$$

After the Green's formula in Equation (2-20) is applied to the first term on the left-hand side of Equation (2-18), the Equation (2-21) can be got.

$$\iint_{\Omega_l} w\nabla \cdot \nu \, d\Omega = \oint_{\Gamma} w\nu \cdot n d\Gamma - \iint_{\Omega_l} \nabla w \cdot \nu \, d\Omega \tag{2-20}$$

$$\oint_{\Gamma} w\frac{1}{\mu}\nabla A_z \cdot n d\Gamma - \iint_{\Omega_l} \nabla w \cdot \frac{1}{\mu}\nabla A_z d\Omega + \iint_{\Omega_l} wJ d\Omega = 0 \tag{2-21}$$

For the first term on the left-hand side of Equation (2-21), the analytical boundary Γ, which is the path of integration, consists of the natural boundary Γ_H and the fundamental boundary Γ_A from (2-15), so the expression can be transformed as follows

$$\oint_{\Gamma} w\frac{1}{\mu}\nabla A_z \cdot n d\Gamma = \oint_{\Gamma_H} w\frac{1}{\mu}\nabla A_z \cdot n d\Gamma + \oint_{\Gamma_A} w\frac{1}{\mu}\nabla A_z \cdot n d\Gamma \tag{2-22}$$

On the natural boundary, from Equation (2-9) and the natural boundary conditions in Equation (2-17).

$$H(x,y) \times n = 0 \rightarrow \frac{1}{\mu}(\nabla \times A_z) \times n = 0$$

Expanding on it with respect to the components

$$\frac{1}{\mu}\left(\frac{\partial A_z}{\partial y}, -\frac{\partial A_z}{\partial x}\right) \times n = \frac{1}{\mu}\left(\frac{\partial A_z}{\partial x}n_x + \frac{\partial A_z}{\partial y}n_y\right) e_z = \frac{1}{\mu} \bigtriangledown A_Z \cdot n = 0 \tag{2-23}$$

Therefore, substituting Equation (2-23) into Equation (2-19), we find that the first term on the right side of Equation (2-22) becomes 0.

On the fundamental boundary.

Assuming that there is no outward magnetic flux leakage on the fundamental boundary, the second term on the right side of Equation (2-22) disappears if the weight function w is set to 0 due to its arbitrariness.

Therefore, from the natural and basic boundary conditions, the weak form used in the two-dimensional static magnetic field analysis is

$$\iint_{\Omega} \bigtriangledown w \cdot \frac{1}{\mu} \bigtriangledown A_Z d\Omega = \iint_{\Omega} wJ d\Omega \tag{2-24}$$

2.2.3 Weak form discretization

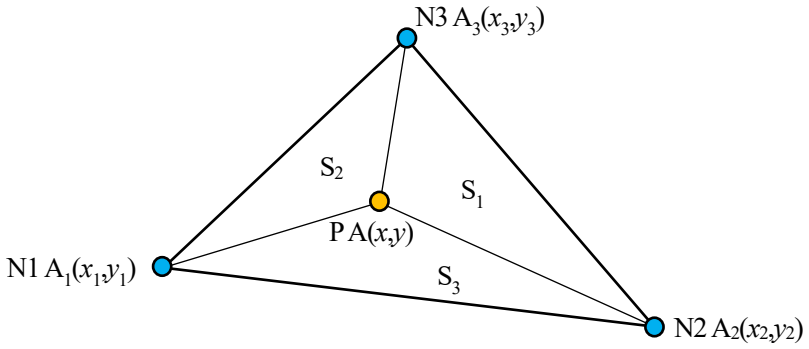

Fig. 2-1 Potential approximated by a triangular mesh.

The finite element method divides the problem domain into elements and constructs weight functions and magnetic vector potentials contained in weak forms by defining functions within each element. When dividing the analysis domain with a triangular mesh. Assuming the magnetic vector potential A at an arbitrary point P within the triangular element using arbitrary coefficients r, s, t.

$$A = r + sx + ty \tag{2-25}$$

For a magnetic vector potential A at any point P in a triangular element and magnetic vector potentials A_1, A_2, and A_3 at each vertex of the triangular element, the following equation holds

$$\begin{bmatrix} A_1 \\ A_2 \\ A_3 \end{bmatrix} = \begin{bmatrix} r & sx_1 & ty_1 \\ r & sx_2 & ty_2 \\ r & sx_3 & ty_3 \end{bmatrix} \tag{2-26}$$

Solving Equation (2-26) for the unknown coefficients r, s, t

$$\begin{bmatrix} r \\ s \\ t \end{bmatrix} = \begin{bmatrix} 1 & x_1 & y_1 \\ 1 & x_2 & y_2 \\ 1 & x_3 & y_3 \end{bmatrix}^{-1} \begin{bmatrix} A_1 \\ A_2 \\ A_3 \end{bmatrix} \tag{2-27}$$

For the coefficient matrix on the right-hand side of Equation (2-27), let this be

$$\begin{bmatrix} 1 & x_1 & y_1 \\ 1 & x_2 & y_2 \\ 1 & x_3 & y_3 \end{bmatrix}^{-1} = \frac{1}{2\Delta} \begin{bmatrix} x_2y_3 - x_3y_2 & x_3y_1 - x_1y_3 & x_1y_2 - x_2y_1 \\ y_2 - y_3 & y_3 - y_1 & y_1 - y_2 \\ x_3 - x_2 & x_1 - x_3 & x_2 - x_1 \end{bmatrix} = \frac{1}{2\Delta} \begin{bmatrix} a_1 & a_2 & a_3 \\ b_1 & b_2 & b_3 \\ c_1 & c_2 & c_3 \end{bmatrix} \tag{2-28}$$

where Δ is defined as

$$\Delta = \frac{1}{2}\begin{vmatrix} 1 & x_1 & y_1 \\ 1 & x_2 & y_2 \\ 1 & x_3 & y_3 \end{vmatrix} \tag{2-29}$$

Substituting Equation (2-27) into Equation (2-25), we obtain

$$A = [1 \quad x \quad y]\begin{bmatrix} r \\ s \\ t \end{bmatrix} = [1 \quad x \quad y]\begin{bmatrix} 1 & x_1 & y_1 \\ 1 & x_2 & y_2 \\ 1 & x_3 & y_3 \end{bmatrix}^{-1}\begin{bmatrix} A_1 \\ A_2 \\ A_3 \end{bmatrix} =$$

$$[1 \quad x \quad y]\frac{1}{2\Delta}\begin{bmatrix} a_1 & a_2 & a_3 \\ b_1 & b_2 & b_3 \\ c_1 & c_2 & c_3 \end{bmatrix}\begin{bmatrix} A_1 \\ A_2 \\ A_3 \end{bmatrix} =$$

$$\frac{1}{2\Delta}[a_1 + b_1x + c_1y \quad a_2 + b_2x + c_2y \quad a_3 + b_3x + c_3y]\begin{bmatrix} A_1 \\ A_2 \\ A_3 \end{bmatrix} \tag{2-30}$$

If the interpolation function $[N]$, where the magnetic vector potential A at an arbitrary point P in the triangular element is represented by the nodal magnetic vector potentials A_1, A_2, and A_3 is defined as follows

$$[N] = \frac{1}{2\Delta}[a_1 + b_1x + c_1y \quad a_2 + b_2x + c_2y \quad a_3 + b_3x + c_3y] \tag{2-31}$$

Equation (2-30) becomes

$$A = [N]\{A_i\} \quad i = 1,2,3 \ldots \tag{2-32}$$

Next, we apply the Galerkin method to the weak form of (2-24). The Galerkin method is a method that uses an interpolation function $[N]$ for the weighting function w.

$$\sum_{l=1}^{ne} \iint_{\Omega_l} \nabla N_i \cdot \left(\frac{1}{\mu}\nabla A_Z\right)_l d\Omega = \sum_{l=1}^{ne} \iint_{\Omega_l} N_i J_l d\Omega$$

By expressing Az in terms of interpolation functions

$$\sum_{l}^{ne} \frac{1}{\mu_l} \int_{\Omega_l} \nabla N_i \cdot \sum_{j=1}^{3} \nabla N_j^{(l)} A_j^{(l)} d\Omega = \sum_{l=1}^{ne} \iint_{\Omega_l} N_i J_l d\Omega \tag{2-33}$$

where ne is the total number of elements, i is the total node number, $N(l)$, $A(l)$ are the

interpolation function and the magnetic vector potential of the l-th element node. While checking all the elements, $Ni = 0$ if the node of the l-th element does not include the node number i.

About $\boldsymbol{\nabla} N$, from Equation (2-31)

$$N_k = \frac{1}{2\Delta}(a_k + b_k x + c_k y), k = 1,2,3 \ldots \tag{2-34}$$

Therefore

$$\nabla N_k = \left(\frac{\partial N_k}{\partial y}, \frac{\partial N_k}{\partial x}\right) = \left(\frac{b_k}{2\Delta}, \frac{c_k}{2\Delta}\right) \tag{2-35}$$

The left-hand side of Equation (2-33) is therefore

$$\sum_{l=1}^{ne} \frac{1}{\mu_l} \iint_{\Omega_l} \left(\frac{b_i}{2\Delta}, \frac{c_i}{2\Delta}\right) \cdot \sum_{j=1}^{3} \left(\frac{b_j}{2\Delta}, \frac{c_j}{2\Delta}\right)^{(l)} A_j^{(l)} \, d\Omega =$$

$$\sum_{l=1}^{ne} \frac{1}{\mu_l} \iint_{\Omega_l} \sum_{j=1}^{3} \left(\frac{b_i}{2\Delta}\frac{b_j}{2\Delta}, \frac{c_i}{2\Delta}\frac{c_j}{2\Delta}\right)^{(l)} A_j^{(l)} \, d\Omega \tag{2-36}$$

That is, for the e-th element, it can be expressed as

$$K_{ij}^{(e)} = \frac{1}{\mu_e} \iint_{\Omega_e} \left(\frac{b_i}{2\Delta}\frac{b_j}{2\Delta} + \frac{c_i}{2\Delta}\frac{c_j}{2\Delta}\right) d\Omega \tag{2-37}$$

$$b_i^{(e)} = \iint_{\Omega_e} N_i J_e \, d\Omega \tag{2-38}$$

As an example, for an element with element number 0 and node numbers 0, 1 and 11, the left-hand side of Equation (2-37) and the nodal The magnetic vector potentials of

$$[K^{(0)}]\{A^{(0)}\} = \begin{bmatrix} K_{0,0}^{(0)} & K_{0,1}^{(0)} & K_{0,11}^{(0)} \\ K_{1,0}^{(0)} & K_{1,1}^{(0)} & K_{1,11}^{(0)} \\ K_{11,0}^{(0)} & K_{11,1}^{(0)} & K_{11,11}^{(0)} \end{bmatrix} \begin{bmatrix} A_0 \\ A_1 \\ A_{11} \end{bmatrix} \tag{2-39}$$

Letting $[K(e)]$ be the element stiffness matrix for element number e, the element stiffness matrix in Equation (2-39) is

$$\left[K^{(0)}\right] = \frac{1}{4\Delta\mu_{(0)}}\begin{bmatrix} b_0b_0 + c_0c_0 & b_0b_1 + c_0c_1 & b_0b_{11} + c_0c_{11} \\ b_1b_0 + c_1c_0 & b_1b_1 + c_1c_1 & b_1b_{11} + c_1c_{11} \\ b_{11}b_0 + c_{11}c_0 & b_{11}b_1 + c_{11}c_1 & b_{11}b_{11} + c_{11}c_{11} \end{bmatrix} \tag{2-40}$$

The same work is carried out for element 1. If element 1 has element number 1 and node numbers 1, 11 and 12, then the left-hand side of Equation (2-37) and the magnetic vector potentials at the nodes are

$$[K^{(1)}]\{A^{(1)}\} = \begin{bmatrix} K_{1,1}^{(1)} & K_{1,11}^{(1)} & K_{1,12}^{(1)} \\ K_{11,1}^{(1)} & K_{11,11}^{(1)} & K_{11,12}^{(1)} \\ K_{12,1}^{(1)} & K_{12,11}^{(1)} & K_{12,12}^{(1)} \end{bmatrix}\begin{bmatrix} A_1 \\ A_{11} \\ A_{12} \end{bmatrix} \tag{2-41}$$

The element stiffness matrix for element 0 and element 1 can be summarized as

$$\left[K^{(0)+(1)}\right] = \begin{bmatrix} K_{0,0}^{(0)} & K_{0,1}^{(0)} & \cdots & K_{0,11}^{(0)} & \\ K_{1,0}^{(0)} & K_{1,1}^{(0)} + K_{1,1}^{(1)} & \cdots & K_{1,11}^{(0)} + K_{1,11}^{(1)} & K_{1,12}^{(1)} \\ \vdots & \vdots & & \vdots & \vdots \\ K_{11,0}^{(0)} & K_{11,1}^{(0)} + K_{11,1}^{(1)} & \cdots & K_{11,11}^{(0)} + K_{11,11}^{(1)} & K_{11,12}^{(1)} \\ & K_{12,1}^{(1)} & \cdots & K_{12,11}^{(1)} & K_{12,12}^{(1)} \end{bmatrix} \tag{2-42}$$

Do this for all elements and get the following global stiffness matrix

$$[K] = \begin{bmatrix} k_{0,0} & k_{0,n} \\ & \\ k_{n,0} & k_{n,n} \end{bmatrix} \tag{2-43}$$

For the right-hand side vector $\{b\}$, area coordinates as Figure (2-2) are first introduced.

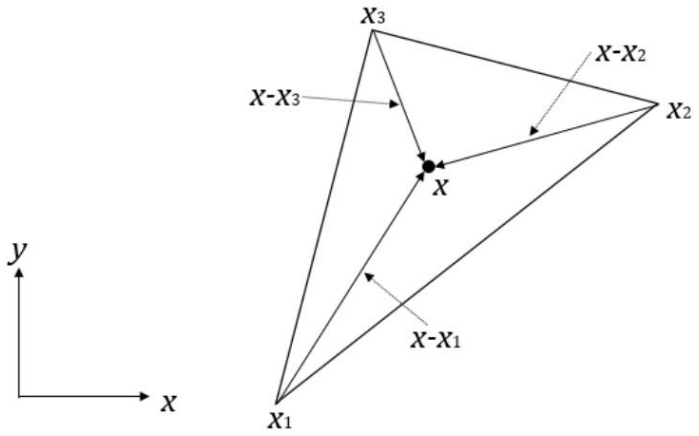

Fig. 2-2 Area coordinates.

Let $\boldsymbol{x_1}$, $\boldsymbol{x_2}$ and $\boldsymbol{x_3}$ be the position vectors of the three vertices, as shown in Figure 2-2.

For a position vector $\boldsymbol{x}$ at any point (x, y) inside the triangle, the three vectors $\boldsymbol{x}$ - $\boldsymbol{x_1}$, $\boldsymbol{x}$ - $\boldsymbol{x_2}$ and $\boldsymbol{x}$ - $\boldsymbol{x_3}$ are considered. Since these three vectors are vectors in the plane, they are linearly dependent. Therefore, the following equation holds.

$$a_1(x - x_1) + a_2(x - x_2) + a_3(x - x_3) = 0 \tag{2-44}$$

where a_1, a_2, a_3 are all scalar quantities that are not 0 at the same time.

Transforming Equation (2-44) to

$$x = \frac{a_1x_1+a_2x_2+a_3x_3}{a_1+a_2+a_3} \tag{2-45}$$

By Equation (2-45), we define

$$L_1 = \frac{a_1}{a_1+a_2+a_3}, L_2 = \frac{a_2}{a_1+a_2+a_3}, L_3 = \frac{a_3}{a_1+a_2+a_3} \tag{2-46}$$

Therefore, $\boldsymbol{x} = L_1\boldsymbol{x}_1 + L_2\boldsymbol{x}_2 + L_3\boldsymbol{x}_3$. In this case, L_1, L_2 and L_3 are called area coordinates. For these, $L_1 + L_2 + L_3 = 1$ holds.

Also, $0 \leq L_1, L_2, L_3 \leq 1$ from the condition that the position vector $\boldsymbol{x}$ is inside the triangle.

The area coordinates L_1, L_2 and L_3 can be used as shape functions of the triangular region. The shape function $[L]$ also corresponds one-to-one to the interpolation function $[N]$ in Equation (2-31).

$$[N]^T = \begin{bmatrix} N_1 \\ N_2 \\ N_3 \end{bmatrix} = \begin{bmatrix} L_1 \\ L_2 \\ L_3 \end{bmatrix} = [L]^T \tag{2-47}$$

In addition, the following integral formula holds for area coordinates.

$$\int \int_{\Omega} \quad L_1^{\alpha} L_2^{\beta} L_3^{\gamma} d\Omega = \frac{\alpha!\beta!\gamma!}{(\alpha+\beta+\gamma+2)!} 2\Delta \tag{2-48}$$

Δ is the area of the element.

As an example, consider element 0. Substituting Equation (2-47) into Equation (2-48), we obtain

$$\begin{cases} \iint_\Omega N_0^1 N_1^0 N_{11}^0 d\Omega = \frac{1!0!0!}{(1+0+0+2)!} 2\Delta = \frac{\Delta}{3} \\ \iint_\Omega N_0^0 N_1^1 N_{11}^0 d\Omega = \frac{0!1!0!}{(0+1+0+2)!} 2\Delta = \frac{\Delta}{3} \\ \iint_\Omega N_0^0 N_1^0 N_{11}^1 d\Omega = \frac{0!0!1!}{(0+0+1+2)!} 2\Delta = \frac{\Delta}{3} \end{cases} \quad (2\text{-}49)$$

Therefore, the right-hand side vector at element 0 is

$$\begin{bmatrix} b_0 \\ b_1 \\ b_{11} \end{bmatrix} = \begin{bmatrix} \frac{J_0\Delta}{3} \\ \frac{J_0\Delta}{3} \\ \frac{J_0\Delta}{3} \end{bmatrix} \quad (2\text{-}50)$$

By performing the same operation for all elements, we obtain the right-hand side vector $\{b\}$ of the following equation

$$\{b\} = \begin{bmatrix} \frac{J_0\Delta}{3} \\ \vdots \\ \frac{J_0\Delta}{3} \end{bmatrix} \quad (2\text{-}51)$$

2.2.4 Nodal force method

Methods of calculating electromagnetic force and torque by the finite element method include the Maxwell's stress method, equivalent magnetizing current method, modified energy method, and nodal force method . In this study, the nodal force method is used to calculate the electromagnetic force and torque. The nodal force method is a method of calculating the electromagnetic force acting on the entire magnetic body by obtaining the electromagnetic force acting on each vertex in the magnetic body.

The volume force f_v and the surface force f_s due to the magnetic field are expressed as follows using Maxwell's stress tensor T.

$$f_v = \nabla \cdot T \quad (5\text{-}52)$$

$$f_s = (T_2 - T_1) \cdot n \quad (5\text{-}53)$$

$$T = \frac{1}{2\mu}\begin{bmatrix} B_x^2 - B_y^2 & 2B_xB_y \\ 2B_xB_y & B_y^2 - B_x^2 \end{bmatrix} \tag{5-54}$$

where $\boldsymbol{n}$ is the normal vector from medium 1 to medium 2.

Using the interpolation function N_i that can continuously differentiate the virtual displacement u^*

$$u^* = \sum_i^{nn} N_i u_i^* \tag{5-55}$$

where nn is the total number of nodes. The energy variant δW for this distribution virtual displacement is

$$\delta W = \iint_\Omega (\nabla \cdot T)\, u^* d\Omega + \oint_\Gamma \{(T_2 - T_1) \cdot n\} u^* d\Gamma \tag{5-56}$$

Using the Green's formula in Equation (2-20) for the first term on the right side of Equation (2.87)

$$\delta W = \oint_\Gamma n \cdot T u^* d\Gamma - \iint_\Omega \nabla \delta u \cdot T d\Omega + \oint_\Gamma \{(T_2 - T_1) \cdot n\} u^* d\Gamma \tag{5-57}$$

In Equation (2-57), the first and third terms on the right-hand side cancel each other out.

$$\delta W = -\iint_\Omega \nabla \delta u \cdot T d\Omega \tag{5-58}$$

Substituting Equation (2-55) into it. We get

$$\delta W = \sum_i^{nn} (-\iint_\Omega T \cdot \nabla N_i \cdot \delta u_i) d\Omega \tag{5-59}$$

Since this can be expressed as

$$\delta W = \sum_i^{nn} f_i \tag{5-60}$$

We get

$$f_i = -\iint_\Omega T \cdot \nabla N_i d\Omega \tag{5-61}$$

The above equation is expressed in terms of components.

$$f_{xi} = -\iint_\Omega \left(T_{xx}\frac{\partial N_i}{\partial x} + T_{xy}\frac{\partial N_i}{\partial y}\right) d\Omega \tag{5-62-a}$$

$$f_{yi} = -\iint_{\Omega} \left(T_{yx}\frac{\partial N_i}{\partial x} + T_{yy}\frac{\partial N_i}{\partial y}\right) d\Omega \tag{5-62-b}$$

For the torque calculation method using the nodal force method, the torque T is obtained as the sum of the torques acting on each node.

$$T = \sum_i^{nn} r_i t_i f_i = \sum_i^{nn} \sqrt{x_i^2 + y_i^2} \left\{ \frac{-y_i}{\sqrt{x_i^2+y_i^2}}, \frac{x_i}{\sqrt{x_i^2+y_i^2}} \right\} \begin{Bmatrix} f_{xi} \\ f_{yi} \end{Bmatrix} = \sum_i^{nn} \left\{ y_i \iint_{\Omega} \left(T_{xx}\frac{\partial N_i}{\partial x} + T_{xy}\frac{\partial N_i}{\partial y}\right) d\Omega \right\} - \iint_{\Omega} \left(T_{yx}\frac{\partial N_i}{\partial x} + T_{yy}\frac{\partial N_i}{\partial y}\right) d\Omega \tag{5-62}$$

where r_i, t_i and f_i are the radius, unit tangent vector and nodal force from the center of node i respectively.

3 Topology optimization for consequent-pole machines

3.1 Consequent-pole permanent magnet synchronous machines

Consequent-pole permanent magnet synchronous machines (CP-PMSMs) are novel machines that raised much attention along with the increasing price and unstable supply of rare-earth permanent magnet (PM). Many published literatures have pointed out that CP-PMSMs are promising especially in cost-sensitive applications because they can save approximately one-third of amount of PM while maintaining almost the same torque density as their surface-mounted PM counterparts. Although many studies for CP-PMSM's performance enhancement design have been released [8]-[13], the design border of the iron poles is not meaningfully studied. The flux density under the iron pole it is mainly governed by the shape of iron poles. To put it in another way, the iron poles, which only take up a limited part in the CP-PMSMs, can be processed into various topologies to bring considerable performance dividends.

The aim of this study is to study multi-objective TO on the iron poles to unlock the full design space potential of a CP-PMSM. High average torque, as well as low torque ripple, are the optimization targets. Since the design region/variables is relatively small, and the TO is performed with some material distribution constraints, the ON/OFF method with evolutionary algorithm is used to solve this problem. In order to apply the multi-objective evolutionary algorithms (MOEAs) to the TO problem, a set of Delaunay mesh-based evolutionary operators is proposed and formulated to make modifications to the shape. Non-dominated Sorting Genetic Algorithm (NSGA)-II [14], and Strength Pareto Evolutionary Algorithm (SPEA)-II are utilized to solve the formulated problem [15]. Compared with the published multi-objective TO studies for electromagnetic devices [16]-[18], the multi-objective TO method in this paper is simple in both concept and practice. In addition, the Delaunay algorithm, which is the most standard method for 2D FE analysis, is used in this work to discretize the model. This makes the smoothing procedure can be easily introduced to eliminate jagged material boundaries. The

Delaunay meshes also allow this TO method to be easily coupled with commercial FE analysis software.

3.2 Machine configuration and modelling

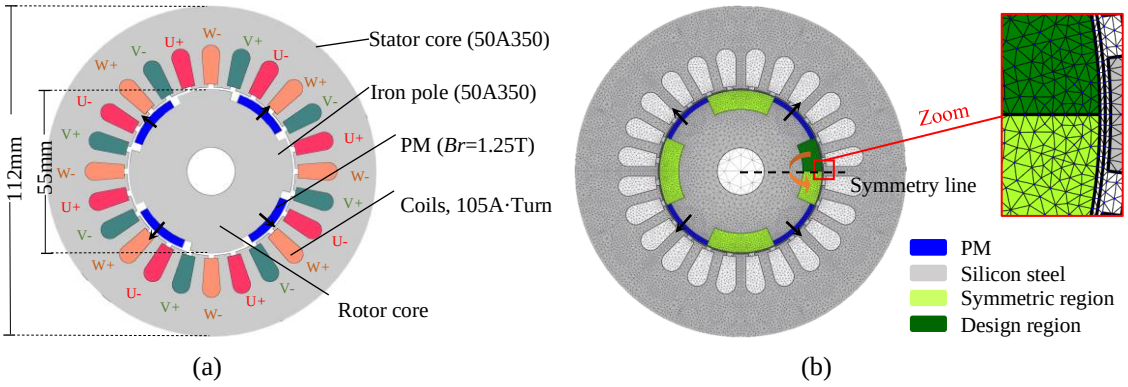

(a) (b)

Figure 3-1: (a) Cross-sections of the CP-PMSM for optimization, (b) Finite element model for optimization.

In a CP-PMSM, all the N poles or S poles are replaced by silicon iron poles. The iron poles can provide a magnetic path for the flux, which is passed easier than the magnetic path including PM poles. Many reported literatures about CP-PMSM's optimization chose PMs as object for optimization. For CP-PMSMs, the iron poles, which modulate the flux in the airgap, can be easily processed into various topologies. In contrast with the released literatures, which focus on the optimization of PM, this paper will optimize the topology of iron poles in a CP-PMSM by ON/OFF method to maximize the average torque and minimize the torque ripple. Figure 3-1 (a) shows the cross-section of the original CP-PMSM for optimization. It is a CP-PMSM that adopts 8-pole, including 4 PM poles and 4 silicon iron poles, and 24-slot. The parameters of this machine are based on a benchmark model from IEEJ [19]. Details of the machine can be found in Table 1. Considering the contribution to the output torque from the reluctance component can be neglected, the current advanced angle is set as 0°. Under this setting, the average torque and torque ripple simulated by FE method are 2.72 N·m and 2.17 N·m,

respectively.

Table 3-1: Specification of the CP-PMSM for optimization.

Number of poles	*8*	*Rotation speed*	*750rpm*
Number of slots	*24*	*PM permanence*	*1.25T*
Coils (per teeth)	*35*	*PM relative permeability*	*1.05*
Current (R.M.S.)	*3A*	*Laminated length*	*65mm*
Split ratio	*0.9*	*Airgap length*	*0.5mm*
Silicon steel	*JIS:50A350*	*PM height*	*1.5mm*

The machine is modelled by FE method. Delaunay algorithm is used for meshing. The four optimization regions, which will be managed by the ON/OFF method, are depicted in Figure 3-1 (b) as green color. Each region is discretized into 652 triangular elements. In the TO process, each element in these regions can freely take the magnetic characteristics of either iron or air, so as to recreate the topology of iron poles. The basis function-based material representation method is not used as this study aims to discover the best possible torque performance and design border of the CP-PMSM [20]-[21]. In order to reduce the time-consuming, the element material above the symmetry line will be mirrored below it, the optimized shape in one region will be copied to the other three regions. Therefore, the variables are reduced to 326.

3.3 Numerical methodology

In this section, the numerical methodology used for optimization and simulation is elaborated. The evolutionary operators under Delaunay-based triangular meshes are proposed and formulated, the coupling flow of MOEAs and FE calculation is described.

3.3.1 ON/OFF method and the modeling of motor

The optimization region is discretized into numerous cells in the ON/OFF method. The material in each cell is the optimization variable, which can freely take up “ON (material)” or “OFF (no material)” to represent different topologies. By using stochastic algorithms to search

a great variety of "ON"/"OFF" binary string combinations, the optimal material distribution can be found without violating constraints in the optimization region. In this paper, the Delaunay-based triangular FE elements in optimization regions are directly used as the cells in the ON/OFF method. The optimization regions cover the iron poles, "ON (iron)" and "OFF (air)" are used to represent the topology of the iron poles.

For this model, the field distribution in the design region is governed by:

$$\begin{cases} \nabla \times (\upsilon_{\mathbf{air}} \nabla \times \boldsymbol{A}) = \mathbf{0} & \textbf{if the state is "OFF (air)"} \\ \nabla \times (\upsilon_{\mathbf{iron}} \nabla \times \boldsymbol{A}) = \mathbf{0} & \textbf{if the state is "ON (iron)"} \end{cases} \tag{5-1}$$

where A, υ_air, and υ_iron denote magnetic vector potential, reluctivity of air, reluctivity of iron, respectively.

The silicon iron material is modelled by JIS 50A350 (JIS: Japanese Industrial Standard). The B-H data can be found in Figure 3-2.

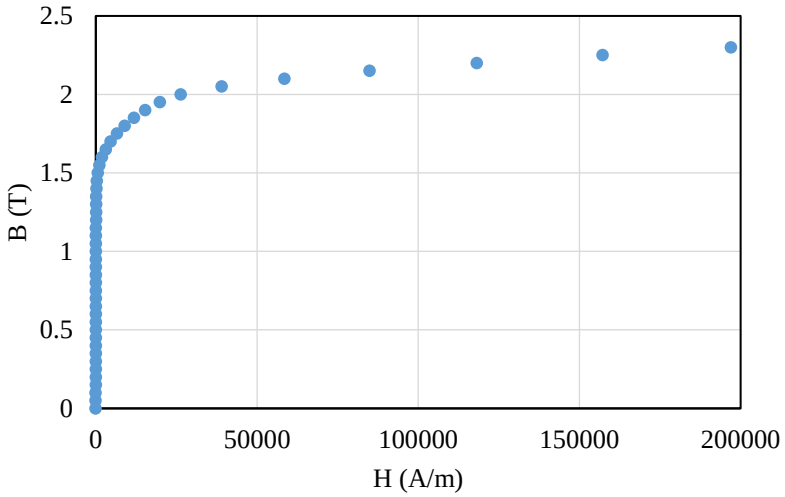

Figure 3-2: B-H data of silicon iron in FE calculation.

3.3.2 Filtering algorithm

The ON/OFF method often generates checkerboard structures when it is combined with stochastic algorithms. Since the existence isolated material block and jagged boundary, the checkerboard structures are non-feasibility in terms of the real-world engineering realization.

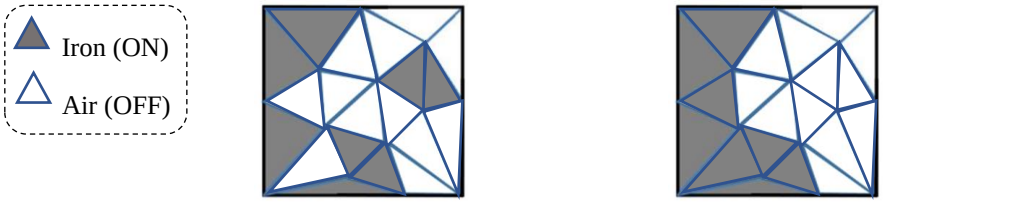

(a) Checkerboard structure (b) Processed by filtering algorithm

Figure 3-3: Checkerboard structure (a) checkerboard structure generated by stochastic algorithms, (a) checkerboard structure after filtering.

Figure 3-3(a) depicts a checkerboard structure. For ease of illustration, it is a local area containing only a dozen meshes. In fact, it should be the design region in Figure 3-1(b) containing 326 meshes.

To deal with the checkerboard structures, a specially designed filtering algorithm for the triangular cells proposed by *Watanabe* [22] is adopted, which checks and fixes the checkerboard structure throughout the whole TO process. As shown in Figure 3-4, the filtering algorithm includes a surface smoothing operator and a floating material removing operator.

The surface smoothing operator performs the following steps to fix the jagged material boundaries:

(1) Search and check the neighborhood of each element.

(2) If two or three sides of an element face toward another state, the state of this element will be converted.

(3) Back to Step 1 until no element can be converted.

The floating material removing operator works following the surface smoothing operator. For this model, the floating material removing operator is used to make sure the iron pole is a continuum by the following steps.

(1) Check the material connection status of each element.

(2) Calculate the area of each iron material block, list them up from large to small.

(3) Keep the biggest iron material block, convert the others to air.

(4) Back to Step 1 until only one iron block left.

3.3.3 Design of evolutionary operators

The evolutionary algorithms are well-used stochastic algorithms to search the optimal topology represented by the ON/OFF method. Since the aim of this work is to find the trade-off relationship between average torque and torque ripple, two Pareto-based MOEAs, NSGA-II, and SPEA-II, are used in this work.

Evolutionary algorithms basically use crossover and mutation to generate offspring. In order to apply NSGA-II and SPEA-II to the ON/OFF method-based TO, a set of Delaunay mesh-based evolutionary operators is designed for the modification of shape. As shown in Figure 3-5, the evolutionary operators including a crossover operator, a mutation operator, and a surface-mutation operator. The former plays a role in exploration, while the latter two play a role in exploitation.

The crossover operator creates offspring by differential evolution. It compares each element's state of two parental populations, then converts the elements that have different materials into air or iron randomly. This operator can make a lot of modifications to the shape while retaining the features of parental populations. The crossover operator can be formulated as:

$$\begin{cases} p_{offspring1} = p_{parent1} + [\alpha \times (p_{parent1} \oplus p_{parent2})] \\ p_{offspring2} = p_{parent2} - [\alpha \times (p_{parent1} \oplus p_{parent2})] \end{cases} \quad (5\text{-}2)$$

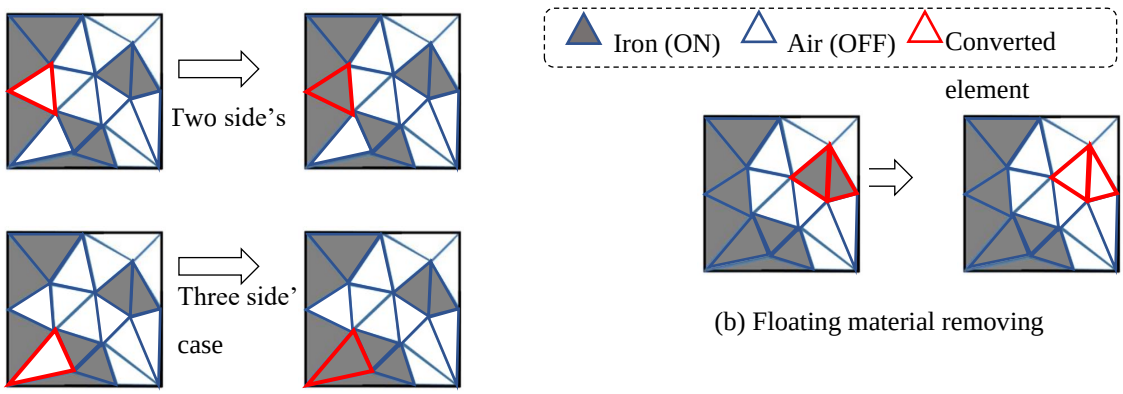

Figure 3-4: Filtering algorithm (a) Surface smoothing, (b) Floating material removing.

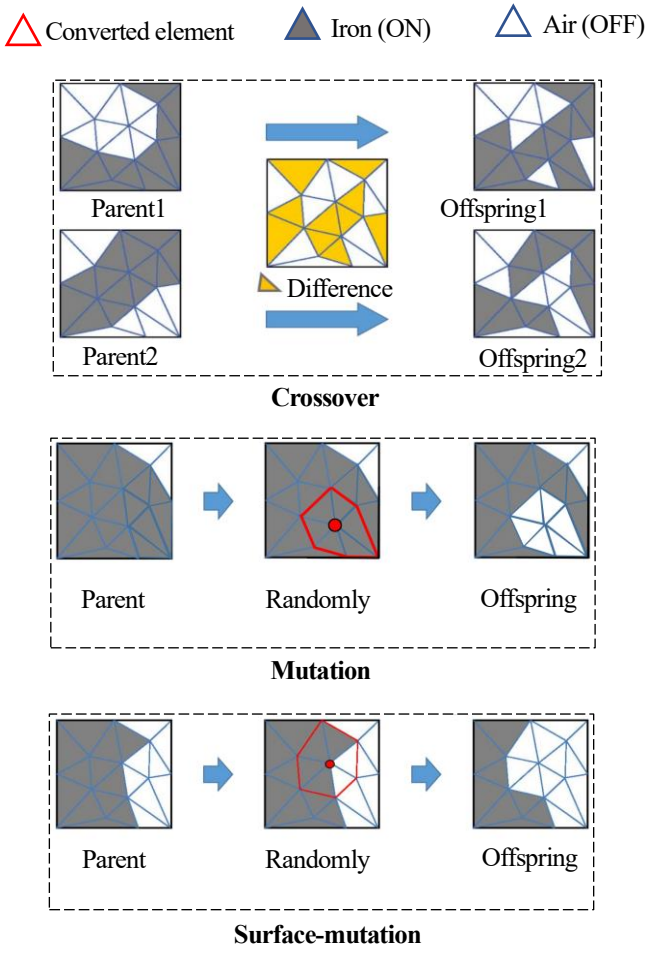

Figure 3-5: Crossover, mutation, and surface-mutation operator for multi-objective

evolutionary algorithms.

where p denotes the population. ⊕ is the "XOR" operator for comparing the binary-coded parental populations. α is the scaling factor of differential evolution. + and – indicate that the state of one element converts to "ON" or "OFF".

The mutation operator randomly chooses some nodes, then converts their surrounding elements' material into air or iron randomly. This operator can create holes inside the shape, which can be formulated as:

$$p_{offspring} = p_{parent} \pm (\beta \times N) \tag{5-3}$$

where β and N denote the probability of being selected for each node and surrounding element of the selected node.

The surface-mutation operator randomly chooses some nodes that belongs to the boundary of iron material, then converts theirs surrounding elements' material into air or iron randomly. This operator can make small modification on the shape boundary. The surface-mutation operator can be formulated as:

$$p_{offspring} = p_{parent} \pm (\gamma \times N_{surface}) \tag{5-4}$$

where γ and $N_{surface}$ denote the probability of being selected for each boundary node and surrounding element of the selected boundary node.

It should be noted that the mutation operator and surface-mutation operator are node-based modification in comparison with the crossover operator. This is because that node-based evolution is more efficient because it can avoid the conflict between evolutionary modification and the filtering algorithm.

3.3.4 Topology optimization workflow

An in-house FE calculation program, which can work in coupling with ON/OFF method and evolutionary algorithms, is used for TO. The working loop of the TO can be illustrated by Figure 3-6. The MOEAs create the offspring (topologies) by the evolutionary operators and

give corresponding material distribution to the FE calculation program, the FE program solve the non-linear magnetostatic field and feedback the torque performance of each offspring. Then the MOEAs perform Pareto solution sorting for this generation and create offspring by the evolutionary operators for the next generation. This looping continues until the given finish criterion is met.

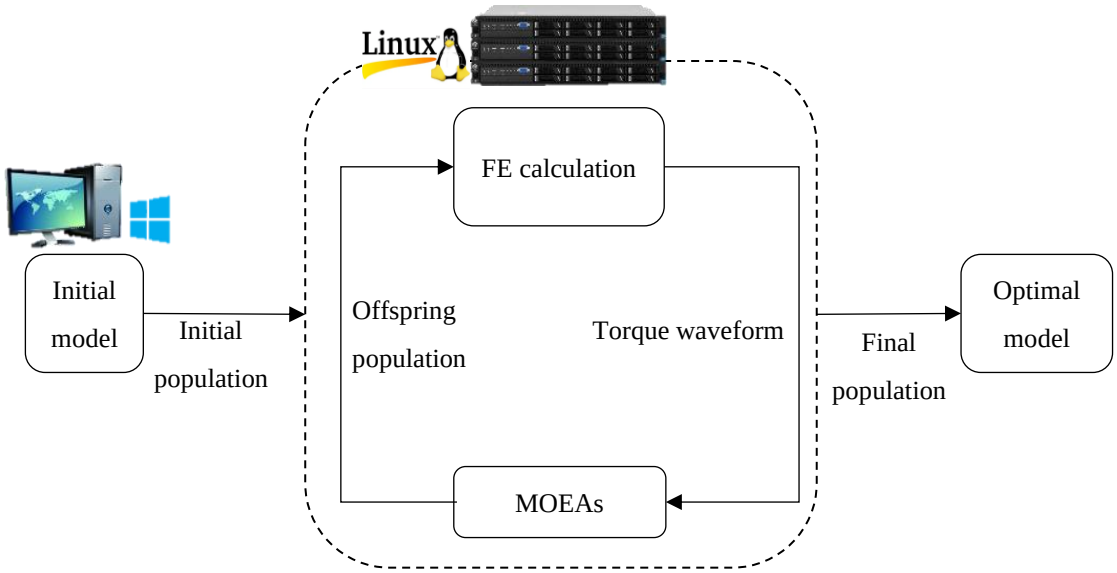

Figure 3-6: Working loop of topology optimization process.

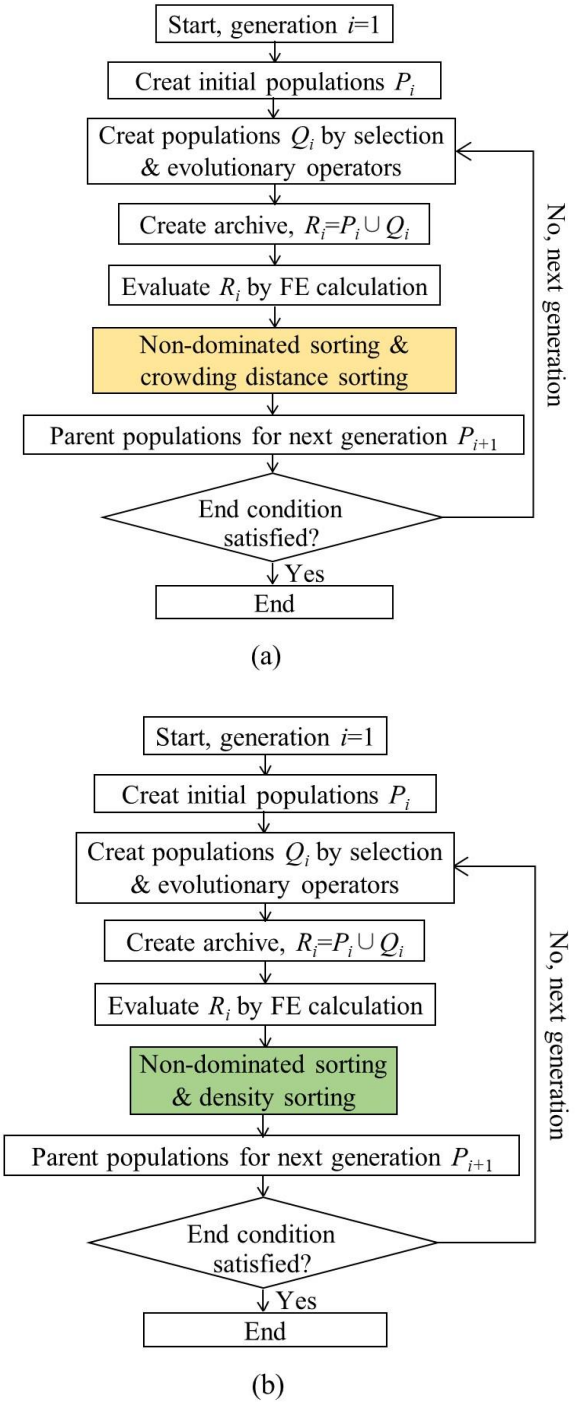

Figure 3-7: Flow diagram of NSGA-II and SPEA-II (a) NSGA-II, (b) SPEA-II.

3.4 Optimization results

3.4.1 Optimization problem formulation

As mentioned, the optimization aims to find out the trade-off relationship between average torque and torque ripple by recreating the topology of iron poles. Thus, two objective functions are defined as follows:

$$\begin{cases} max(T_{ave}) \\ min(T_{rip} = T_{max} - T_{min}) \end{cases} \tag{5-5}$$

where T_{ave},T_{rip}, T_{max}, and T_{min} are average torque, torque ripple, maximum torque, and minimum torque, respectively.

The torque is simulated where the condition that the rotor angle ranges from 0 to 45 degrees at 1-degree intervals. Nodal force method is used to calculate the force on the rotor.

3.4.2 Multi-objective optimization results

NSGA-II and SPEA-II with the aid of the proposed evolutionary operators are adopted to manage the design region. The flowcharts of the two MOEAs are depicted in Figure 3-7. Because NSGA-II and SPEA-II have different principles in Pareto solution sorting and archive length setting, for impartial comparison, the NSGA-II is performed twice with different population sizes (*P*). Then shape of initial populations are randomly generated. Evaluating 19200 topologies is set as stop criterion. Detailed settings of the algorithms can be found in Table 2.

The resultant Pareto fronts obtained by the algorithms are plotted in Figure 3-8(a), from which we can see that all the algorithms can find superior solutions compared with the original topology shown in Figure 3-1(a). The NSGA-II (*P*=24) finds the best Pareto fronts in comparison with the other two. The Pareto fronts searching results of NSGA-II (*P*=24) and NSGA-II (*P*=96) suggest that it may be more important to give each population more evolutionary opportunities than to adopt a large population size. This is consistent with a great deal of the previous work indicating that algorithms with stronger local search capability are

more suitable for TO of electromagnetic devices [23]-[25]. On the other hand, since NSGA-II (P=24) and SPEA-II (P=24) have the same population size and initial populations, it can be suggested that NSGA-II has stronger Pareto fronts searching ability for the formulated problem, while SPEA-II is better in terms of the distribution uniformity. A possible explanation for this might be that NSGA-II prefers to keep the local convex solutions in the Pareto solution sorting process, these kept outstanding populations may be helpful for the searching of Pareto fronts with a little sacrifice in distribution uniformity.

Three representative optimal iron poles are selected from the Pareto fronts. As shown in Figure 3-8(a), they are called Topology A, Topology B, and Topology C. The "No.FE" under their names means the number of finite element calculation trials required to generate the topology. The performance of the CP-PMSM with the selected optimal iron poles will be analyzed in the next section.

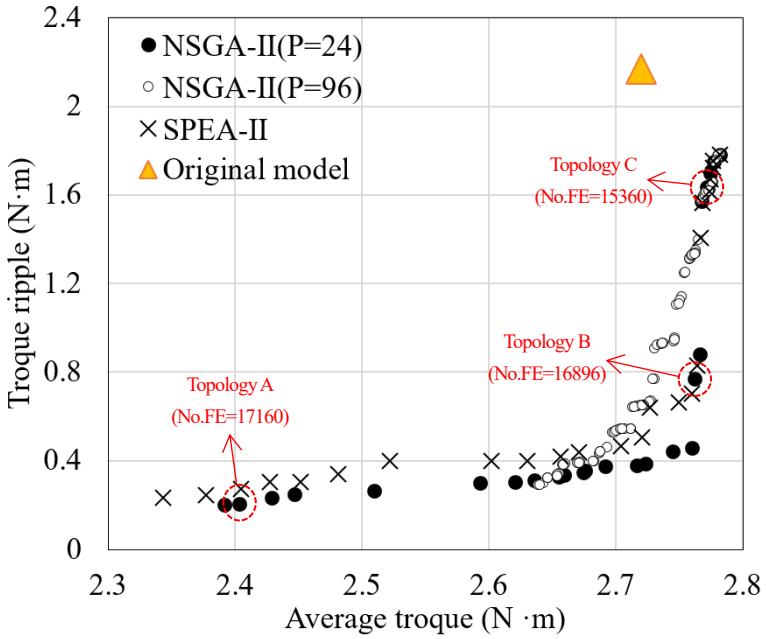

(a)

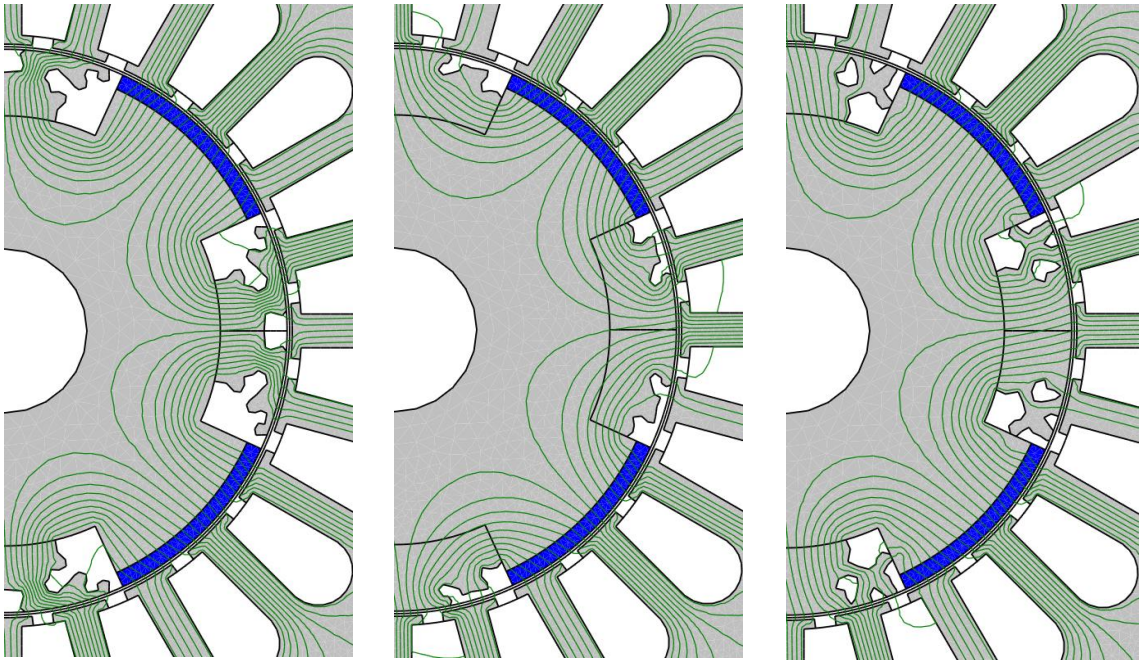

(b)

Figure 3-8: Resultant Pareto fronts and topologies (a) Resultant Pareto fronts obtained by three algorithms, (b) optimal topologies obtained by NSGA-II (P=24).

Table 3-2: Settings in NSGA-II and SPEA-II.

Items	*SPEA-II*	*NSGA-II*	*NSGA-II*
Size of population, P	*24*	*24*	*96*
Number of offspring population, Q	*96*	*24*	*96*
Length of archive, R	*24*	*24*	*96*
Total evaluation times (FE calculation)	*19200*	*19200*	*19200*
Generations	*200*	*800*	*200*
Probability of evolutionary operators (Crossover: Surface-mutation: Mutation)	*1:1:1*	*1:1:1*	*1:1:1*
Scaling factor, α	*0.5*	*0.5*	*0.5*

Selection probability for nodes, β	*0.1*	*0.1*	*0.1*
Selection probability for surface nodes, γ	*0.1*	*0.1*	*0.1*
Elapsed time	*21.4hours*	*23.8hours*	*24.6hours*

Intel Xeon Gold6134(8Core 3.7GHz), RAM usage: 300MB, Intel C++ Compiler

3.5 Discussion for the optimized motors

3.5.1 The role of modulator played by the iron pole

The winding function theory presented in [26] by *Lipo et al.* characterizes electric machines in terms of coupled magnetic circuits instead of accurate magnetic fields. Recently, a general airgap field modulation theory for electrical machines is proposed by *Cheng et al.* inspired by the derivation of the winding function concept [27-30]. This theory analysis of electrical machines by introducing the analogy between the electrical machine and the switching converter. According to this analogy, an electrical machine is a cascade of three elementary parts, that is, the primitive magnetizing magnetomotive force (source), the short-circuited reluctance/flux guide (modulator), and the armature winding (filter). The primitive magnetizing magnetomotive force (MMF) establishes an initial MMF. The short-circuited reluctance/flux guide modulates the initial MMF distribution to produce a spectrum of MMF harmonic components, for which they are termed as modulators. The armature winding plays the role of a spatial filter selecting effective airgap field harmonics, then receives the synchronous current to provide torque.

By introducing this airgap field modulation theory, the structure difference between the surface-mounted PMSM and CP-PMSM can be clearly explained. As shown in Figure 3-9, when we compare the rotor, for the surface-mounted PMSM, there are two sources made up of PMs, for the CP-PMSM, there is a source made up of PM and a modular made up of the salient iron pole. The salient iron pole modulates the influence of tooth harmonics, which in turn affects the airgap flux distribution. It can therefore be easily understood that the salient iron pole will

have different modulation effects in different topologies and result in different torque waveforms.

The magnetostatic field of Topology A, Topology B, and Topology C under no-load condition is solved. The airgap flux density of Topology A, Topology B, and Topology C, and the original machine is plotted in Figure 3-10, from which we can clearly observe how the optimized iron poles influent the tooth harmonic and modulate the flux in the airgap.

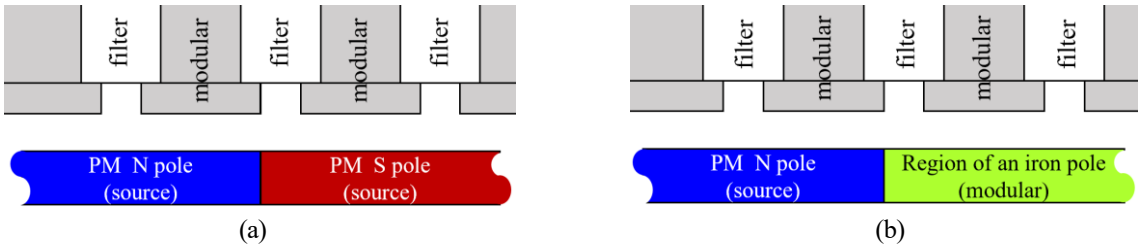

Figure 3-9: Models based on the airgap field modulation theory (a) surface-mounted PMSM, (b) CP-PMSM.

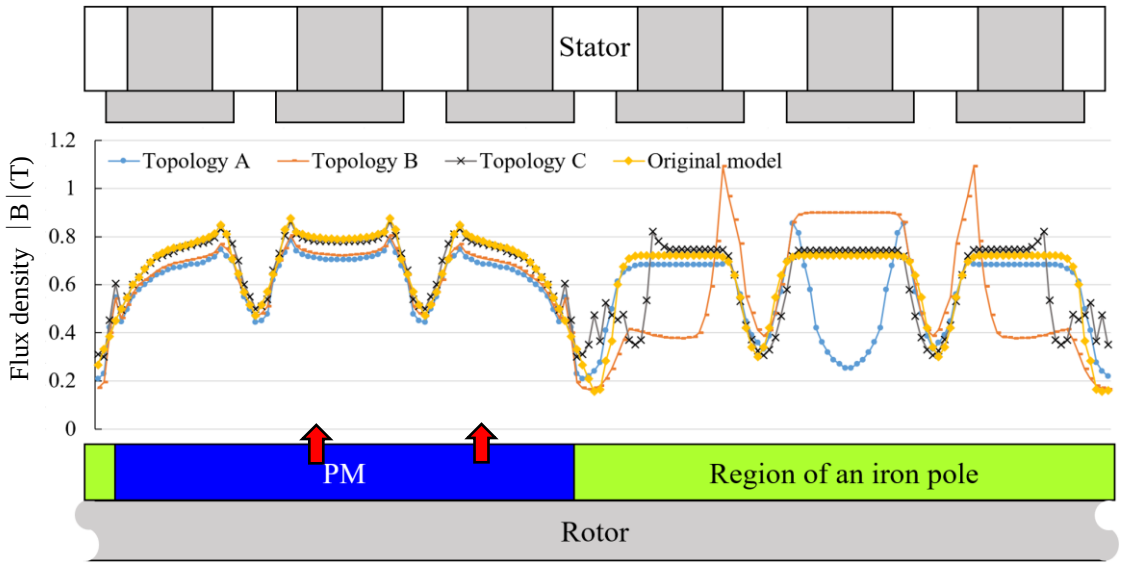

Figure 3-10: No-load airgap flux density of Topology A, Topology B, and Topology C, and the original machine (rotation angle: 0°).

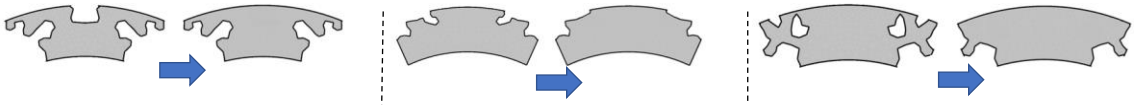

Topology A	Modified A	Topology B	Modified B	Topology C	Modified C
T_{ave}=2.40	T_{ave}=2.81(↑17%)	T_{ave}=2.73	T_{ave}=2.75(↑1%)	T_{ave}=2.77	T_{ave}=2.80(↑1%)
T_{rip}=0.21	T_{rip}=1.9(↑904%)	T_{rip}=0.77	T_{rip}=1.8(↑234%)	T_{rip}=1.64	T_{rip}=2.1(↑128%)

Figure 2-11: Optimized iron poles and the modified optimized iron poles(Unit: Nm).

3.5.2 Modulation effect of the optimized iron poles

As shown in Figure 3-11, to investigate the modulation effect of the optimized iron poles, the notch and holes in Topology A, Topology B, and Topology C are filled. The torque property of the CP-PMSM with the optimal iron poles and the modified optimal iron poles is simulated and summarized in Figure 3-11. For all three optimized topologies, the average torque is modestly improved after the modification, while the torque ripple is greatly deteriorated. The average torque is improved due to the decrease of equivalent air-gap length, while the deterioration of torque ripple may be due to the enhanced tooth harmonics. It can thus be suggested that the optimal iron poles with wavy shapes modulate the airgap flux to better distributions, consequently achieving better balance between the average torque and torque ripple.

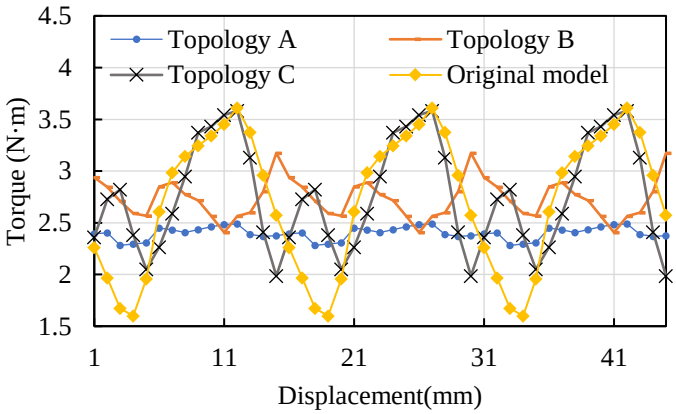

(a)

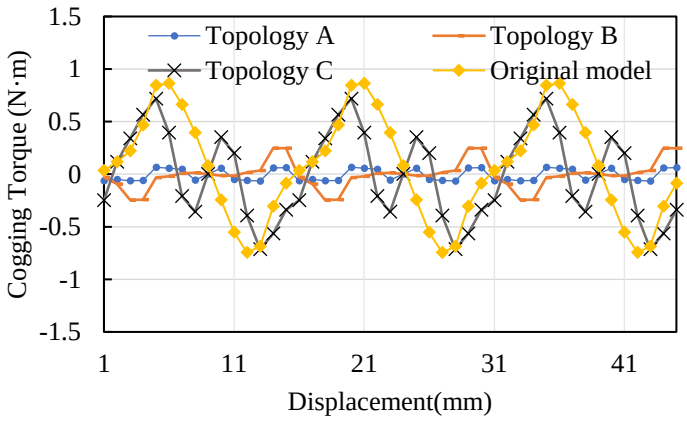

(b)

Figure 3-12: Performance of Topology A, Topology B, and Topology C, and the original machine (a) Torque waveform, (b) Cogging torque waveform.

Table 2-3: Performance comparison of optimized CP-PMSMs and original CP-PMSM.

Machines	*Average torque*		*Torque ripple*		*Cogging torque*		*Rotary inertia*
	Value (N·m)	*Variation*	*Value (N·m)*	*Variation*	*Value (N·m)*	*Variation*	*Variation*
Original model	*2.72*	*standard*	*2.18*	*standard*	*1.73*	*standard*	*standard*
Topology A	*2.40*	*↓11.8%*	*0.21*	*↓90.4%*	*0.13*	*↓92.5%*	*↓8.2%*
Topology B	*2.73*	*↑0.4%*	*0.77*	*↓64.7%*	*0.49*	*↓71.7%*	*↓2.6%*
Topology C	*2.77*	*↑1.8%*	*1.64*	*↓24.8%*	*1.44*	*↓16.8%*	*↓4.2%*

3.5.3 Analysis of the torque characteristics

The torque waveforms and cogging torque waveforms of Topology A, Topology B, and Topology C are plotted in Figure 3-12. A comprehensive comparison is given in Table 3. Comparison results indicate that the torque properties, especially cogging torque, are surprisingly improved. It can be suggested that the multi-tooth structures modulate the airgap flux, suppress the cogging torque, and contribute a lot to the resultant low torque ripple. Meanwhile, the rotary inertia of optimized CP-PMSMs is lower than that of the original CP-PMSM, which has a benefit on the dynamic response characteristic.

3.6 Conclusions

This study has studied the multi-objective TO on a CP-PMSM to unlock the full design space potential. To this end, the evolutionary operators, which can make modifications to the shapes under Delaunay meshes, are proposed and formulated. Thereby we demonstrated how to combine the ON/OFF method with MOEAs and how to apply this technique efficiently for the TO of this machine. The aiming of finding the trade-off relationship between the average torque and torque ripple has been completely fulfilled. In addition, it is numerically shown that the NSGA-II can find superior solutions in comparison with SPEA-II for the formulated problem.

4. Study on topology optimization for permanent magnet linear synchronous machines

4.1 Permanent magnet linear synchronous machines

Permanent magnet linear synchronous machines (PMLSMs) are types of equipment with simple structure and easy maintenance, they can efficiently convert energy between linear motion mechanical energy and electrical energy. PMLSMs have been used in many applications since the distinct merit of direct energy conversion without intermediate translation mechanisms. A typical application of PMLSMs as generators is the wave energy conversion system [31,32]. Typical applications of PMLSMs as motors are linear metros and reciprocating servo systems [33,34]. However, the detent force (DF), which makes the mover and stator tend to align in certain positions, is an inherent problem of PMLSMs [35]. The DF is caused by the periodic fluctuation of mutual attraction between permanent magnets (PMs) and the mover core with positions, it exists even in no-load case and deteriorates the performance of PMLSMs. When PMLSMs are used as the generator, the DF will hinder the movement of the mover or make its velocity oscillate, affecting the electric power generation and electric power quality. On the other side, when PMLSMs are used as the motor, the DF will induce mover velocity oscillation thus deteriorates positioning accuracy.

In the past several years, the suppression of DF had become the most active field in PMLSM research [36]-[45]. Albeit control strategies can be used to alleviate the DF [36,37], most of the published works aim to reduce the DF by special designs in the initial design phase [38]-[45]. As depicted in the flux lines in Figure 4-1, the distorted flux distribution caused by the mover core ends is the cause of DF. To reduce the DF, some methods have been proposed. The most effective one is to optimize the mover core length, this technique can be considered a kind of passive compensation method as it adjusts the phase difference between the left- and right-end forces by adopting a proper mover core length [38,39]. Other active compensation methods are also proposed, such as adding auxiliary teeth [40,41] or compensation winding [42,43]. In these

methods, a part that can produce a force wave opposite to the fundamental component of DF is connected to the mover core to suppress the periodic DF. In addition, for applications with adequate mounting space, some special arrangement methods such as staggered double-side mover or multi-unit combinations are also effective [44,45], the principle is to compensate the overall DF through the phase difference of DF between different primary units. Actually, compensation methods for DF cannot completely eliminate the DF due to the DFs are not ideally sinusoidal and have many high-order harmonics.

Although many achievements have been made on DF reduction of PMLSMs, all of them regarded DF as an inevitable phenomenon caused by the finite mover core and suppress the DF in a compensation way. In fact, based on the theory of the virtual work method, the generation mechanism of the DF is because of the fluctuations of magnetic energy stored in the air gap with different moving positions [35]. Therefore, if the shape of the mover core is designed ideal enough to make the magnetic energy stored in the air gap change little with the mover position, the ripple of DF can be eliminated to nearly zero.

In this study, a design methodology for minimizing the DF on PMLSMs is proposed. The proposed methodology allows for discovering the ideal mover shape, which can eliminate the DF to nearly zero. Specifically, a mesh-level ON/OFF method is introduced to manage the topology of the two mover ends for producing auxiliary ends, evolutionary algorithms are adopted to steer the shaping. It will be shown by comprehensive numerical results that the proposed design methodology is viable and effective, the DFs and thrust ripple of two typical PMLSMs can be minimized to a considerably low level.

4.2 PMLSMs modeling and analytic model of detent force

This section firstly explains the PMLSMs modeling by finite element method (FEM). Then,

the reason for adopting inverse mover ends shaping for DF minimization is explained in an analytic way.

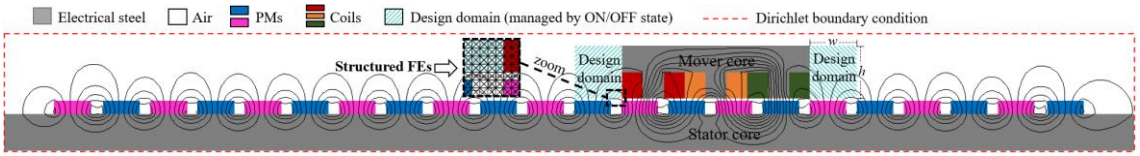

Fig. 4-1. Modeling of the 3-slot 4-pole PMLSM by finite element method and the calculated flux distribution on no-load condition.

4.2.1 Modeling PMLSMs by finite element method

The PMLSMs modeling is accomplished by the FEM as it can consider shape details and achieve high precision in the calculation of the performance parameters. For the earlier design steps of PMLSMs, 2D field models are typically used to calculate the major machine parameters up to an accuracy that is sufficient in practice. For coupling the ON/OFF method, the structured finite elements (FEs) are adopted. Figure 4-1 depicts the 2-D FE modeling for a 3-slot 4-pole PMLSM that will be studied. Every four FEs can be pieced together to form a square required by the ON/OFF method. To calculate the DF of the PMLSM, one has to solve Maxwell's equations. The magnetostatic formulation is sufficient to model the PMLSM. This implies that eddy currents and displacement currents are neglected. To calculate the magnetic vector potential A, one has to solve the partial differential equation

$$\nabla \times (v\nabla \times A) = J - \nabla \times H \tag{4-1}$$

with proper boundary conditions. v means the reluctivity, J and H depict the source current density and PM's source magnetic field strength, respectively. The nonlinear permeability of the electrical steel is modeled by JIS50A350. For freely shaping the mover ends, the modeling and solving of PMLSMs are performed by an in-house FEM program written by the authors. The node force method is used to calculate the force on the mover core. It takes about 5-7

seconds to calculate the DF profile of a PMLSM by the CPU Intel Xeon Gold 6134 when the Incomplete Cholesky decomposition conjugate gradient is used as the solver.

Once the finite element model for one PMLSM is established, the finite element model for other PMLSMs can be easily created by updating the node connectivity and mesh material information, in another word, the in-house FEM program for PMLSM analysis is general. To verify the correctness of DF calculated by the in-house FEM program, the DF of a PMLSM is calculated by the in-house FEM program and compared with the experimental data. Specifications of the PMLSM and experiment bench can be found in [46]. As shown in Figure 4-2(b), the DF provided by the in-house FEM has good agreement with the experimental data. The DF fluctuates with the period of a pole pitch.

It should be noted that the PMLSM prototype that provides experimental data is not the PMLSM numerical example studied in this paper, it is from a prototype tested by our group before. The authors deem that this experimental approach is enough to verify the correctness of the numerical analysis for the typical PMLSMs studied in this paper, as the in-house FEM program for PMLSM analysis is general.

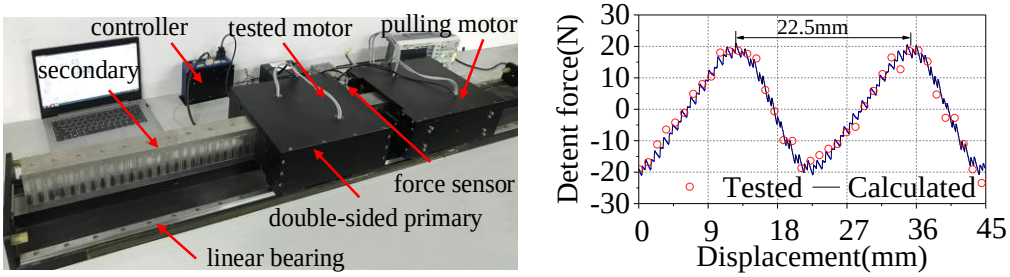

(a) (b)

Fig. 4-2. (a) experiment bench and prototype; (b) comparison of detent force provided by in-house FEM program and experimental data.

4.2.2. Analytic model of Detent force on typical PMLSMs

Theoretically, for PMLSMs, when the slot effect in the mover core is neglected the magnetic force at the left- and right-end can be expressed in the form of Fourier series [9]. Therefore, DF of the mover core is:

$$F_{detent} = F_{detent\_left} + F_{detent\_right} = \sum_{n=1}^{\infty} F_n \cos\left(\frac{\delta}{2}\right) \sin\left(\frac{2n\pi}{\tau}x + \delta\right) \quad (4\text{-}2)$$

Equation 2 shows that DF should be zero if the length of the mover core δ is taken as

$$\delta = (2k-1)\pi \quad (4\text{-}3)$$

where k is an any integer. However, the magnetic length of the stator is different from the real geometric length. Meanwhile, the end forces are actually not ideally sinusoidal, when the slot effect is further considered, the spectrum will be more abundant. As a result, it is difficult to minimize the DF in a forward way by theoretically predicting the optimal mover core length and shape. Nevertheless, based on the concept that the spectrums and respective phases in DF are determined by the shape and length of the mover core, respectively. It can be suggested that one or some ideal mover structures should exist, and their DFs are infinitude adjacence zero.

To find out the ideal structures, an inverse way is adopted, and the topology of the mover ends will be shaped in a stochastic way for minimizing the ripple of DF. As shown in Figure 4-1, the design domains for TO are rectangles with height h and width w on two mover ends. Since the design domains basically do not influence the energy conversion in the airgap under windings but modulate the flux distribution around the mover ends, it can be expected the optimized mover ends shape can influent the waveform of DF while not influent the energy conversion capacity of PMLSMs. The next section moves on to elaborate on the mesh-level shaping methodology.

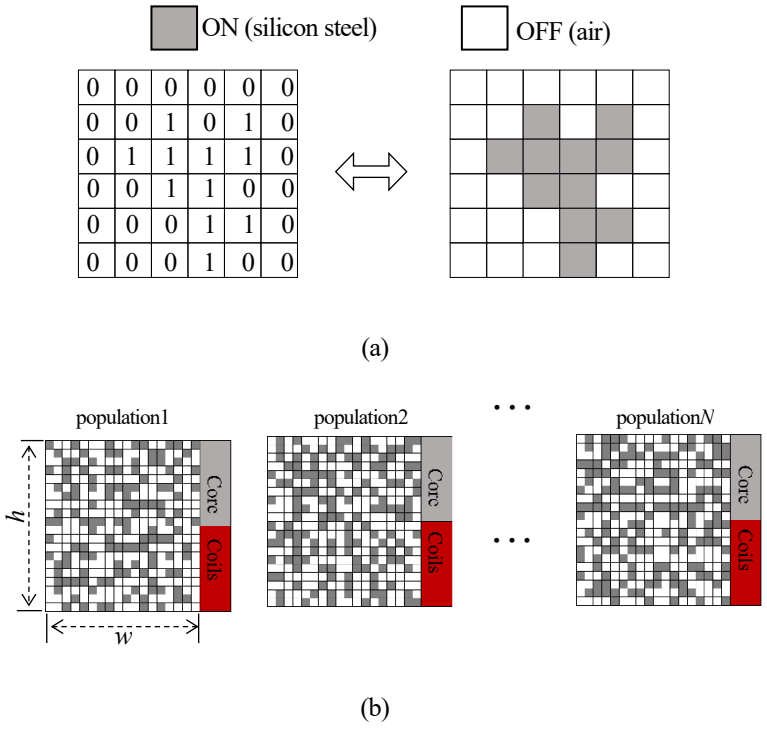

Fig. 4-3. (a) ON/OFF method for topology expression; (b) some initial populations with random pattern (initialization stage).

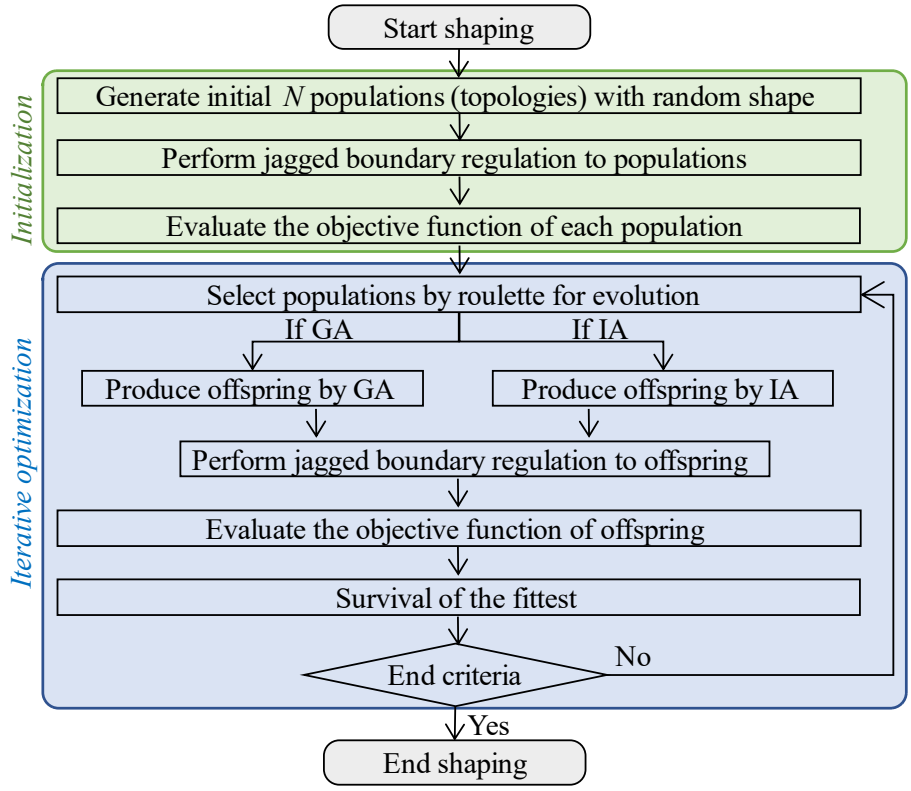

Fig. 4-4. Simplified flow for shaping the mover ends by the ON/OFF method and evolutionary algorithms.

4.3 Inverse shaping method

In this section, we present an introduction on how the ON/OFF method couples with a evolutionary algorithm for the mesh-level inverse shaping. Specifically, the topology expression method, the topology reproduction method and the jagged boundary regulation method are elaborated in turn.

4.3.1. Topology expressed by ON/OFF method

Topology optimization (TO) is a state-of-art technique for inverse shaping [47,48,24], contrary to treating forward problems ("Given the structure, find the property") the TO pursues a new paradigm ("Given the desired property, find the structure"). The broad category of TO techniques can be generally classified by gradient-based methods such as density method and level-set method, and stochastic-based methods such as ON/OFF method [48,24]. The ON/OFF method is adopted for shaping of mover ends since it is well suited for noisy, multi-modal, discontinuous black-box optimization problems such as the TO of electromagnetic devices.

For the implementation of the ON/OFF method, the optimization domain is discretized into numerous cells. As shown in Figure 4-3(a), the material in each cell is considered an independent design variable that can take up either "ON" (electrical steel) or "OFF" (air) material, the optimal topology is obtained by trialing a great variety of ON/OFF binary combinations. As the inverse shaping flow shown in Figure 4-4, the trials are usually steered by an evolutionary algorithm (EA) for a better searching efficiency. In this study, "ON" (electrical steel) and "OFF" (air) are used to shape the mover ends on PMLSMs for achieving the desired DF, genetic algorithm (GA) and immune algorithm (IA) are used to steer the shaping.

The initial populations (topologies) for producing mover ends are randomly created for the diversity of the populations. Some of the initial populations are drawn in Figure 4-3(b).

4.3.2. Genetic algorithm for topology reproduction

For the reproduction of topologies, an algorithm is necessary. GA is the most typical metaheuristic algorithm, it mainly produces offspring by crossover. The basic concept of crossover for TO is depicted in Figure 4-5, the crossover based on differential evolution and produces new topologies by converting the state of some cells that have different states in the two parental topologies.

The detailed procedures of ON/OFF method steered binary GA can be summarized as the following steps.

(1)Generate initial *N* populations (topologies) by assigning the ON/OFF state of each cell randomly.

(2)Perform filtering to initial topologies.

(3)Randomly select two topologies as parents, then produce two offspring by crossover.

(4)Perform filtering to offspring.

(5)If the offspring has higher objective function value, it will take place of its parent.

(6)Back to step 3.

The convergence speed of searching can be controlled by adjusting the scaling factor in the crossover.

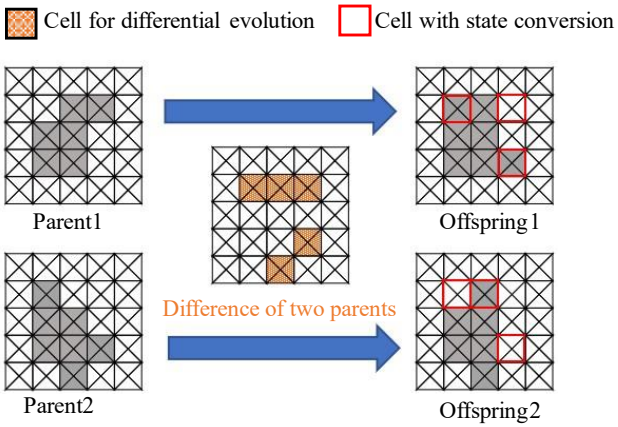

Fig. 4-5. Topological evolution by ON/OFF method and GA (iterative optimization stage).

4.3.3 Immune algorithm for topology reproduction

The IA for TO is inspired by the clonal selection principle in the mammalian immune system. The basic concept of IA is shown in in Figure 4-6, it creates new typologies by affinity maturation, which produce offspring topologies by make small modifications to the surface of a parental topology. Compared with the crossover in GA, affinity maturation in IA is an exploitation-based operator since the material modification only happens on the shape surface. The detailed procedures of ON/OFF method steered by IA can be summarized as the following steps.

(1)Generate initial *N* populations (topologies) by assigning the ON/OFF state of each cell randomly.

(2)Perform filtering to topologies.

(3)Evaluate the objective function value of each topology, list them up from high value to low, and then weed out *W* topologies with low objective function.

(4)Generate clones for each topology. Topologies with high objective function will be cloned more times for creating more offspring in next step.

(5)Perform affinity maturation for clones to crate offspring.

(6)Perform filtering to each offspring.

(7)If the best offspring has higher objective function, it will take place of its parent.

(8)Add randomly generated topology to keep the population size *N* constant.

(9)Back to step 3.

Steps 4-6 play a role of local search, while step 8 plays a role of global search. We can control the balance of local and global search by adjusting the parameters *W*.

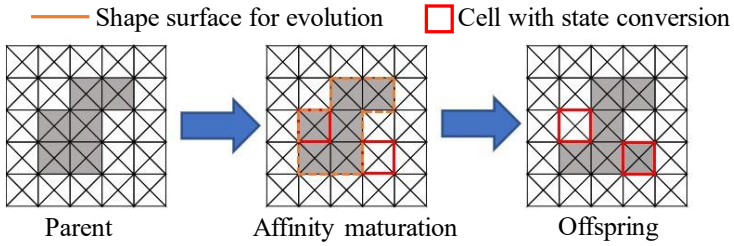

Fig. 4-6. Topological evolution by ON/OFF method and IA (iterative optimization stage).

4.3.4 Jagged boundary regulation by half material filling

The topologies with terraced boundaries may be too expensive from the manufacturability point of view. To evolve out topologies with no terraced surface, a post-process method based on half-material filling is proposed. Depicted as the resultant topologies in Figure 4-7, this post-process fills the terraced boundaries with triangular half-material for smoother boundaries. To avoid the conflict between the boundary regulation and topological evolution, the half-material cells are considered void in the GA and IA.

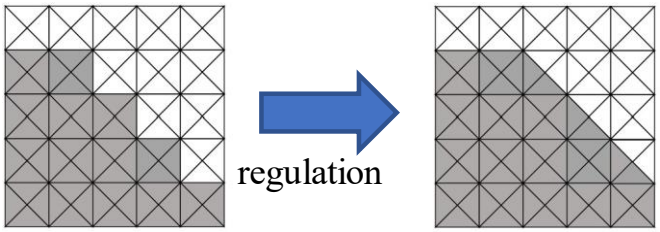

Fig. 4-7. Jagged boundary regulation by triangular material filling (iterative optimization

stage).

4.4 Shaping results

4.4.1 Typical PMLSMs studied

Table 4-1. Specifications of two typical PMLSMs studied as the numerical examples.

Item		3-slot 4-pole PMLSM	6-slot 7-pole PMLSM
Rated Current density in Windings		BLAC 5A/mm^2	BLAC 2A/mm^2
Air-gap length		1mm	2mm
Grade of electrical steel		JIS 50A350	
Mover	Mover yoke height	10mm	
	Slot pitch	24mm	
	Slot width	8mm	
	Slot height	10mm	
	Coils (per teeth)	40 turns	
	Lamination	100mm	
Stator	Stator yoke height	14mm	
	PM width	14mm	
	PM height	5mm	
	PM grade	Nd-Fe-B N46H	
	Pole pitch (τ)	18mm	

Table 4-2. Setting in topology optimization.

Item	GA	IA
Population size N in each generation	100	20
Scaling factor	0.2	/
Proportion of weed out W	/	30%
Modified surface cells in affinity maturation	/	10%

Two typical fractional slot PMLSMs respective adopting 3-slot 4-pole (3s4p) structure and 6-slot 7-pole (6s7p) structure are chosen as numerical examples. The two PMLSMs are designed as motors for the application where low speed and high thrust are needed. Besides the

slot pole combination, the differences between the two numerical examples are the air gap length and rated current density, which aims to clarify the effectiveness of the proposed DF minimization methodology on PMLSMs with different magnetic saturation levels. Specifications of the two PMLSMs can be found in Table 1. The DF and thrust waveforms of the two PMLSMs before optimization can be found in Figure 4-13, from which we can clearly observe that the DF deteriorates the smoothness of thrust.

4.4.2 Shaping settings

As shown in Figure 4-1, the TO domains are rectangles with height h and width w on the mover ends, which was originally air. The w is set as τ, which equals the wavelength of DF, while h is set as the height of the mover core. Every four triangular FEs in these domains serve as a rectangular cell in the ON/OFF method, "ON" (core) and "OFF" (air) are used to represent the topology. Thus, the design variables are binary states in 360 ($w \times h = 360$) cells. The created shapes in the left TO domain will be mirrored to the right TO domain to keep the mover symmetry.

The objective function is defined as:

$$\text{objective function} = \text{minimize}\ (DF_{rip}) \tag{4}$$

where DF_{rip} denotes the ripple (peak-peak value) of detent force in the moving direction.

4.4.3 Shaping results

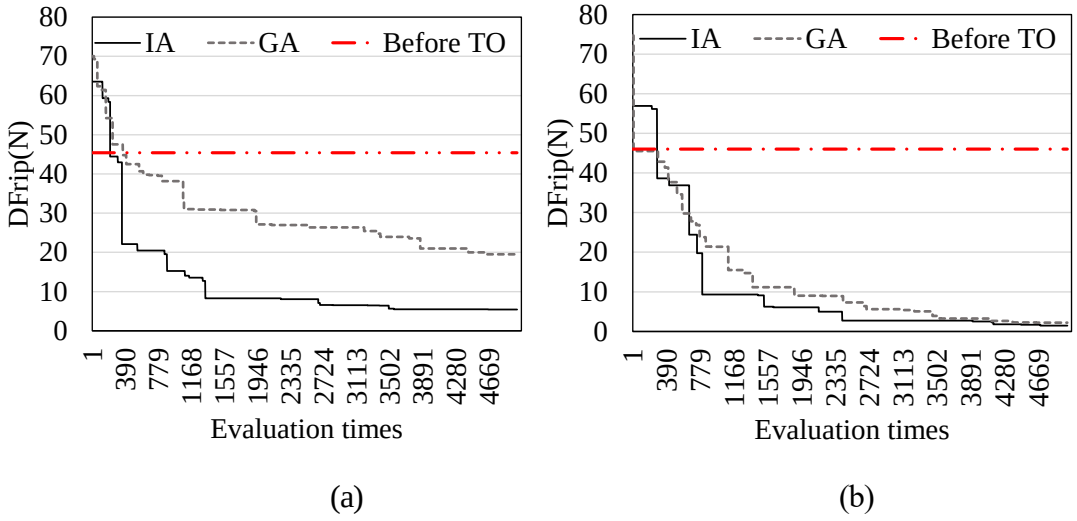

Fig. 4-8. Convergence history of GA and IA for DF minimization (a) 3-slot 4-pole PMLSM; (b) 6-slot 7-pole PMLSM.

Table 4-3. Detent force and average thrust of PMLSMs before and after optimization.

PMLSM	Average thrust (N)			Detent force ripple (N)		
	Original	After TO		Original	After TO	
		GA	IA		GA	IA
3-slot 4-pole	107.4	108.5	108.1	45.4	19.3	5.2
6-slot 7-pole	58.4	59.1	59.2	46	2.1	1.8

The convergence history of IA and GA is depicted in Figure 4-8. We can observe from Figure 4-8 both GA and IA have converged after 5000 different designs are evaluated, the corresponding elapsed time is about 10 hours. The data in Figure 4-8 suggests that both GA and IA have the ability to produce an end shape that can suppress the thrust ripple of PMLSMs to a considerably low level. The DF cannot be totally eliminated but can be suppressed to nearly zero, which must be caused because the limited number of meshes limits the shape representation. With a finer mesh, the DF minimization effect can be further improved, which

will also induces a longer computational time.

In comparison with GA, IA is better in terms of efficiency for the formulated black-box optimization problem. As for the optimal mover core structure, GA and IA provided different results since the stochastic shaping. Figure 4-9 shows the optimized ends provided by GA and IA. The DF ripple of the optimized 3s4p- and 6s7p-PMLSM can be 5.2N and 1.8N, which are suppressed by 89% and 96%, respectively. For both PMLSMs, the DF is suppressed to a considerably low level. Thanks to the suppressed DF, the thrust waveforms of two PMLSMs are also optimized. For the 3-slot 4-pole PMLSM, the thrust ripple after TO is 6.1N, which is 13.4% of the original value. For the 6-slot 7-pole PMLSM, the thrust ripple after TO is 1.8N, which is only 3.9% of the original value. In addition, the average thrust is basically unchanged, which is in line with our expectations as the mover ends basically do not participate in energy conversion. The waveforms of DF and thrust before and after optimization can be found in Figure 4-13.

The optimal design provided by a metaheuristic algorithm depends on random number extractions. Numerical experiment on the optimization results under different initial seeds is also conducted. The results show that when the initial seeds (topologies) change, the convergence characteristics of the GA and IA are similar. Specifically, the convergence speed of the GA and IA with different initial seeds is close, and the resulting objective function with different initial seeds is also close. However, it is worth noting that although the convergence characteristics with different seeds are close, the shape of the optimal topology may be quite different. This phenomenon is caused by the multimodal landscape of the electromagnetic TO problem [47][49], that is, there can be a considerable number of optimal solutions, whose topologies are rather different, but the objective function (DF in this paper) is very close.

The results in this section indicate that the proposed design methodology can minimize the

DF on typical PMLSMs to a considerably low level. Thanks to the suppressed DF, the optimized PMLSMs can provide smoother thrust when it is used as the motor or capture smaller mechanical energy when it is used as a generator. The next section, moves on to figure out how the optimized mover ends influent the PMLSMs for achieving DF suppression.

4.5 Performance investigation for the optimized PMLSMs

In this section, the mechanism of the optimized ends acting on PMLSMs is investigated. The PMLSMs with the IA-produced optimal ends are comprehensively investigated by the in-house FEM program. The flux distribution of the optimized 3s4p PMLSM in the no-load case is shown in Figure 4-10, the flux around the mover ends is guided by the optimized auxiliary ends. To clarify the DF minimization mechanism provided by the optimal ends, the force in the moving direction in the whole mover is abstracted into three parts by node force method. The three parts are the force in the left auxiliary end F_{left}, the force in the original mover core F_{middle}, force in the right auxiliary end F_{right}.

Firstly, the contribution of auxiliary ends and original mover core to the detent force under no-load condition is analyzed. As shown in Figure 4-11, due to the symmetrical structure, the waveforms of detent force provided by the two auxiliary ends are the same, but their directions are opposite, and the phases differ by half a cycle. Due to the force provided by the auxiliary ends, the total DF is significantly suppressed. For the 3s4p and 6s7p PMLSM, the overall detent force is suppressed by 89% and 96%, respectively.

Then, the contribution of auxiliary ends and the original mover core to the thrust under rated conditions is analyzed. As shown in Figure 4-12, the force waveforms provided by the auxiliary ends is almost the same as the no-load case, indicating the exciting current basically does not affect the force characteristics of the auxiliary ends. In addition, the average torque provided by

the auxiliary ends is zero, confirming that the auxiliary ends do not participate in energy conversion.

The DF and thrust of the original PMSLMs and the optimized PMLSMs are depicted in Figure 4-13, from which we can clearly see that the optimized PMLSMs can provide smooth thrust because the ripple of the DF is suppressed. Thrust performance with different current densities is shown in Figure 4-14, the results confirm that the PMLSMs with the optimized ends can provide smoother thrust in all operation modes thanks to the considerably low DF.

The nonlinear magneto-static formulation in the in-house FEM program is based on the assumption that there is no deformation or vibration of the mover ends. In fact, PMLSMs are often used where high dynamic linear motion is required. Therefore, it is important to ensure that the acceleration-induced mechanical properties have no impact on electromagnetic performance. The mechanical properties of the 3s4p PMLSMs with the IA-provided optimal ends at an acceleration of 20 m/s^2 are simulated. The maximum Von-Mises stress on the mover core is 661kPa, which is far lower than the yield strength of silicon steel. Thus, it can be considered that the optimal designs produced by the proposed methodology can fully meet the structural strength requirements.

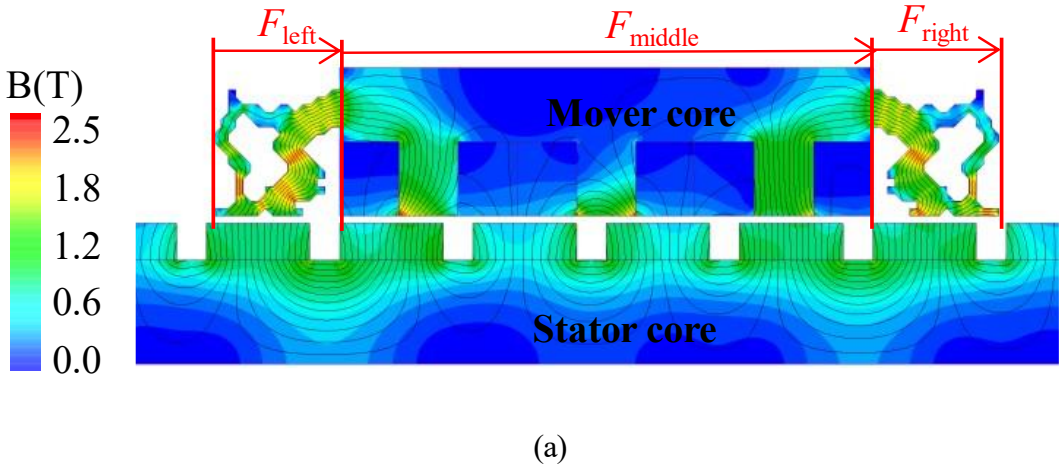

(a)

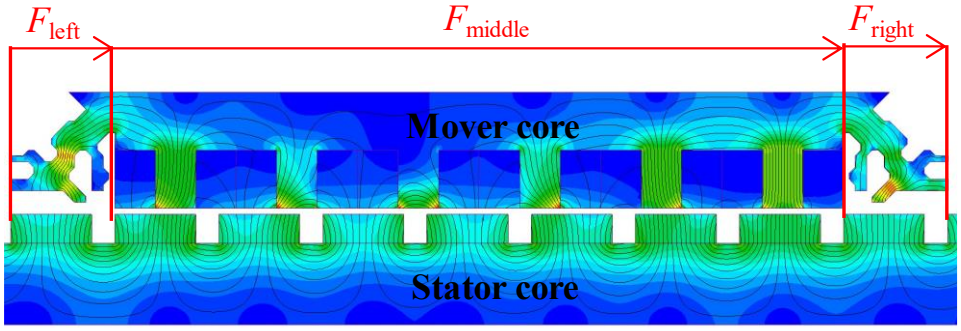

(b)

Fig. 4-10. Flux lines and flux density of the PMLSMs with IA-produced optimal mover ends (a) 3-slot 4-pole PMLSM; (b) 6-slot 7-pole PMLSM.

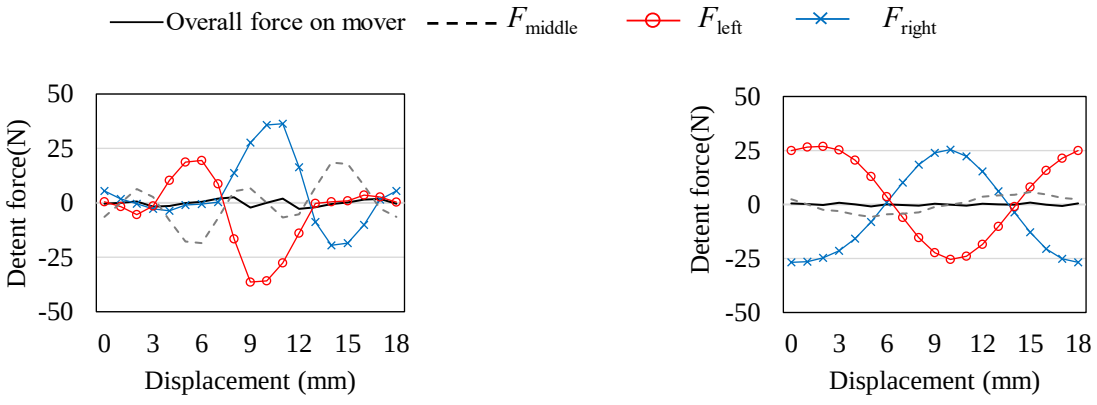

(a) (b)

Fig. 4-11. Detent force in one period of the PMLSMs with IA-shaped mover ends (a) 3-slot 4-pole PMLSM; (b) 6-slot 7-pole PMLSM.

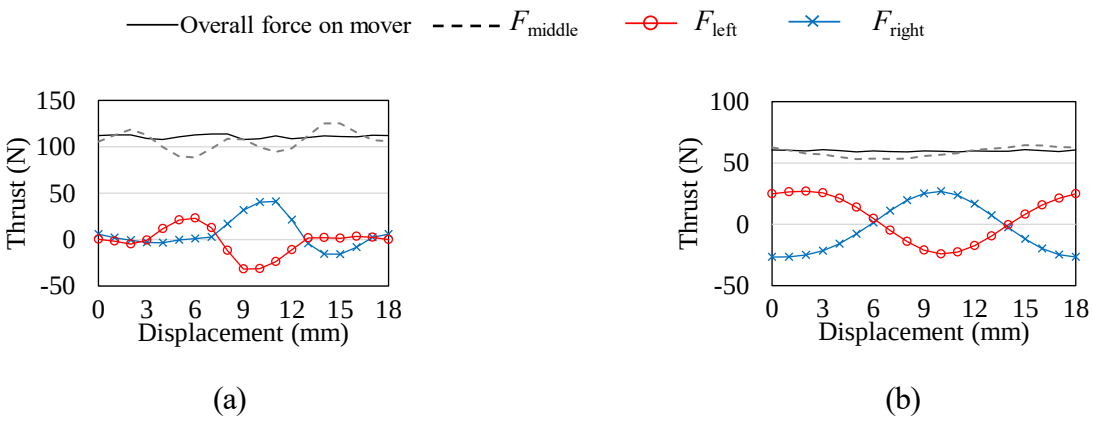

Fig. 4-12. Thrust in one period of the PMLSMs with IA-shaped mover ends (a) 3-slot 4-pole PMLSM; (b) 6-slot 7-pole PMLSM.

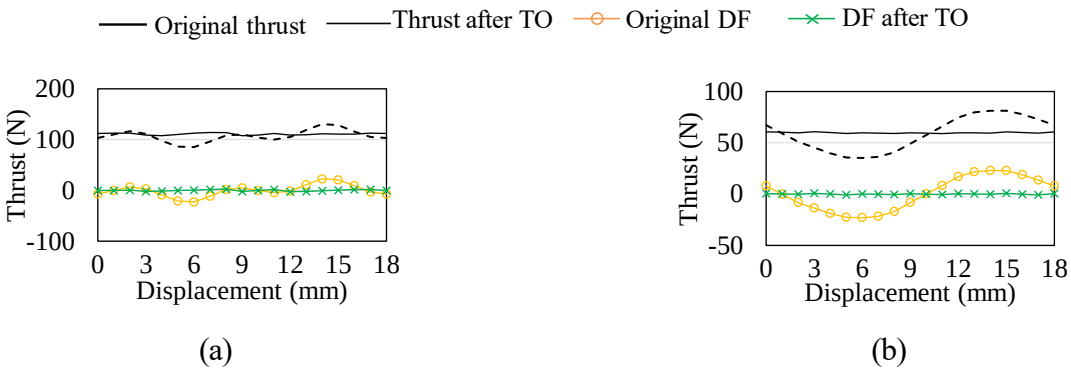

Fig. 4-13. Thrust and DF of the original PMLSMs and PMLSMs with IA-shaped mover ends (a) 3-slot 4-pole PMLSM; (b) 6-slot 7-pole PMLSM.

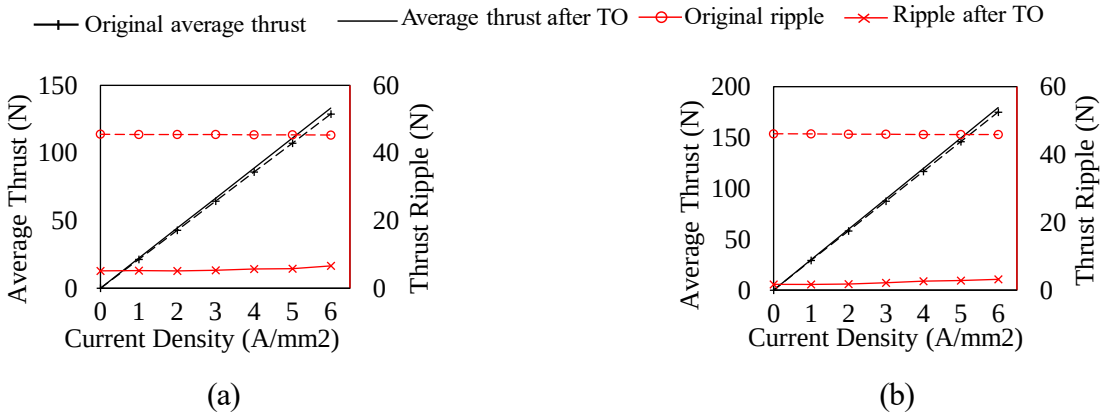

Fig. 4-14. Thrust with current density of the PMLSMs before and after optimization ($i_d = 0$). (a) 3-slot 4-pole PMLSM; (b) 6-slot 7-pole PMLSM.

4.6 Conclusions

A mesh-level design method to shape the mover ends of PMLSMs is proposed. The proposed method allows for discovering the ideal mover shape, which can eliminate the DF to nearly zero. Numerical results demonstrated the proposed methodology is effective for different PMLSMs. The detent force of two typical PMLSMs is suppressed by 89% and 96% without influencing their average output thrust. With a finer mesh, the detent force minimization effect can be further improved. The comprehensive numerical results indicating the proposed detent force minimization methodology is viable and applicable, offering a novel approach to the design of PMLSMs.

5 Topology optimization of SRM for reducing vibration

5.1 The vibration problem in switched reluctance motors

The switched reluctance motors (SRMs) have many advantages over other electric motor types, such simple construction, low cost, wide speed range, and reliability. However, compared with other electric motors, such as permanent magnet synchronous motors and induction motors, the vibration and acoustic noise of SRMs are more severe. The further promotion of SRMs in many applications is thus limited [50]-[52]. Thus, designing SRMs considering vibration and acoustic noise properties but not only torque properties at the early design stage can be substantially beneficial.

The vibration and acoustic noise in SRMs can arise from electromagnetic, mechanical, or aerodynamic causes. The electromagnetic vibration and noise, which are caused by the pulsating electromagnetic forces (EMFs) in the airgap, contribute to the majority of vibration and acoustic noise in SRMs [50]-[52]. During the electromechanical energy conversion, EMFs (mainly radial components) excitations in the airgap are amplified by the natural modes of the stator structure and induce stator vibrations. The vibrations on stator surface transmit sound waves through the surrounding air medium. The sound waves are sensed by the human eardrum. When the stator structure is excited periodically, resonances may occur when the excitation frequencies coincide with mode frequency (natural frequency) of the stator. The resonances cause severe vibration and acoustic noise and may make people uncomfortable. The electromagnetic vibration of an SRM can be precisely predicted by numerical methods such as the finite element method (FEM) [53].

Over the past two decades, many studies have been conducted to mitigate the electromagnetic vibration and acoustic noise of SRMs [54]-[56]. Based on the fact that the EMFs in the airgap depend on the excitation current and motor geometry, these studies can be classified into two categories: motor body geometrical modification [54] and control

approaches [51] [55] [56].

In this study, the TO is introduced to design the rotor of an SRM to explore the potential best design in terms of low electromagnetic vibration. The proposed method can be classified as the geometrical design approach. To the authors' knowledge, this is the first study that employs TO for an electromagnetic-structural Multiphysics problem. The TO method freely forms the rotor topology, it has the ability to discover the optimal structure without relying on the designer's prior knowledge [47]. Thus, the TO method is suitable for the early design of SRMs because it may bring efficient, radical, and sometimes unimaginable designs. To this end, the operation speeds that may evoke resonances of a 12/8 SRM are first elaborated. Next, electromagnetic-structural coupling FEM modeling is established and the stator vibration response caused by resonance is predicted. Then, the normalized Gaussian network (NGnet) method is employed to re-design the rotor for reducing the stator displacement caused by resonance. As the TO results, a novel rotor that employs the anchor-shaped pole with an inner window is found. Finally, the characteristics of the SRM with the novel rotor are investigated in detail for giving comprehensive conclusions.

5.2 The SRM and Multiphysics finite element modelling

5.2.1 SRM specification

As shown in Figure 5-1, a 3-phase 12/8 SRM is used as the numerical example. The SRM is driven by square current [56] shown in Figure 5-2. The pulsating EMFs along the SRM circumference can be developed in 2D Fourier series and be characterized by a series of progressive waves $acos(fN_r\omega t-r\theta+\varphi)$ of spatial order r (corresponding to a spatial wavenumber r)and temporal order f. For the 3-phase 12/8 SRM studied [51][58], the spatial-temporal feature of EMFs is

$$\begin{cases} r = 4 \times k \\ f = \pm 3 \times n + k \end{cases} \tag{4-1}$$

where k and n are arbitrary natural numbers. The negative of f indicates the opposite rotation direction. ω is the angular frequency of rotor rotation, N_r is the number of rotor poles In short, the EMFs with spatial order r=0 have the temporal order f=0, ±3, ±6,…; the EMFs with spatial order r=4 have the temporal order f=1, ±3+1 ±6+1,….

Figure 5-4 roughly shows the first six natural mode shapes of the cylindrical stator. Stator vibration happens on each natural mode. Especially, resonances will be evoked when two conditions are met: when the EMF circumferential pattern matches a natural mode deflection shape, and the EMF exciting frequency matches this mode frequency [51][53][55]. The main vibration modes depend on the slots per pahse. For the 3-phase 12/8 SRM studied, stator mode0 and mode4 contribute the greatest part to the acoustic noise when the SRM is driven at variable speed because resonances happen when the natural frequencies of mode0 and mode4 are close to the f of the EMFs with spatial order r=0 and r=4. The natural frequency of each mode of the stator can be obtained by hammer impact test or accurately predicted by structural FEM. Once the natural frequencies of mode0 and mode4 are known, the mechanical speeds that may induce resonances of this SRM can be predicted. The vibration response of these resonances can be simulated by electromagnetic-structural coupling FEM.

Even though some commercial software support forward design based on electromagnetic-structural coupling FEM, this study aims to explore the potential best design in an inverse way. Therefore, an in-house multiphysics FEM program is made for TO. Figure 5-5 shows the flow of the in-house FEM program. The solver used for all problems was the conjugate gradient method. Necessary technical details in this electromagnetic-structural coupling FEM modeling will be elaborated then.

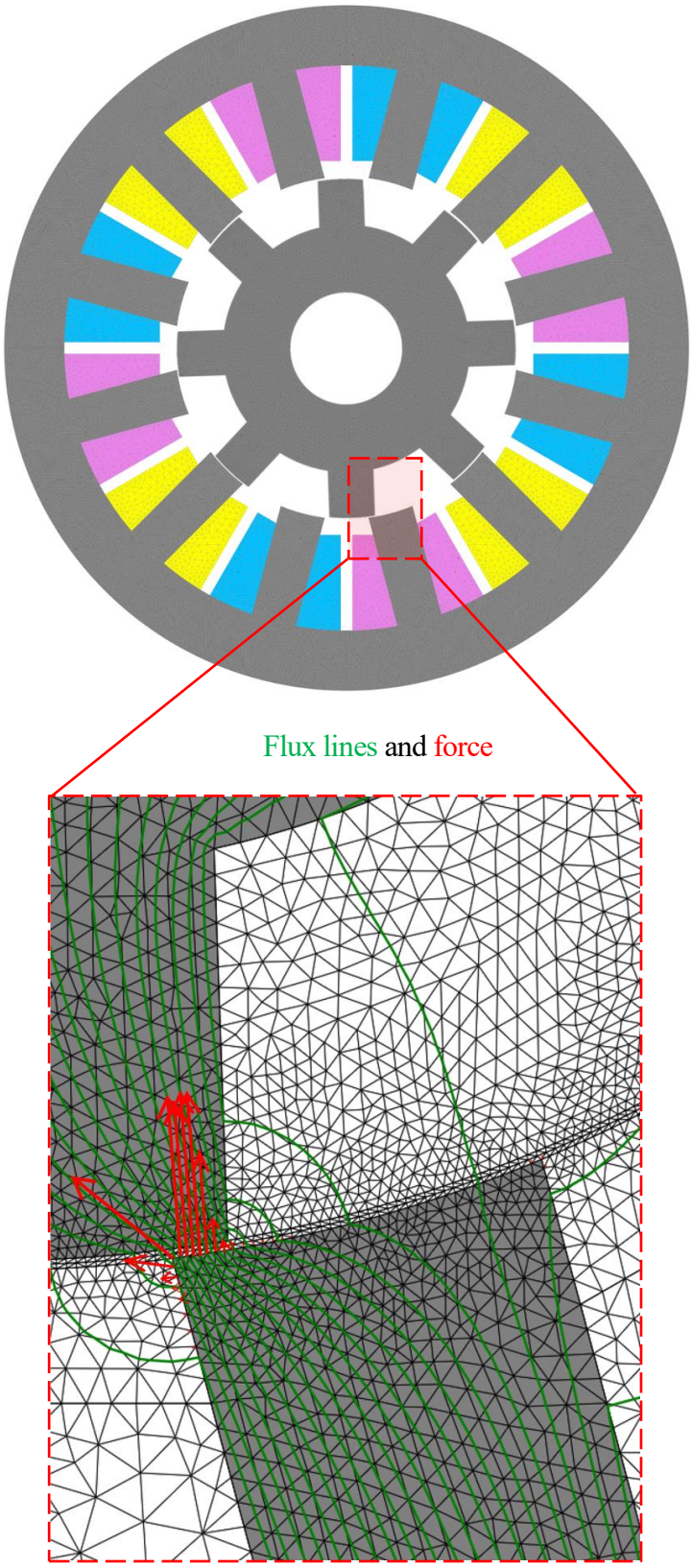

Fig.5-1 Three-phase 12/8 baseline SRM that will be optimized.

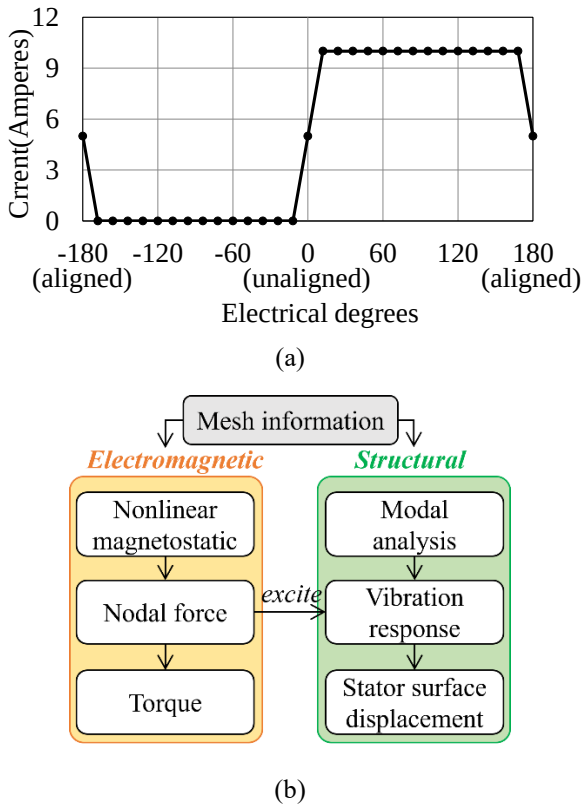

Fig.5-2 (a)Phase current (b)Flow of electromagnetic-structural FEM.

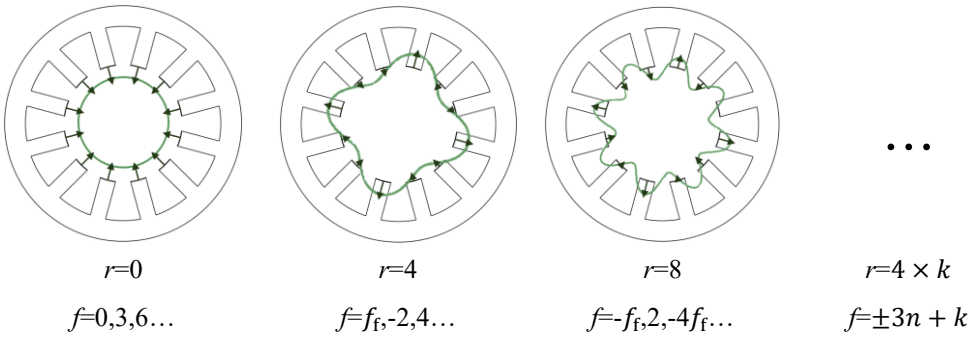

Fig.5-3 Spatial-temporal feature of the EMFs in 12/8 SRMs.

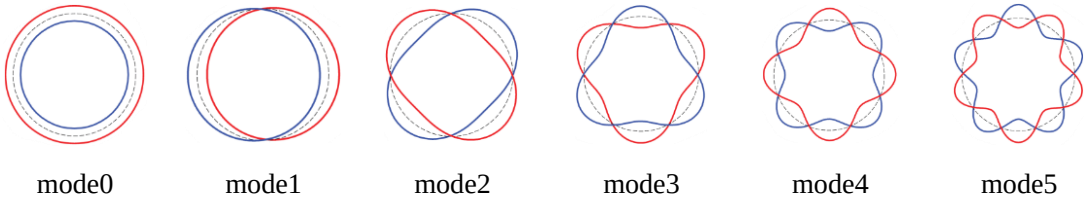

Fig.5-4 Circumferential mode shapes of a cylindrical shell.

5.2.2 2D magnetostatic FEM formulation

For the earlier design steps of SRMs, the 2D field models are sufficient to simulate the major machine performance in practice. To calculate the field, one has to solve Maxwell's equations. The nonlinear magnetostatic formulation is sufficient to model the SRM. To calculate the magnetic vector potential A, one has to solve the partial differential equation

$$\nabla \times (v\nabla \times \boldsymbol{A}) = \boldsymbol{J} \tag{4-2}$$

with proper boundary conditions. v and $\boldsymbol{J}$ depict the reluctivity and source current density. As shown in Figure 5-1, the EMF is calculated by the nodal force method, which can consider non-uniform EMF distribution for accurate vibration prediction.

5.2.3 2D structural FEM formulation

2D structural formulation is used for the stator core as it can predict vibration for motors with the invariant axial structure in a short time [53]. The meshing in the magnetostatic FEM is directly used for structural FEM to avoid the numerical error caused by the mesh-to-mesh EMF projection [58]. In addition, the Multiphysics coupling is with some reasonable assumptions:

(1) A weak coupling is assumed between electromagnetics and structural: airgap deflections do not change the flux distribution;

(2) Computed EMFs are supposed to be only due to Maxwell stress: magnetostriction forces are not considered;

(3) Undamped free vibration of stator core: impact of different installation methods in different industrial applications on the vibration response of the SRM is not considered.

The frequency response equation in a generally undamped system is as follows:

$$(\mathbf{K} - \omega^2\mathbf{M})\boldsymbol{x} = \boldsymbol{F} \tag{4-3}$$

where $\mathbf{K}, \mathbf{M} \in \mathbf{R}^{n\times n}$ are mass matrix and stiffness matrix. $\boldsymbol{x}$, $\boldsymbol{F} \in \mathbf{R}^n$ are nodal displacement and nodal EMFs. Mathematically, the natural modes and natural frequencies respectively correspond to the eigenvalues and eigenvectors of (3). The natural frequencies of stator mode0

and mode4 calculated by FEM are 8394Hz and 4963Hz, respectively. They are shown in Figure 5-8 in the next section.

Mode superposition method is used for frequency response analyses. Using this method, the vibration response of the stator can be approximated by a superposition of a small number of its first mth natural modes ($m \ll n$), (3) can be written as

$$(\boldsymbol{\Phi}^T \mathbf{K} \boldsymbol{\Phi} - \omega^2 \boldsymbol{\Phi}^T \mathbf{M} \boldsymbol{\Phi}) \boldsymbol{\delta} = \boldsymbol{\Phi}^T \boldsymbol{F} \tag{4-4}$$

where $\boldsymbol{\Phi} \in \mathbf{R}^{n \times m}$ is the modal matrix made by the first mth eigenvectors and $\boldsymbol{\delta} \in \mathbf{R}^m$ is displacement in the modal coordinates. m is set as 50. The $\boldsymbol{F}$ in (4) is given by the Fourier-transformed time domain EMFs, which had been calculated by the nodal force method in the magnetostatic formulation.

5.3 Optimization settings and results

5.3.1 Topology optimization settings

Stator vibration is the response of its structure to the applied EMFs. Especially, when the spatial-temporal characteristics of an EMF meet the two conditions of resonance, stator resonance will be evoked. Thus, it is a matter of course that stator resonance can be suppressed by suppressing the EMF which causes resonance, even without validating by structural FEM simulation. However, when the resonances of multiple modes are simultaneously evoked by different EMFs, the vibration response will be complex, it will thus be necessary to use the FEM for a precise evaluation. The TO is performed at the rotation speed of 5250rpm ($N_r\omega/2\pi$=700Hz). At this speed, the frequency of EMF with r=0 f=12 is close to the natural frequency of mode0 (8396Hz), and the frequency of EMF with r=4 f=7 is close to the natural frequency of mode4 (4965Hz). Thus, both mode0 and mode4 are evoked to induce the most serious vibration. The stator displacement of the SRM at different speeds can be found in Figure 5-10 in the next section. The TO aims to reduce the stator displacement while keeping at least 95% of the average torque.

NGnet method is a stochastic-based TO method proposed by the authors, technique details of this method can be found in [59]. By introducing NGnet method, the iron and air materials' distribution in the design domain is expressed by the output of the NGnet function. When a metaheuristic algorithm such as a genetic algorithm (GA) is used to optimize the real weightings of normalized Gaussians, the rotor can be wise-formed for improving the objective function of the GA. As shown in Figure 5-5(a), in order to maintain symmetry, 1/16 of the rotor is the design domain, other rotor space is slave domain. 30 2D Gaussians are placed in the design domain to manage the rotor topology. GA is used to steer the iterative optimization. The objective function of GA is defined as follows

$$objective\ function = \min\left(\frac{D}{D_0} - \frac{T_{ave}}{T_{ave0}} + penalty\right) \qquad (4\text{-}5)$$

$$penalty = \begin{cases} 10 * \frac{95\% * T_{ave0} - T_{ave}}{T_{ave}} & if(T_{ave} < 95\% * T_{ave0}) \\ 0 & if(T_{ave} > 95\% * T_{ave0}) \end{cases}$$

where T_{ave0}, T_{ave}, D_0, and D denote the average torque of the baseline SRM, average torque after optimization, average displacement of the baseline SRM, and average displacement after optimization, respectively. The acoustic noise sensed by the human eardrum is related to the frequency and severity of stator vibration. D and D_0 use average stator surface displacement of all calculated frequencies under 10000Hz to evaluate vibration.

Population and offspring sizes of GA are set as 200 and 90, respectively. Figure 5-6(b) shows the transitions of the objective function. It can be observed that GA converges after 150 generations. At that moment, 13700(200+90×150) designs have been evaluated, which takes about 7 days using a Xeon G6134 CPU.

5.3.2 Topology optimization results

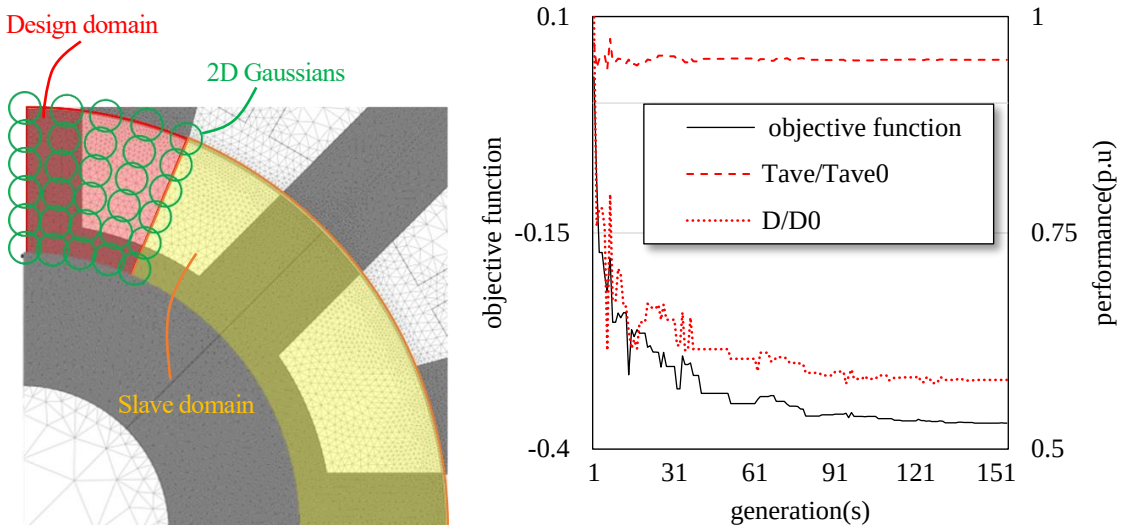

Fig.5-5 (a) Design domain of TO (b) Convergence history of the GA.

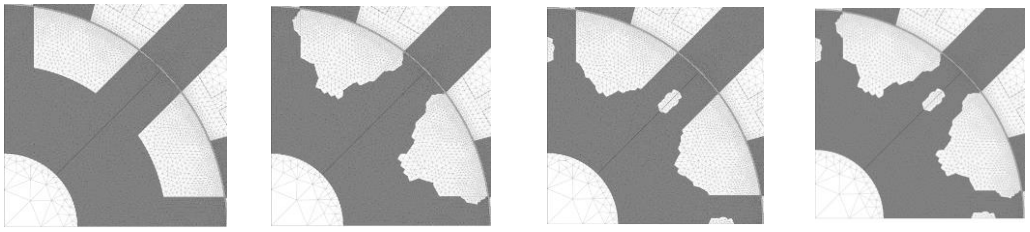

Fig.5-6 Different rotor topologies for the 12/8 SRM.

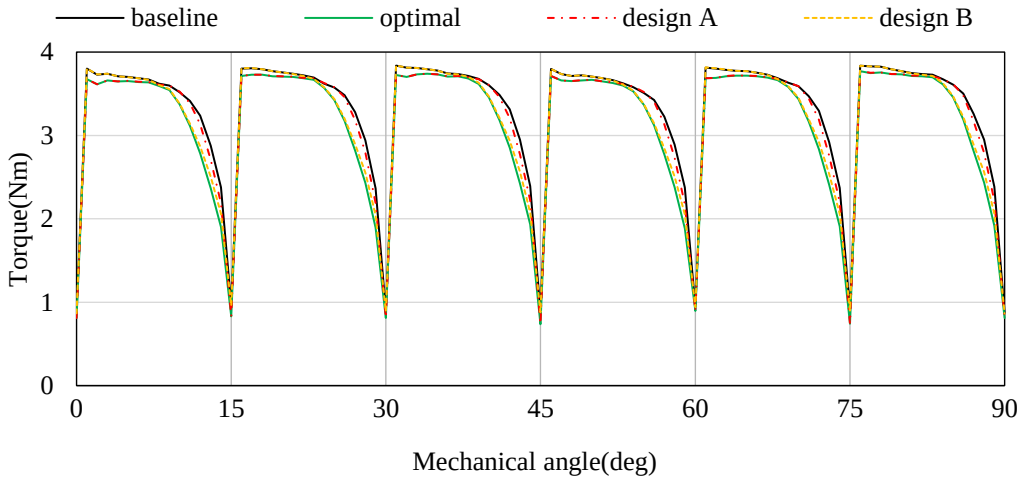

Fig.5-7 Torque waveforms of different SRMs.

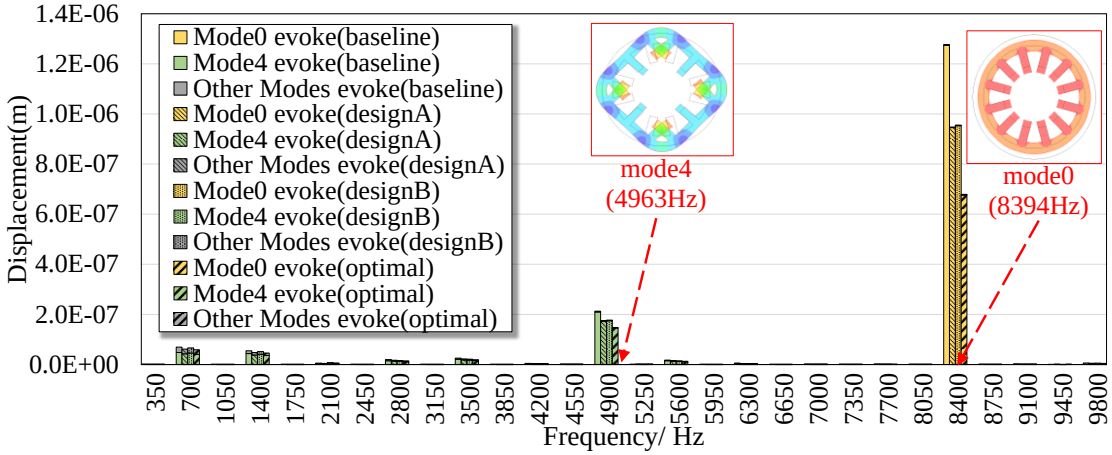

Fig.5-8 Stator displacement of SRMs predicted by mode-superposition method.

Figure 5-6(d) shows the optimal rotor design. A note of caution is that the optimal due here is in terms of the defined objective function since the trade-off between torque and displacement. The non-dominant solutions of torque and displacement can be explored by using multi-objective GA, which may consume more time. Compared with the baseline design shown in Figure 5-6(a), the optimal design has anchor-shaped poles with an inner window, the displacement of stator surface vibration has been reduced by 42% with only a 5% average torque loss. To investigate the optimized vibration, two designs respective with anchor-shaped poles and poles with inner windows are created, they are shown in Figure 5-6(b) and Figure 5-6(c). Torque waveforms of the four designs are compared in Figure 5-7. Adopting anchor-shaped poles can mitigate the decrease of torque while opening a window and chop the peak of torque. Both of them can help reduce the of EMFs' hammering to reduce vibration. Figure 5-8 compares the stator surface average displacement of the four SRMs. The displacement in Figure 5-8 is colored to indicate the contribution of different natural modes. Apparently, resonances happen on mode4 and mode0, and they are evoked by EMF with frequencies of 4900 Hz and 8400 Hz, respectively. This is consistent with previous theoretical analysis. Figure 5-8 also indicates that the anchor-shaped poles and inner windows have basically equivalent

contribution to the vibration suppression. With the help of these two design tactics, the stator resonances, especially the mode0-evoked resonance, are suppressed.

5.4 Investigation for the SRM with novel rotor

The results of Multiphysics simulation show that the novel rotor design found by TO can suppress the stator displacement caused by resonances at a certain operating condition. This is because the novel design changes the reluctance of the magnetic circuit around the poles of the SRM, the amplitudes of EMFs are therefore changed. The purpose of the current section is to comprehensively investigate the novel design provided by TO.

The static torque versus the rotor position of the four SRMs is presented in Figure 5-9a. During the unaligned (0°) and fully aligned (180°) positions, the torque is zero. The torque generation starts immediately after the stator and rotor alignment. It can be observed forming an anchor-shaped pole impacts the torque production at the start of alignment, whereas opening a window impacts the torque production before full alignment. The radial force is the main cause of vibration, the comparison of static radial force is shown in Figure 5-9b. While the radial force is minimum during unaligned positions (0° and 360°), it is maximized when the rotor and the stator poles are aligned (180°). The impact of forming an anchor-shaped pole and opening a window in reducing the radial force is very effective between 60° and 300°. Forming an anchor-shaped pole reduces the production of radial force, whereas opening a window chop the peak of the radial force waveform. When the two tactics are simultaneously employed to form the optimal design, the chump of radial force to the stator can be greatly mitigated. In addition, it can be observed these two design tactics influent radial force more than torque.

The stator displacement versus the rotation speed of the baseline and optimal SRMs is presented in Figure 5-10. Figure 5-8 is one slice of Figure 5-10. The dashed rays in Figure 5-

10 represent EMFs with different frequencies, they are always multiples of the mechanical frequency. The spatial orders of the EMFs are distinguished, r=0 is colored blue whereas r=4 is colored green. Horizontal solid lines in Figure 5-11 denote the natural frequencies of mode4 and mode0. The red and black circles in Figure 5-10 represent the stator surface average displacement of the baseline and optimal SRM, respectively. The diameter of circles denotes the displacement amplitude. The information contained in Figure 5-10 can be seen from two aspects. On one aspect, the resonances will happen when a green dashed line crosses the green solid line or a blue dashed line crosses the blue solid line because the two conditions for resonance are simultaneously met. The results provided by Multiphysics simulation are consistent with the theoretical analysis because of the size difference of rings. As for some significant displacements at low frequencies, they are forced displacements induced by low-frequency EMFs with very high amplitudes. On the other aspect, compared with the baseline SRM, the stator displacement of the optimal SRM at many resonance speeds is suppressed, not just the operating condition for TO. The suppressed displacement should be attributed to the effectively mitigated radial force. It should be noted that SRMs have a variety of drive strategies. Even though the impact of different drive strategies is not considered in Figure 5-10, the optimal SRM should be effective in suppressing resonance under different drive strategies, because the radial force has been suppressed.

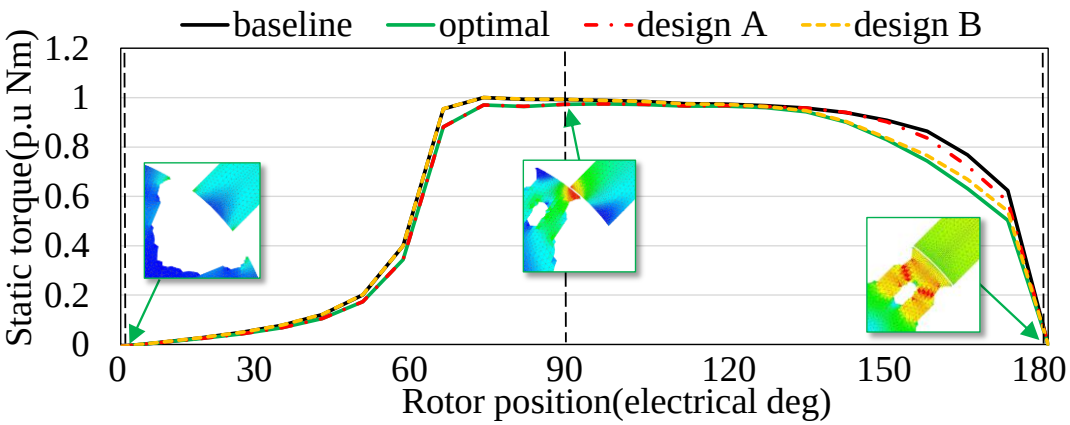

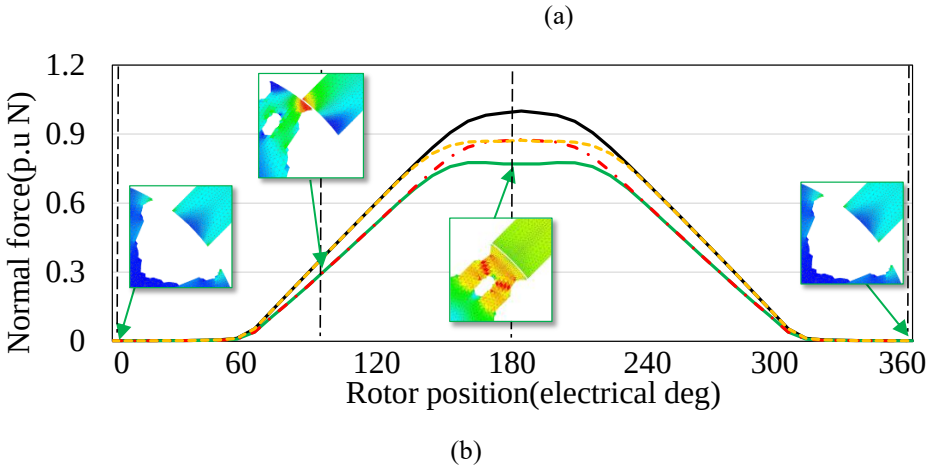

Fig.5-9 static force of the optimized SRM (a)static torque (b)radial force.

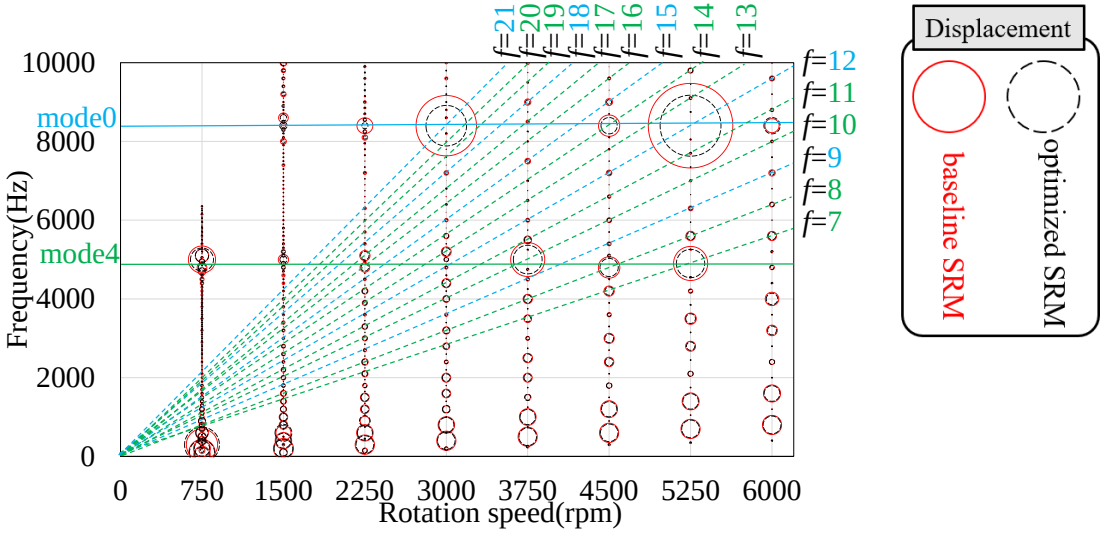

Fig.5-10 Vibration versus rotation speed of the baseline and optimal SRMs.

5.5 Conclusions

In this study, TO has been applied to a Multiphysics problem to extend its application boundary. TO is introduced to the design of an SRM for reducing the resonance-induced stator displacement. To this end, the electromagnetic-structural FEM coupling is established. As the TO result, adopting the anchor-shaped rotor pole and opening a window inner the rotor pole are discovered as two design tactics to mitigate stator resonances. With aid of the two tactics, the resonance-induced displacement is reduced by 42% with only a 5% average torque loss.

Further research should be undertaken on rotor optimization with considering different drive strategies and resonance speeds.

6 Hybrid optimization method for the permanent magnet machines

6.1 Simultaneous topology optimization and parameter optimization

Interior permanent magnet synchronous machines (IPMSMs) are playing important roles in many industrial applications and household appliances because of their excellent torque density, high efficiency, and high power factor[60]-[61]. IPMSMs have high flexibility in the rotor design because of the great number of PM geometrical parameters and the free-formed air barriers. The performance of an IPMSM can be significantly altered by modifying the shape of the PM and the air barriers[61].

With shortened time-to-market and increasingly stringent design specifications, optimal design methods are replacing the traditional trial-and-error design methods. Amongst these methods, a new way typically referred to as topology optimization (TO) is grabbing attention. In the TO method, material is wise-distributed in a design domain in a free-form manner. Thus, TO can create radical, efficient, sometimes unimaginable designs [62]-[68]. The broad category of TO method can be classified into gradient-based methods [62]-[64] and stochastic-based methods [65]. The ON/OFF method, which is a typical approach of the stochastic-based method, is well suited for electromagnetism TO problems because of its ability to treat multi-objective optimization. In general, when a TO method is used to design the rotor of an IPMSM, the designer first determines the layout of the permanent magnets (PMs) according to the existing design [66], then the topology of the air barriers is optimized by a TO method to discretize the modeling domain and element-wise assigning material properties for desired specifications such as higher torque, higher efficiency, lower ripple.

Albeit the magnetomotive force in the rotor is produced by the PMs, most studies about TO-based IPMSMs design have only focused on the optimal design of the free-formed air barriers, few studies have dealt with the simultaneous optimization of air barriers and PMs. For the optimal design of the rotor in an IPMSM, it is necessary to optimize the location and shape of

PMs as well, because the PMs not only provide the magnetic potential source but also can be considered as the barriers which provide additional reluctance torque. In [67] a magneto-structural combined dimensional and TO using the density method was presented, in which the machinability of the optimized rotor core was not well considered. *Hiruma* [68] proposed a hybridization method of parameter optimization (PO) and TO for PM machine design, in which the formulated multi-modal problem is hard to be solved efficiently because the PMs and air barriers are relatively independent. *Kuci* [69] attempted to combine PO and TO by solving an adjoint formulation by a sequential gradient-based convex programming approach, which can only treat single-objective optimization, in addition, the optimal design provided by a gradient method highly relays on the initial material distribution. As has been reported in these studies, it is a challenge to optimize the topology of air barriers and geometry parameters of PMs in an IPMSM simultaneously. The difficulty is how the topological and parametric variables are incorporated into a framework and then offer it to a solver for simultaneous optimization. In the case of a gradient-based solver being used, the problem that must be addressed is how to compute the shape sensitivities analytically, which will be a tedious calculation. In the case of a stochastic-based solver being used, the problem that must be addressed is how to find the global optimum efficiently for this multi-modal problem, since there exists an optimal topology under every possible PM layout.

Returning to TO methods. A stochastic-based TO method referred to as normalized Gaussian network (NGnet) method was proposed [59]. In the NGnet method, the topology expression by the ON/OFF state is reduced to a problem of parameter optimization by introducing Gaussian basis functions.

In this paper, the NGnet method is further extended to treat the problem of IPMSMs design, simultaneous topology optimization and parameter optimization (STOPO) is proposed. The

proposed STOPO can simultaneously optimize the geometry parameters of PMs and the topology of the air barriers by a genetic algorithm (GA) to unlock the full design potential in IPMSMs. To achieve this target, a number of innovations are made and reported in this paper. The innovations can be basically summarized in the following aspects:

(1) Integrating geometric variables of the PMs and the topology of the air barriers into one real-coded string by the NGnet method.

(2) Proposing using mesh smoothing technique for model regeneration to solve the formulated string. Using this way to regenerate models, a connection between the geometry of the PMs and the topology of the air barriers is made, consequently, the string can be solved by metaheuristics algorithms in a shorter time as the instructive topological features for IPMSMs design can be inherited in the iterative optimization.

(3) The current phase is co-optimized with the variation of rotor structure to explore the respective best torque profile of the new designs.

The rotor of a baseline IPMSM model is re-designed by the proposed SPOTO method. The SPOTO coupled with the Non-dominated Sorting Genetic Algorithm-II (NSGA-II) explored the border of some typical trade-off problems in IPMSMs design. As the design result, novel rotor structures with better torque profile and higher reluctance torque respective are found. It is verified the proposed STOPO method is useful in the conceptual design phase of IPMSMs as it can find optimal rotor structures from the full design space without relying on the experience and knowledge of the engineer.

The rest of this paper is organized as follows. Section II gives the specifications of the IPMSM to be designed. In section III, the flow of the proposed STOPO is elaborated, focusing on how the mesh smoothing technique influent the convergence of the GA. In section IV, the proposed STOPO is performed to treat two optimization problems. The efficiency of STOPO

and the novel designs provided by STOPO are discussed. Section V gives the conclusions.

6.2 Rotor structure considered

For cylindrical machines with lengths comparable to or larger than their diameters, two-dimensional (2D) field models are typically used to calculate the major machine parameters up to an accuracy that is sufficient in practice. Designing for a V-type IPMSM is used as the numerical example. Specifications of this machine can be found in Table I, the specifications originate from a baseline machine of IEE-Japan rotating machine committee [19]. Here we only focus on the design of the rotor. Figure 6-1 shows the design of the initial IPMSM. Due to the symmetry, 1/8 of the rotor is the design domain, the 1/4 model with 9358 meshes is solved. This IPMSM is driven by a sinusoidal current with an effective value of 3A. The temperature of the PMs and winding is assumed to be 60°C and 20°C, respectively. Meshing of this initial machine is accomplished by a commercial Finite element analysis (FEA) software named *FEMTET*, whereas the creation and solving of new designs are accomplished by an in-house program. This machine is solved in terms of a nonlinear magneto-static formulation. Static FEA simulation from 0° mechanical angle to 30° mechanical angle with a 1° interval is used to evaluate the performance of the IPMSM. This evaluation time is 5 seconds to 8 seconds, depending on the rotor structure, using an Intel Xeon 6134 processor.

Table 6-1 Specifications of the Initial IPMSM

Item(Unit)	Value
Stator diameter(mm)	112mm
Rotor diameter(mm)	55mm
Stack length(mm)	65mm
Air gap length	0.5mm

Number of turns per phase	35
Grade of NdFeB magnet	N45
Grade of core material	JIS 50A350
l	13mm
h	2.1mm
θ	22.5°

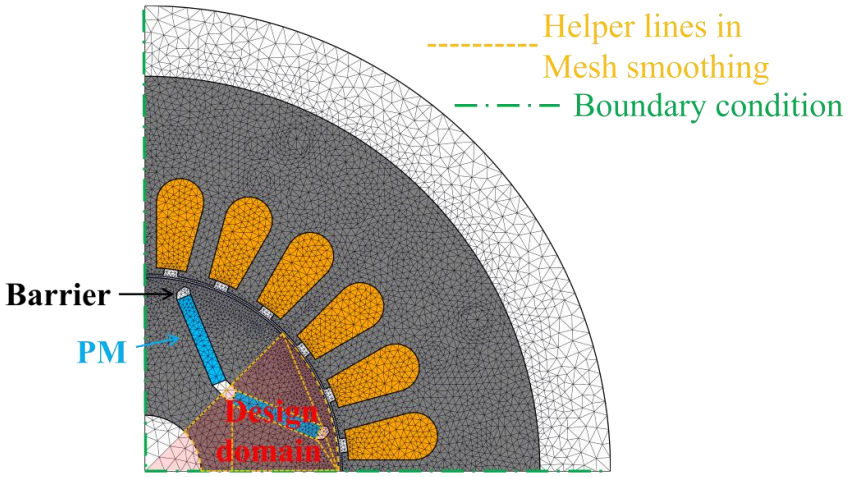

Fig. 6-1: Finite element model of the initial IPMSM.

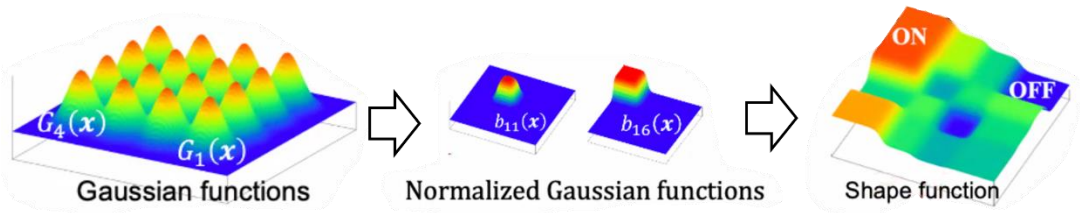

Fig. 6-2: NGnet method for topology optimization.

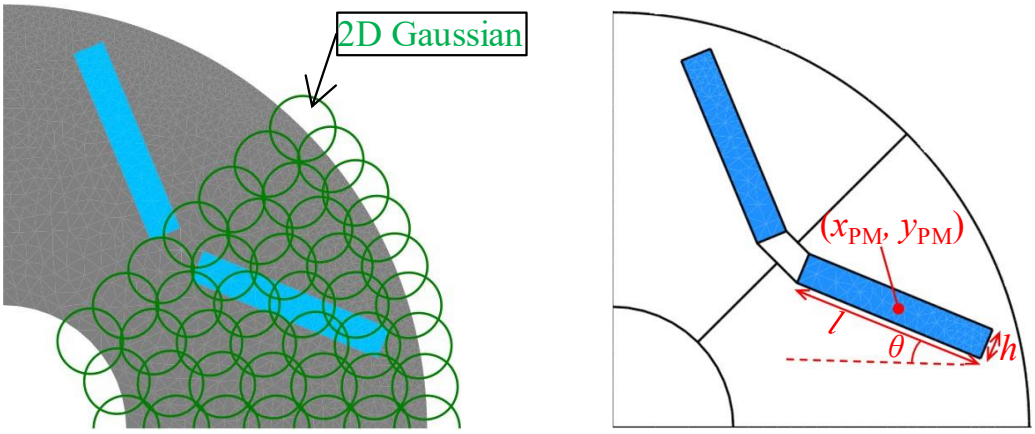

(a) (b)

Fig.6-3: (a)NGnet for topology optimization of air barriers (b) Five shape indicators for PMs.

6.3 Proposed SROPO method for IPMSM design

6.3.1 Topology expression

The NGnet method is utilized to express the free-formed air barriers. The basic concept of the NGnet method is briefly explained for the completeness of the article.

As shown in Figure 6-2, the NGnet method is a basis function-based method, it expresses the topology by the Gaussians uniformly distributed in the design space. In this method, the topology of the rotor core is expressed by the output of the NGnet function *f(x)*:

$$f(x) = \sum_{i=1}^{N} w_i b_i(x) \tag{5-1a}$$

in which N and x is the number of Gaussian and position vector, respectively. For this problem, 42 2D Gaussians uniformly distributed in the design domain are depicted in Figure 6-3(a). w_i denotes the weighting of the i-th normalized Gaussian function. b_i is the i-th normalized Gaussian function, which is:

$$b_i(x) = \frac{G_i(x)}{\sum_{k=1}^{N} G_k(x)} \tag{5-1b}$$

As the output of the NGnet is spatially smooth, different rotor core topologies can be expressed by adjusting the weightings of the normalized Gaussians. The boundary between iron

material and air material is depicted by the zero-contour of the NGnet. Specifically, in case the center of the j-th mesh in the rotor is described by c_j, if $f(c_j) \geq 0$, the j-th mesh will be filled by electrical steel (core), otherwise, it will be filled by air (barrier). Thus, the NGnet method reduces the TO problem to a parameter optimization (PO) problem in which the weightings (from -1 to +1) of the normalized Gaussians are variables. Stochastic algorithms such as GAs can be used to find the optimal weightings.

6.3.2 Parameter variables

To optimize the layout of the PMs, the geometry of the PMs in this IPMSM is parameterized as five indicators: length l, thickness h, PM angle θ, and PM center (x_{PM}, y_{PM}). To search all the potential designs as possible, there is no limit to the value of the five PM indicators in the STOPO process. As long as the deformation requirements of the mesh are met, a new PM configuration will be created.

The torque-current phase characteristic of an IPMSM can be greatly influenced by the modification of the PM layout and flux barriers. Thus, the current phase c must be optimized for each new-created design. Instead of repeating the FEA at different c to find the best torque profile of one new-created design, we add c as a variable for optimization to reduce the FEA counts required. Each new-created design is evaluated by FEA at the current phase c, which is randomly given by the GA. After the STOPO program is finished, it is verified that most of the designs on the Pareto front are correctly optimized and evaluated at their respective maximum torque per ampere (MTPA) current phase condition. To the authors' understanding, this is because the gradient feature of the torque-current phase curve makes the MTPA point can be easily found by a GA.

6.3.3 Flow of the proposed STOPO

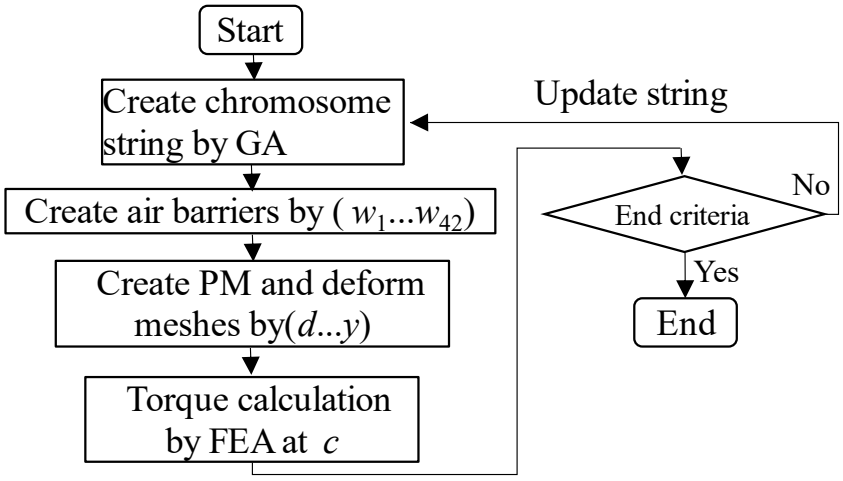

Fig.6-4: Flow of the proposed STOPO-smoothing for IPMSM design.

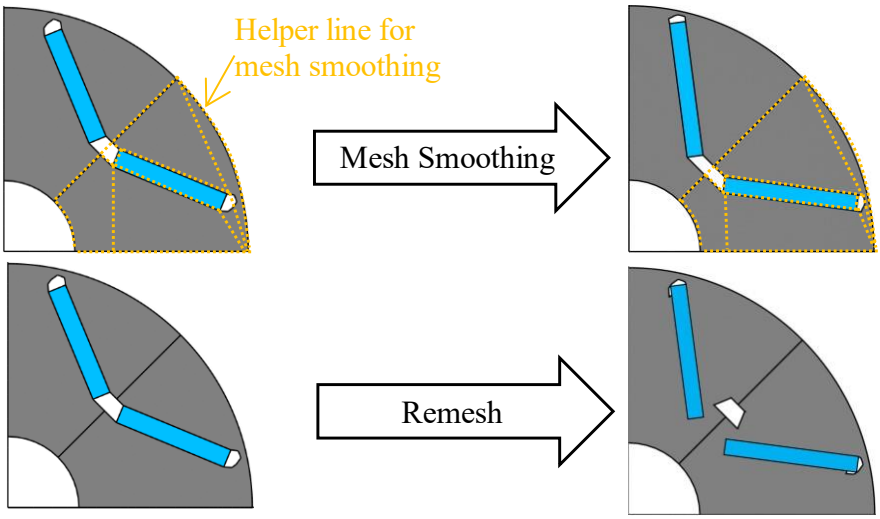

Fig.6-5: Comparison between remesh and mesh smoothing for regenerating a model with a new PM layout.

To perform STOPO, the real-coded variables that manage the core topology, PM layout, and the current phase are cascaded as follows:

$$\text{String} = [w_1, w_2, \ldots w_i, \ldots, w_{42}, l, h, \theta, x_{PM}, y_{PM}, c]$$

Since the only difference in the string between the traditional TO and the proposed STOPO is the additional shape indicators and current phase that are cascaded at the end, for a designer with the knowledge of TO, it is a natural idea to refer to TO and use a metaheuristics algorithm

such as GA to optimize this string. In this approach, the PM will be shaped according to the shape indicators, the topology of the rotor core will be created according to the weightings of the NGnet, then the FEA evaluation excited at a current phase c will be performed. The real-coded string will be updated by the GA to find a better design until converging. However, there exists a potential concern because there exists an optimal topology (i.e., one optimal w_1, w_2,…, w_{42}) for each PM layout (i.e., one l, h, θ, x_{PM}, y_{PM}). Especially, this problem cannot be ignored when multiple objective functions because there exists one Pareto front (i.e., many optimal w_1, w_2,…, w_{42}) for each PM layout (i.e., one l, h, θ, x_{PM}, y_{PM}). Consequently, the searching time of GA can be very long or even prohibitive as the landscape character of the STOPO problem is too multi-modal.

To solve this difficulty, we propose to use mesh smoothing to regenerate models with different PM configurations (i.e., different l, h, θ, x_{PM}, y_{PM}). GA can be used to update the string. The flow of the proposed STOPO hybridized by mesh smoothing (STOPO-smoothing) is shown in Figure 6-4. By introducing the mesh smoothing, a link between the air barriers and PM layout is made. More specifically, each Gaussian no longer manages material distribution near it in global coordinates but manages material distribution in relative positions with the PM as a reference coordinate. In this case, the air barrier location and shape information inherited by a GA is not the absolute location and shape in global coordinates, but its relative location and shape with PM. By this means, the search burden for the formulated multi-modal problem can be efficiently reduced because it is obvious that the optimal core topologies with different PM layouts have some common features. For example, the air barriers should not be near the magnetization direction of the PMs but should be near the two sides of the PMs to guide the fluxes.

We give an example, in which the bits that manage the air barriers (i.e., w_1, w_2,…, w_{42}) are

unchanged while the bits that manage the PM layout (i.e., l, h, θ, x_{PM}, y_{PM}) are modified, to clearly explain how the model regeneration methods influent the convergence of GA. As shown in Figure 6-5, in the case of mesh smoothing being used for model regeneration, the topological features of the iron core relative to the PMs are kept. In the case of remesh being used for model regeneration, in contrast, the weightings of NGnet (i.e., w_1, w_2,…, w_{42}) are no longer instructive in the rotor design with a new PM layout. It can thus be easily understood that the mesh smoothing can make a connection between the air barriers and PM layout, allowing the weightings of NGnet (i.e., w_1, w_2,…, w_{42}) still be instructive in the rotor design for a new crated PM layout (i.e., l, h, θ, x_{PM}, y_{PM}). It can be also inferred that the search efficiency of the GA can be significantly improved by introducing mesh smoothing for model regeneration.

There are several methods for mesh smoothing: Laplace smoothing, Winslow smoothing, Deformable Complex method, etc. Since the flexible layout of PMs in the IPMSM, that is, not only translation, scaling, but also rotation, the mesh deformation method must ensure that there is no mesh folding. Furthermore, the computation time for mesh deformation must be short, as the GA may need to evaluate a large number of different rotor designs before it converges. Therefore, a subdomain-based Laplace mesh deformation method is introduced.

The subdomain-based Laplace mesh smoothing technique, which was originally proposed by an engineer from *COMSOL* [70] for fast model regeneration in fluid-structure problems, is introduced. In this method, the domain needed for mesh smoothing (TO domain in this paper) is firstly divided into some subdomains by the helper lines, then following Laplace's equation is solved in each subdomain independently for achieving the new node positions:

$$\begin{cases} \frac{\partial^2 x}{\partial X^2} + \frac{\partial^2 x}{\partial Y^2} = 0 \\ \frac{\partial^2 y}{\partial X^2} + \frac{\partial^2 y}{\partial Y^2} = 0 \end{cases} \tag{5-2}$$

where X, Y x, y, are the vertex positions of the nodes in each subdomain before and after

deformation, respectively.

In the subdomain-based Laplace mesh smoothing technique, the mesh folding will never happen if only each subdomain is still a convex polygon. Moreover, the processing time of this method is fast, the processing time for this problem (more than 1000 nodes in the rotor) is about 0.2 seconds.

6.3.4 Settings for optimization Algorithm

In this study, the NSGA-II is adopted to treat the trade-off problems in IPMSM design. The settings of NSGA-II can be found in Table II. The population size is 500 to ensure diversity and avoid converging to the local optimal designs. The five PM shape indicators and the current angle are randomly given in the initial populations to randomly create the configuration of the PMs. The core shape of the initial populations is randomly created by specifying a random number between -1 and 1 for each *w*.

The NSGA-II will keep updating the string until the Pareto front is not improved for 30 generations. Correspondingly, the Pareto front provided when NSGA-II stops are seen as the design boundary that can be provided.

Table 6-2 Settings of NSGA-II

Item	Value
Crossover type	BLX-α
Crossover rate α	0.4
Selection method	Roulette
Pareto sorting method	Crowd distance
Population size	500
Offspring in one generation	200

Elapsed time for one generation	About 0.3 hours

6.4 Rotor design results

In this section, the traditional NGnet-based TO is firstly performed for the rotor core to provide a baseline result for comparison. Then, the optimization results of STOPO realized by remesh (STOPO-remesh) and the proposed STOPO hybridized by mesh smoothing (STOPO-smoothing) are compared in the same optimization problem. It will be confirmed that STOPO-smoothing can find better designs in a lesser time in comparison with the STOPO-remesh. The usefulness of the proposed STOPO-smoothing for the conceptual design phase of IPMSMs will be proved by the optimization results of two case studies, which respective aim to improve the torque property and reduce PM volume.

6.4.1 Results of traditional TO

In this part, the traditional NGnet-based TO is performed to provide a result for comparison. The traditional TO aims to maximize average torque and minimize torque ripple by re-designing the air barriers. For this TO problem, the chrome string that will be optimized by NSGA-II is:

$$\text{String} = [w_1, w_2, \ldots w_i, \ldots, w_{42}] \tag{5-53a}$$

The objective function is:

$$\begin{cases} \text{Maximize}(f_1 = T_{ave}) \\ \text{Minimize}(f_2 = T_{rip}) \end{cases} \tag{5-3b}$$

$$\text{subject to} \begin{cases} n_{connected} = 1 \\ \sigma_{eqv} < 320\text{Mpa} \end{cases} \tag{5-3c}$$

where T_{ave} and T_{rip} are the average torque and torque ripple of a new-created design, respectively. $n_{connected}$ is the number of connected core, this construction aims to avoid evolving a topology that has unconnected island cores. σ_{eqv} denotes the Von-Mises stress. In traditional

TO, the current phase *c* for new-created designs is set as 19°, which is the MTPA condition of the initial IPMSM.

The moving of the Pareto front stops from the 210th generation, thus, the Pareto front in the 210th generation is considered the design border that could be provided by traditional NGnet-based TO.

Three optimal designs on the design border are shown in Figure 6-7. They are the design that provides maximum average torque (Design-TO1), the design that provides minimum torque ripple (Design-TO2), and the design that keeps a balance between the average torque ripple (Design-TO3). One interesting optimization result is that the Design-TO1 almost has the same air barrier design as the initial IPMSM. Compared with the initial IPMSM, the air barriers in Design-TO1 are designed as larger as possible to reduce the flux leakage of PMs, which is the reason why the average torque is improved. It can be considered that the reappearance of this air barrier design verifies that the NGnet method can provide a good global search for the TO problem.

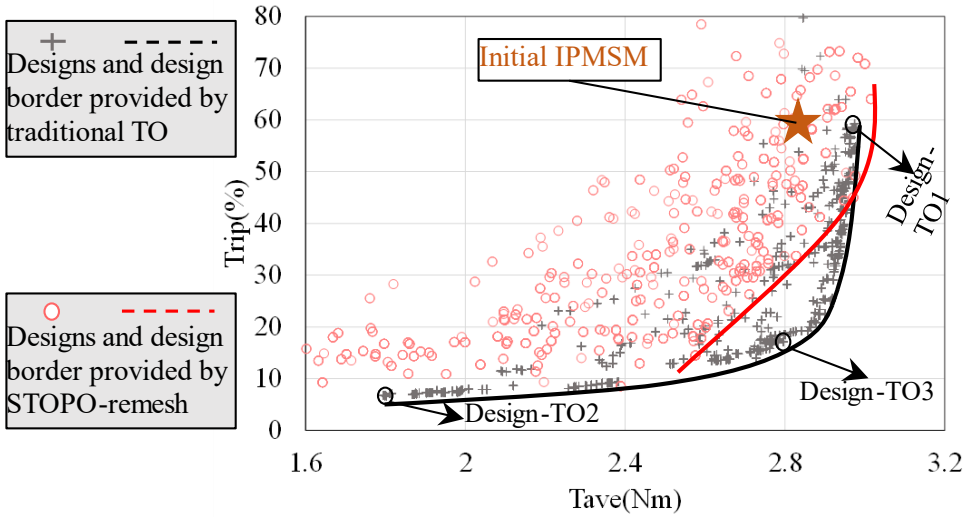

Figure 6-6: Design borders provided by traditional TO and STOPO-remesh.

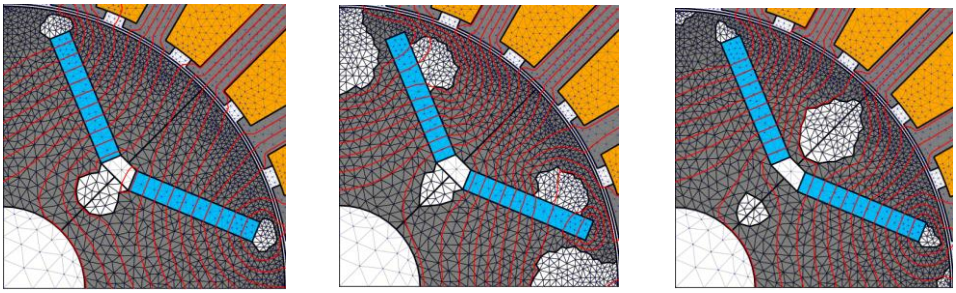

Design-TO1 Design-TO2 Design-TO3

Figure 6-7: Optimal designs provided by traditional TO.

6.4.2 STOPO-remesh for torque property enhancement

found the border of average torque and torque ripple when the air barriers in the rotor can be freely designed. However, for the optimal rotor design of an IPMSM, it is necessary to optimize the PM layout and air barriers simultaneously. For this purpose, we have performed the STOPO in this and the following part to maximize average torque and minimize torque ripple on the premise that the same PM volume as the above TO. It should be noted that the STOPO in this part did not adopt mesh smoothing to regenerate new-created designs. In this case, the remesh is performed to create the PMs according to [l, h, θ, x, y], then the air barriers will be formed according to [w_1, w_2, …w_i, …, w_{42}], as have been described in the Section-II. The existence of this part aims to compare the results provided by STOPO-remesh and STOPO-smoothing.

For the optimization problem in this part, the string that will be optimized by NSGA-II is:

$$\text{String} = [w_1, w_2, \ldots w_i, \ldots, w_{42}, l, h, \theta, x_{\text{PM}}, y_{\text{PM}}, c] \quad \text{(5-4a)}$$

The objective function is:

$$\begin{cases} \text{Maximize}(f_1 = T_{ave}) \\ \text{Minimize}(f_2 = T_{rip}) \end{cases} \quad \text{(5-4b)}$$

$$\text{subject to} \begin{cases} V_{\text{PM}} = V_{\text{PM\_initial}} \\ n_{connected} = 1 \\ \sigma_{eqv} < 320\text{Mpa} \\ h > 1.5\text{mm} \end{cases} \quad \text{(5-4c)}$$

The moving of the Pareto front stops from the 650th generation. As shown in Figure 6-6, the

Pareto front in the 650th generation is considered the design border that could be provided by STOPO-remesh. Disappointingly, the higher design freedom cannot make STOPO-remesh gain a Pareto front that fully exceeds that provided by traditional TO. The STOPO-remesh converged to some local optimal designs even though the population size is big enough. This result is not unforeseen since STOPO is not simply increased from 42 to 47 optimization variables compared to traditional TO. In fact, for each possible combination of PM shape indicators, a Pareto front exists, making the landscape of this problem too multi-modal to be explored efficiently by a stochastic algorithm.

6.4.3 STOPO-smoothing for torque property enhancement

The STOPO-remesh failed to provide a design border that fully exceed that provided by traditional TO. In this part, the STOPO-smoothing is performed to the same problem. The string that will be optimized by NSGA-II is the same as Equation (4a) in the above part. The target and settings are the same as Equation (4b) and Equation (4c) in the above part.

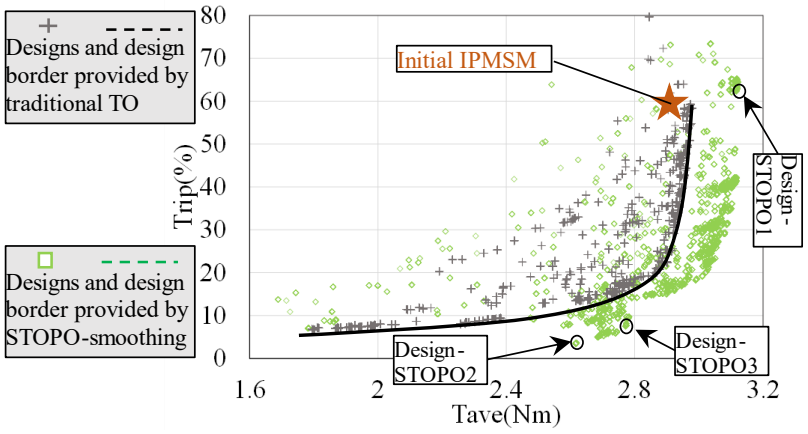

Figure 6-8 Design borders provided by traditional TO and STOPO-smoothing.

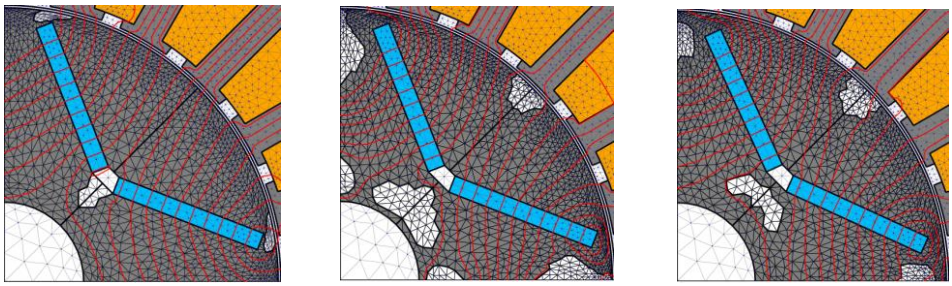

Design-STOPO1 Design-STOPO2 Design-STOPO3

Figure 6-9 Optimal designs provided by STOPO-smoothing.

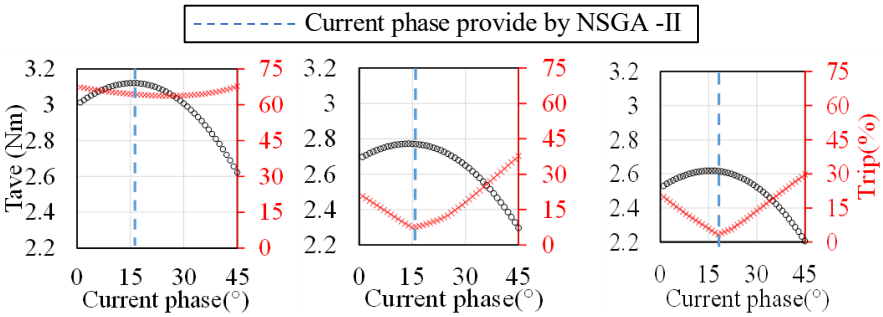

Design-STOPO1 Design-STOPO2 Design-STOPO3

Figure 6-10 Torque property of the optimal designs.

The moving of the Pareto front stops from the 300th generation, thus, the Pareto front in the 300th generation is considered the design border that could be provided by the proposed STOPO-smoothing. The design border is shown in Figure 6-8. The design border provided by the proposed STOPO-smoothing fully exceeds that provided by traditional TO thanks to the rotor can be formed more freely. Considering that the time-consuming of the proposed STOPO-smoothing is about 1.5 times that of conventional TO, it is obviously STOPO-smoothing is more attractive and practical in terms of IPMSM design. On the other hand, by comparing the results provided by the STOPO-remsh and STOPO-smoothing, it is confirmed that the mesh smoothing technique makes this multi-modal problem can be solved more efficiently due to the instructive topological features for IPMSMs design are inherited in the iterative optimization. Three optimal designs on the design border provided by the proposed STOPO-smoothing are

shown in Figure 6-9. They are the design that provides maximum average torque (Design-STOPO1), the design that provides minimum torque ripple (Design-STOPO2), and the design that keeps a balance between the average torque ripple (Design-STOPO3). It can be observed that the PM becomes slender in the three designs. This PM shape can reduce the reluctance in the main magnetic circuit thus improving the torque. Therefore, it can be considered that the main reason why the proposed STOPO can provide higher average torque than traditional TO is that better PM shapes are found.

The torque property of the three optimal designs with respect to different current phases is shown in Figure 6-10. An unexpected finding from this case study was that the torque ripple of an IPMSM under a certain operating condition can even be significantly lower than the cogging torque if the rotor is well-designed. For Design-STOPO3 shown in Figure 6-10, its minimum torque ripple can be 3% (0.08Nm), which is even lower than its cogging torque (0.21Nm) under no-load condition. This can be explained as follows: in IPMSMs, the output torque of IPMSMs can be regarded as the superposition of PM torque and reluctance torque [71]-[73], and the respective phases during superposition are determined by the current angle. Thus, the torque ripple of an IPMSM may vary greatly with the rotor structure and current angle. Since the current phase can co-evolve with the rotor structure, the STOPO found much better designs in terms of torque ripple in comparison with the traditional TO.

The optimization results indicate that STOPO-smoothing can simultaneously optimize the topology and parameter variables and find better designs compared to traditional TO, in addition, the search of optima is high-efficient due to the mesh smoothing making a connection between the core topology and the shape of PMs.

6.4.4 STOPO-smoothing for reducing PM volume

It has been confirmed that the proposed STOPO-smoothing can find better designs compared

to traditional TO thanks to the rotor can be formed more freely. In this part, the proposed STOPO-smoothing is performed for another optimization problem, which aims to keep the torque property while reducing the PM volume (V) as possible. In this problem, the string that will be optimized by NSGA-II is:

$$\text{String} = [w_1, w_2, \ldots w_i, \ldots, w_{42}, l, h, \theta, x_{PM}, y_{PM}, c] \tag{5-5a}$$

The objective function is:

$$\begin{cases} maximize(f_1 = 1.2 \times \frac{T_{ave}}{T_{ave\_base}} - 0.2 \times \frac{T_{rip}}{T_{rip\_base}}) \\ minimize(f_2 = \text{V}) \end{cases} \tag{5-5b}$$

$$\text{subject to} \begin{cases} n_{connected} = 1 \\ \sigma_{eqv} < 320\text{Mpa} \\ h > 1.5\text{mm} \\ m_{max} - m_{min} < 150° \end{cases} \tag{5-5c}$$

where T_{ave_base} and T_{rip_base} are the average torque and torque ripple of the initial IPMSM. m_{max} and m_{min} are the maximum inner angle and minimum inner angle of a mesh, respectively. Limiting their difference aims to avoid creating flat meshes.

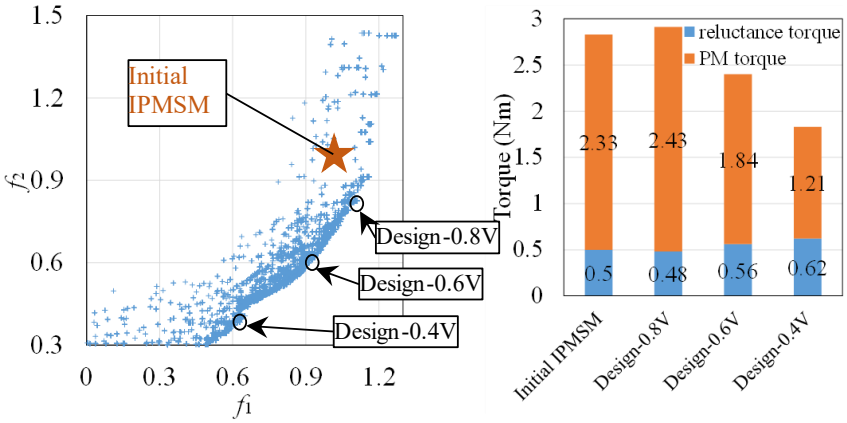

(a) (b)

Figure 6-11: (a) Pareto front provided by the proposed STOPO-smoothing (b) Reluctance torque of the designs.

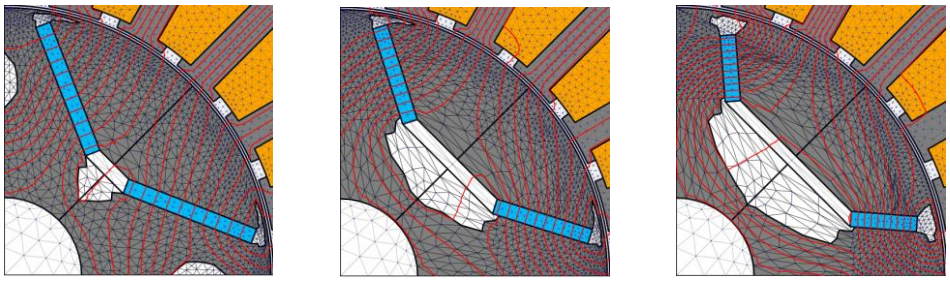

Design-0.8V Design-0.6V Design-0.4V

Figure 6-12: optimal designs provided by the proposed STOPO-smoothing.

For this design problem, the moving of the Pareto front stops from the 200th generation. The Pareto front is shown in Figure 6-11(a). Three optimal rotor designs on the Pareto front are studied in detail, they are the design with 80%V (Design-0.8V), 60%V (Design-0.6V), and 40%V (Design-0.4V), respectively. The three designs are shown in Figure 6-12. Interestingly, the structure of Design-0.4V has many similarities with the Permanent Magnet Assisted Synchronous Reluctance Motor (PMA-synRM) [74]. Thus, the PM torque and reluctance torque of respective design was computed by

$$\text{PM torque} = p\theta_a i_q \tag{5-6a}$$

$$\text{reluctance torque} = p(L_d - l_q) i_d i_q \tag{5-6b}$$

where p, θ_a, L_d, L_q, i_d, i_q are the number of the pole pairs, magnet flux, d-axis inductance, q-axis inductance, d-axis current, and q-axis respectively [18]. The computation results are shown in Figure 6-11(b), it is confirmed the proportion of reluctance torque increases with the reduction of PM volume.

It can be found from the optimal designs on the Pareto front that as PM volume decreases, an air barrier appears on the d-axis. For engineers with IPMSM design experience, when the magnetomotive force provided by the PM is limited, the only way to increase the output torque is to increase the reluctance torque as possible, that is, to design the motor from IPMSM to

PMA-synRM. This is in a line with the appeared air barrier on the d-axis provided by the proposed STOPO-smoothing. Surprisingly, the STOPO-smoothing successfully formed the rotor in this right way without relying on any prior knowledge.

6.5 Conclusions

A STOPO has been proposed to simultaneously optimize the layout parameters of PM and topology of air barriers in IPMSMs. Comparative numerical results show that the proposed STOPO can provide much better designs compared with traditional TO within a comparable time-consuming. Optimization results of two case studies prove the proposed method is useful and practical in the conceptual and innovative design of IPMSMs because the proposed method can find optimal rotor structures from the full design space without relying on the experience and knowledge of the engineer.

The present study has investigated the applicability and efficiency of the proposed STOPO in detail in the electromagnetic design. Further research will be conducted on the STOPO-based IPMSMs conceptual design considering more comprehensive evaluation indicators such as loss, lightweight, and NVH.

List of Publication

Peer-viewed journal paper

[1] Z. Sun, K. Watanabe and X. Xu, "Derivation of optimal rotor topologies for consequent-pole PMSM by ON/OFF method," *CES Transactions on Electrical Machines and Systems*, vol. 5, no. 4, pp. 301-310, Dec. 2021, doi: 10.30941/CESTEMS.2021.00035.

[2] Z. Sun, K. Watanabe and X. Xu, "Design Optimization of Consequent-Pole PMSM by ON/OFF Method and Multi-Objective Evolutionary Algorithms," *International Journal of Applied Electromagnetics and Mechanics*, 2022. doi: 10.3233/JAE-210149.

[3] Sun Zhen, Sato Takahiro, and Watanabe Kota. "An Efficient Combination of Topology Optimization and Parameter Optimization for Electromagnetic Devices". *International Journal of Applied Electromagnetics and Mechanics*, 2022, doi: 10.3233/JAE-220108

[4] Sun Zhen, Xu Xiaozhuo, and Watanabe Kota. "Minimizing detent force of permanent magnet linear synchronous machines by designing mover using mesh-level stochastic shaping". *Energy Reports*, https://doi.org/10.1016/j.egyr.2023.05.138

[5] Sun Zhen and Watanabe Kota. "An Improved ON/OFF Method with a Two-step Surface Smoother for Topology Optimization of Electromagnetic Devices". *COMPEL - The international journal for computation and mathematics in electrical and electronic engineering*. Vol. ahead-of-print No. ahead-of-print. https://doi.org/10.1108/COMPEL-12-2022-0432.

[6] Sun Zhen, Sato Takahiro and Watanabe Kota. "Topology Optimization and Parameter Optimization Hybridized by Mesh Smoothing for IPMSM Design". *COMPEL - The international journal for computation and mathematics in electrical and electronic engineering*, Vol. ahead-of-print No. ahead-of-print. https://doi.org/10.1108/COMPEL-12-2022-0426.

[7] Zhen Sun, Hiroto Otsuki, Takahiro Sato, Kota Watanabe，"Topology Optimization of a

Switched Reluctance Machine by Electromagnetic-Structural Multiphysics Finite Element Analysis", *IEEE Transactions on Magnetics*，DOI: 10.1109/TMAG.2023.3301903.

International conference

[1] Z. Sun, K. Watanabe and X. Xu, "Topology Optimization of PMSM with Consequent-Pole using ON/OFF Method", *IEEE International Magnetics Conference*, France, April 7th 2021.

[2] Z. Sun, K. Watanabe and X. Xu, "Influence of Slot and Pole Number Combinations on PMLSM with Consequent Pole," *13th International Symposium on Linear Drives for Industry Applications*, China, July 1st 2021.

[3] Z. Sun, K. Watanabe and X. Xu, "Design Optimization of Consequent-Pole PMSM by ON/OFF Method and Multi-objective Evolutionary Algorithms", *16th International Workshop on Optimization and Inverse Problems in Electromagnetism*, Poland, September 6th 2021.

[4] Z. Sun, K. Watanabe and X. Xu, "Topology Optimization based on ON/OFF Method and Immune Algorithms for Thrust Ripple Minimization of PMLSMs," *23rd International Conference on the Computation of Electromagnetic Fields*, Mexico, January 16th 2022.

[5] Z. Sun, and K. Watanabe, "Multi-material Topology Optimization of Permanent Magnet Motors Based on ON/OFF Method," *23rd International Conference on the Computation of Electromagnetic Fields*, Mexico, January 16th 2022.

[6] Sun Zhen, Sato Takahiro, and Watanabe Kota. "An Efficient Combination of Topology Optimization and Parameter Optimization for Electromagnetic Devices". *The 20th International Symposium on Applied Electromagnetics and Mechanics*. June, 2022.

[7] Sun Zhen, Sato Takahiro, and Watanabe Kota. "An Efficient Combination of Topology Optimization and Parameter Optimization for Electromagnetic Devices". *The 20th IGTE Symposium on Computational Methods in Electromagnetics and Multiphysics*. September, 2022.

[8] Sun Zhen and Watanabe Kota. "An Improved ON/OFF Method with a Two-step Surface Smoother for Topology Optimization of Electromagnetic Devices". *The 20th IGTE Symposium*

on Computational Methods in Electromagnetics and Multiphysics. September, 2022.

[9] Sun Zhen, Xu Xiaozhuo, and Watanabe Kota. "Minimizing detent force of permanent magnet linear synchronous machines by designing mover using mesh-level stochastic shaping". *International Conference on Power and Electrical Engineering*, December, 2022.

[10] Z. Sun, H. Otsuki, T. Sato, and K. Watanabe and X. Xu, "Topology Optimization for Switched Reluctance Machine Using Electromagnetic-Structure Multiphysics Finite Element Analysis," *24rd International Conference on the Computation of Electromagnetic Fields*, Japan, May, 2022.

[11] Z. Sun, X. Xu, and K. Watanabe and, "Zeroization of End Effect Detent Force on Permanent Magnet Linear Synchronous Motors by Designing the Topology of Mover Ends," *24rd International Conference on the Computation of Electromagnetic Fields*, Japan, May, 2022.

[12] Z. Sun and K. Watanabe and, "Analysis of Zeroth-Mode Vibration of Switched Reluctance Motors," *24rd International Conference on the Computation of Electromagnetic Fields*, Japan, May, 2022.

References

[1]. Salon, Sheppard Joel. Finite element analysis of electrical machines. Vol. 101. Boston: Kluwer academic publishers, 1995.

[2]. Mahmoudi, Amin, et al. Design, analysis, and prototyping of an axial-flux permanent magnet motor based on genetic algorithm and finite-element analysis. IEEE Trans. Magn. Vol.49, 2012.

[3]. Sigmund, Ole, and Kurt Maute. Topology optimization approaches: A comparative review. Structural and Multidisciplinary Optimization 48.6 (2013): 1031-1055.

[4]. Rozvany, George IN. A critical review of established methods of structural topology optimization. Structural and multidisciplinary optimization 37 (2009): 217-237.

[5]. Andreassen, Erik, et al. Efficient topology optimization in MATLAB using 88 lines of code. Structural and Multidisciplinary Optimization 43 (2011): 1-16.

[6]. Hieda, Naoya, et al. Function expansion based topology optimization of NRD guide device using hybrid method of harmony search and gradient method. IEICE Electronics Express 20.5 (2023): 20230012-20230012.

[7]. Dbouk, Talib. A review about the engineering design of optimal heat transfer systems using topology optimization. Applied Thermal Engineering 112 (2017): 841-854.

[8]. S. U. Chung, J. W. Kim, Y. D. Chun, B. C. Woo, and D. K. Hong. Fractional slot concentrated winding PMSM with consequent pole rotor for a low-speed direct drive: reduction of rare earth permanent magnet. IEEE Trans. Energy Convers., vol.30, 2015, pp. 103–109.

[9]. J. Li, K. Wang, and F. Li. Analytical prediction of optimal split ratio of consequent-pole permanent magnet machines. IET Electr. Power Appl., vol.12, 2017, pp. 365-372.

[10].Z. Z. Wu and Z. Q. Zhu. Comparative Analysis of End Effect in Partitioned Stator Flux

Reversal Machines Having Surface-Mounted and Consequent Pole Permanent Magnets. IEEE Trans. Magn., vol. 52, 2016, pp. 1-4.

[11].H. Dhulipati, S. Mukundan, Z. Li, E. Ghosh, J. Tjong and N. C. Kar. Torque Performance Enhancement in Consequent Pole PMSM Based on Magnet Pole Shape Optimization for Direct-Drive EV. IEEE Trans. Magn., vol. 57, 2021, pp. 1-7.

[12].Paplicki, Piotr et al. Hybrid Excited Electric Machine with Axial Flux Bridges. Int. J. Appl. Electromagn. Mech. vol. 59, 2019, pp. 703-711.

[13].Z. Sun, K. Watanebe and X. Xu, Derivation of optimal rotor topologies for consequent-pole PMSM by ON/OFF method. CES Transactions on Electrical Machines and Systems, vol. 5, no. 4, pp. 301-310, Dec. 2021.

[14].K. Deb, A. Pradiscover, S. Agarwal, T. Meyarivan. A fast and elitist multiobjective genetic algorithm: NSGA-II. IEEE Trans. Evol. Comput., vol. 6, 2002, pp. 182-197.

[15].E. Zitzler, M.Laumanns, L. Thiele. SPEA2: Improving the strength Pareto evolutionary algorithm. TIK-report, 2001, 103.

[16].S. Doi, H. Sasaki and H. Igarashi. Multi-Objective Topology Optimization of Rotating Machines Using Deep Learning. IEEE Trans. Magn., vol. 55, 2019, Art no. 7202605.

[17].N. Ryu, W. S. Song, Y. Jung and S. Min. Multi-Objective Topology Optimization of a Magnetic Actuator Using an Adaptive Weight and Tunneling Method. IEEE Trans. Magn., vol. 55, 2019, Art no. 7202504.

[18].Y. Li, L. Liu, S. Yang, Z. Ren and Y. Ma. A Multi-Objective Topology Optimization Methodology and its Application to Electromagnetic Actuator Designs. IEEE Trans. Magn., vol. 56, 2020, Art no. 7506004.

[19].Technical report of the institute of electrical engineering of Japan, industry application society, No.776, 2000.

[20].S. Sato, T. Sato and H. Igarashi. Topology Optimization of Synchronous Reluctance Motor Using Normalized Gaussian Network. IEEE Trans. Magn., vol. 54, 2015, Art no. 8200904.

[21].H. Sasaki and H. Igarashi. Topology Optimization Using Basis Functions for Improvement of Rotating Machine Performances. IEEE Trans. Magn. vol. 54, 2018, Art no. 8201504.

[22].K. Watanabe, T. Suga and S. Kitabatake. Topology Optimization Based on the ON/OFF Method for Synchronous Motor. IEEE Trans. Magn., vol. 54, 2018, pp. 1-4.

[23].K. Watanabe, F. Campelo and H. Igarashi, Topology Optimization Based on Immune Algorithm and Multigrid Method, IEEE Trans. Magn. vol. 43, 2007, pp. 1637-1640.

[24].K. Watanabe et al.. Optimization of Inductors Using Evolutionary Algorithms and Its Experimental Validation. IEEE Trans. Magn. vol. 46, 2010, pp. 3393-3396.

[25].T. Sato, K. Watanabe, H. Igarashi. A modified immune algorithm with spatial filtering for multiobjective topology optimisation of electromagnetic devices. Compel-Int. J. Comp. Math. Electr. Electron. Eng. vol. 33, 2014, pp. 821-833.

[26].T.A. Lipo. Winding distribution in an ideal machine. Analysis of Synchronous Machine, 2nd ed. Boca Raton, FL, USA: CRC Press, 2012, pp. 1-76.

[27].M. Cheng, P. Han and W. Hua. General Airgap Field Modulation Theory for Electrical Machines. IEEE Trans. Ind. Electron., vol. 64, 2017, no. 8, pp. 6063-6074.

[28].M. Cheng, H. Wen, P. Han and X. Zhu. Analysis of Airgap Field Modulation Principle of Simple Salient Poles. IEEE Trans. Ind. Electron., vol. 66, 2019, no. 4, pp. 2628-2638.

[29].H. Wen, M. Cheng, Y. Jiang, M. Tong and W. Wang. Analysis of Airgap Field Modulation Principle of Flux Guides. IEEE Trans. Ind. Appl., vol. 56, 2020, no. 5, pp. 4758-4768

[30].M. Cheng, P. Han, Y. Du, H. Wen and X. Li. A Tutorial on General Air-gap Field Modulation Theory for Electric Machines. IEEE Trans. Emerg. Sel. Topics Power Electron, early access, doi: 10.1109/JESTPE.2021.3055224.

[31]. Zhang Xiaoyu, et al. "Research on adaptive segmented control strategy used in direct-drive wave power generation systems." Energy Reports 8 (2022): 8140-8150.

[32]. Leijon Mats, et al. "Multiphysics simulation of wave energy to electric energy conversion by permanent magnet linear generator." IEEE Transactions on energy conversion 20.1 (2005): 219-224.

[33]. Cheema Muhammad Ali Masood, et al. "Optimal, combined speed, and direct thrust control of linear permanent magnet synchronous motors." IEEE Transactions on Energy conversion 31.3 (2016): 947-958.

[34]. Chen Mei-Yung, and Jian-Shiun Lu. "High-precision motion control for a linear permanent magnet iron core synchronous motor drive in position platform." IEEE Transactions on Industrial Informatics 10.1 (2013): 99-108.

[35]. Lu Qinfen, et al. "Analytical model of permanent magnet linear synchronous machines considering end effect and slotting effect." IEEE Transactions on Energy Conversion 35.1 (2019): 139-148.

[36]. Wang Mingyi, Liyi Li, and Donghua Pan. "Detent force compensation for PMLSM systems based on structural design and control method combination." IEEE Transactions on Industrial Electronics 62.11 (2015): 6845-6854.

[37]. Cupertino Francesco, et al. "End effects in linear tubular motors and compensated position sensorless control based on pulsating voltage injection." IEEE Transactions on Industrial Electronics 58.2 (2010): 494-502.

[38]. Liu Chunyuan, et al. "Detent force reduction in permanent magnet tubular linear generator for direct-driver wave energy conversion." IEEE transactions on magnetics 49.5 (2013): 1913-1916.

[39]. Inoue Masaya, and Kenji Sato. "An approach to a suitable stator length for minimizing

the detent force of permanent magnet linear synchronous motors." IEEE Transactions on Magnetics 36.4 (2000): 1890-1893.

[40]. Zhu Yu-wu, et al. "Investigation of auxiliary poles design criteria on reduction of end effect of detent force for PMLSM." IEEE Transactions on Magnetics 45.6 (2009): 2863-2866.

[41]. Seo Sung-Won, et al. "Characteristic analysis of the influence of auxiliary teeth and notching on the reduction of the detent force of a permanent magnet linear synchronous machine." IEEE Transactions on Applied Superconductivity 28.3 (2018): 1-5.

[42]. Zhao Jing, et al. "Study on a double-sided permanent-magnet linear synchronous motor with reversed slots." IEEE/ASME Transactions on Mechatronics 26.1 (2020): 3-12.

[43]. Li Bin et al. "Detent force reduction of an arc-linear permanent-magnet synchronous motor by using compensation windings." IEEE Transactions on Industrial Electronics 64.4 (2016): 3001-3011.

[44]. Chung Shi-Uk, and Jong-Moo Kim. "Double-sided iron-core PMLSM mover teeth arrangement design for reduction of detent force and speed ripple." IEEE Transactions on Industrial Electronics 63.5 (2015): 3000-3008.

[45]. Huang Xuzhen, et al. "Detent force, thrust, and normal force of the short-primary double-sided permanent magnet linear synchronous motor with slot-shift structure." IEEE Transactions on Energy Conversion 34.3 (2019): 1411-1421.

[46]. Xu Xiaozhuo, et al. "Pole optimization and thrust ripple suppression of new Halbach consequent-pole PMLSM for ropeless elevator propulsion." IEEE Access 8 (2020): 62042-62052.

[47]. Lucchini Francesco, et al. "Topology Optimization for Electromagnetics: A Survey." IEEE Access 10 (2022): 98593-98611.

[48]. Sun Zhen and Watanabe Kota. "An Improved ON/OFF Method with a Two-step Surface Smoother for Topology Optimization of Electromagnetic Devices". *The 20th IGTE Symposium on Computational Methods in Electromagnetics and Multiphysics*. September, 2022.

[49]. Guirguis, David, et al. "Evolutionary black-box topology optimization: challenges and promises." IEEE Transactions on Evolutionary Computation 24.4 (2019): 613-633.

[50].J. Li, X. Song and Y. Cho, "Comparison of 12/8 and 6/4 Switched Reluctance Motor: Noise and Vibration Aspects," IEEE Trans. Magn., vol. 44, no. 11, pp. 4131-4134, Nov. 2008.

[51].A. Dorneles Callegaro, et al. "Radial Force Density Analysis of Switched Reluctance Machines: The Source of Acoustic Noise," IEEE Trans. Transp. Electrification, vol. 5, no. 1, pp. 93-106, March 2019.

[52].J. Furqani, et al. "Experimental Verification of Acoustic Noise and Radial Force Sum Variation in Switched Reluctance Motor," IEEE Trans. Ind. Appl., vol. 57, no. 3, pp. 2481-2493, May-June 2021.

[53].M. van der Giet, et al. "Comparison of 2-D and 3-D Coupled Electromagnetic and Structure-Dynamic Simulation of Electrical Machines," IEEE Trans. Magn., vol. 44, no. 6, pp. 1594-1597, June 2008.

[54].M. Abdalmagid, E. Sayed, M. H. Bakr and A. Emadi, "Geometry and Topology Optimization of Switched Reluctance Machines: A Review," IEEE Access, vol. 10, pp. 5141-5170, 2022.

[55].A. D. Callegaro, B. Bilgin and A. Emadi, "Radial Force Shaping for Acoustic Noise Reduction in Switched Reluctance Machines," IEEE Trans. Power Electron., vol. 34, no. 10, pp. 9866-9878, Oct. 2019.

[56].J. Bayless, et al. "Acoustic Noise Reduction of Switched Reluctance Motor With Reduced RMS Current and Enhanced Efficiency," IEEE Trans. Energy Convers., vol. 31, no. 2, pp. 627-636, June 2016.

[57].J. Liang, et al., "Analytical Calculation of Temporal and Circumferential Orders of Radial Force Density Harmonics in External-Rotor and Internal-Rotor Switched Reluctance Machines," IEEE Open Journal of Industry Applications, vol. 2, pp. 70-81, 2021.

[58].R. Pile, G. Parent, et al. "Effect of Mesh-to-Mesh Projection on the Magnetic Tooth Forces Calculation in Electrical Machines," Proc. Int. Conf. Elect. Mach. (ICEM), Gothenburg, Sweden, 2020, pp. 2500-2506

[59].T. Sato, K. Watanabe and H. Igarashi, "Multimaterial Topology Optimization of Electric Machines Based on Normalized Gaussian Network," IEEE Trans. Magn., vol. 51, no. 3, pp. 1-4, March 2015, Art no. 7202604.

[60].Y. Li, X. Liu, and Z. Liu, "Analysis and design of an interior permanent magnet synchronous machine with double-layer PMs for electric vehicles based on multi-physics fields", COMPEL, vol. 37, no. 1, pp. 118-135, 2018.

[61].Di Barba, Paolo, et al. "Optimal shape design of a class of permanent magnet motors in a multiple-objectives context." COMPEL, vol. 41, no. 6, pp. 1994-2009, 2022.

[62].S. Lim and S. Min, "Design optimization of permanent magnet actuator using multi-phase level-set model," IEEE Trans. Magn., vol. 48, no. 4, pp. 1641–1644, Apr. 2012.

[63].H. Shigematsu, S. Wakao, H. Makino, K. Takeuchi, and M. Matsushita, "Shape optimization of synchronous reluctance motor using sensitivity information for multiple objective functions", COMPEL, vol. 41, no. 6, pp. 2060-2071, 2022.

[64].P. Seebacher, M. Kaltenbacher, F. Wein, and H. Lehmann "A pseudo density topology optimization approach in nonlinear electromagnetism applied to a 3D actuator", Int. J.

Appl. Electromagn. Mech., vol. 65, no. 3, pp. 545-559, 2021.

[65].N. Takahashi, "Application of ON/OFF method to new conceptual design of magnetic devices", COMPEL, vol. 32, no. 6, pp. 1943-1954, 2013.

[66].Z. Sun, K. Watanabe, and X. Xu, "Design Optimization of Consequent-pole PMSM by ON/OFF Method and Multi-objective Evolutionary Algorithms," Int. J. Appl. Electromagn. Mech., vol.69, pp.305-317, 2022.

[67].F. Guo and I. P. Brown, Magneto-Structural Combined Dimensional and Topology Optimization of Interior Permanent Magnet Synchronous Machine Rotors, 2020 IEEE Energy Conversion Congress and Exposition, 2020.

[68].S. Hiruma, M. Ohtani, S. Soma, Y. Kubota and H. Igarashi, "Novel Hybridization of Parameter and Topology Optimizations: Application to Permanent Magnet Motor", IEEE Trans. Magn., vol. 57, no. 7, pp. 1–4, 2021.

[69].E.Kuci et al., Combination of topology optimization and Lie derivative-based shape optimization for electro-mechanical design, Struct Multidiscipl Optim, vol. 59, no. 5, pp. 1723–1731, 2019.

[70].F. Walter, "Model Translational Motion with the Deformed Mesh Interfaces," COMSOL, 2015, https://www.comsol.com/blogs/model-translational-motion-with-the-deformed-mesh-interfaces/.

[71].W. Zhao, F. Zhao, T. A. Lipo and B. -I. Kwon, "Optimal Design of a Novel V-Type Interior Permanent Magnet Motor with Assisted Barriers for the Improvement of Torque Characteristics," IEEE Trans. Magn., vol. 50, no. 11, pp. 1-4, Nov. 2014, Art no. 8104504, doi: 10.1109/TMAG.2014.2330339.

[72].R. Thike and P. Pillay, "Mathematical Model of an Interior PMSM With Aligned Magnet and Reluctance Torques," IEEE Transactions on Transportation Electrification, vol. 6, no.

2, pp. 647-658, June 2020, doi: 10.1109/TTE.2020.2991369.

[73].K. Yamazaki and M. Kumagai, "Torque analysis of interior permanent magnet synchronous motors by considering cross-magnetization: Variation in torque components with permanent-magnet configurations," IEEE Trans. Ind. Electron., vol. 61, no. 7, pp. 3192–3201, 2014, doi: 10.1109/TIE.2013.2278508.

[74].S. S. R. Bonthu, S. Choi and J. Baek, "Design Optimization With Multiphysics Analysis on External Rotor Permanent Magnet-Assisted Synchronous Reluctance Motors," IEEE Trans. Energy Convers., vol. 33, no. 1, pp. 290-298, March 2018.